3-26-2020

Modeling Nonlinear Heat Transfer for a Pin-on-Disc Sliding System

Brian A. Boardman

Modeling Nonlinear Heat Transfer for a Pin-on-Disc Sliding System

THESIS

Brian A. Boardman, Major, USAF

AFIT-ENC-MS-20-M-001

DEPARTMENT OF THE AIR FORCE
AIR UNIVERSITY

AIR FORCE INSTITUTE OF TECHNOLOGY

Wright-Patterson Air Force Base, Ohio

AFIT-ENC-MS-20-M-001

MODELING NONLINEAR HEAT TRANSFER FOR A PIN-ON-DISC SLIDING SYSTEM

THESIS

Presented to the Faculty

Department of Applied Mathematics and Statistics

Graduate School of Engineering and Management

Air Force Institute of Technology

Air University

Air Education and Training Command

in Partial Fulfillment of the Requirements for the

Degree of Master of Science in Applied Mathematics

Brian A. Boardman, B.S.

Major, USAF

March 2020

AFIT-ENC-MS-20-M-001

MODELING NONLINEAR HEAT TRANSFER FOR A PIN-ON-DISC SLIDING SYSTEM

THESIS

Brian A. Boardman, B.S.
Major, USAF

Committee Membership:

William Baker, Ph.D.
Chair

Anthony Palazotto, Ph.D., P.E.
Co-Chair

Richard Uber, Ph.D.
Member

Abstract

The objective of this research is to develop a numerical method to characterize heat transfer and wear rates for samples of Vascomax® 300, or Maraging 300, steel. A pin-on-disc experiment was conducted in which samples were exposed to a high-pressure, high-speed, sliding contact environment. This sliding contact generates frictional heating that influences the temperature distribution and wear characteristics of the test samples. A two-dimensional nonlinear heat transfer equation is discretized and solved via a second-order explicit finite difference scheme to predict the transient temperature distribution of the pin. This schematic is used to predict the removal of material from the specimens over time based on the temperature profile of the pin. The solutions presented also consider the experimental data and are used to determine characteristics of the contact interface and pin surface associated with the material removal process.

I will be forever indebted to my family for the love, patience, and support they have selflessly given me not only during my pursuit of this degree, but throughout my career. I would not be the person I am today without their continuous encouragement and grace.

Acknowledgements

I would like to thank my advisors, Dr. William Baker and Dr. Anthony Palazotto, for the guidance they provided in understanding the concepts from which this endeavor was framed upon. Their countless efforts over the past two decades concerning the intricacies of sliding contact provided expertise beyond measure. Their direction and patience throughout my research were instrumental in the completion of my degree.

I am also extremely grateful to Captain Richard Uber, who guided me in my return to mathematical academia and kept me on track during my initial investigations. His perspective and insight were invaluable throughout the course of my AFIT assignment.

This research project was sponsored by the Air Force Research Laboratory, Aerospace Systems Directorate. Their expertise proved to be essential during the design and implementation of the experimental testing that provided the foundation for this work.

Brian A. Boardman

Table of Contents

Page

Page

List of Figures

List of Tables

Nomenclature

α thermal diffusivity as a function of homologous temperature

α_1, χ_2 thermal diffusivity of stationary body

α_2, χ_1 thermal diffusivity of moving body

$\bar{E}_{removal}$ average stored thermal energy at material removal

$\bar{U}_E$ equivalent temperature corresponding to stored thermal energy at material removal

$\bar{U}_{removal}$ average surface temperature at material removal

β partition function

$\eta_{m,n}$ variable, nodal contribution of $n-1$ node in radial dimension

Γ constant, nonlinear contribution in axial length dimension

γ constant, solution node

$\hat{\alpha}$ thermal diffusivity as a function of temperature

$\hat{c}_p$ specific heat of material as a function of temperature

$\hat{k}$ thermal conductivity as a function of temperature

λ constant, centerline symmetry condition

μ coefficient of friction

Ω, ω angular velocity

$\omega_{m,n}$ variable, convective boundary condition along radial surface of pin

ϕ cylindrical azimuthal coordinate

$\Phi_{m,n}$ variable, heat flux boundary condition

Ψ constant, nonlinear contribution in radial dimension

$\psi_{m,n}$ variable, nodal contribution of $n+1$ node in radial dimension

ρ scaled radial length

ρ_s density

σ constant, nodal dependence in axial length dimension

θ homologous temperature

$\tilde{F}$ normalized force

$\tilde{Q}$ net heat transferred within a system

$\tilde{v}$ normalized velocity

$\tilde{W}$ normalized wear rate

ξ scaled axial length

A contact surface area

a pin radius

Bi Biot number

Bi_d Biot number of disc

Bi_p Biot number of pin

d_0 pin initial location

d_p pin location at time step p

E_{gen} energy generated in a control volume

E_{in} energy entering a system

E_{out} energy exiting a system

E_{st} stored energy within a system

E_{tot} total thermal and mechanical energy within a system

F normal force

$G_{m,n}$ variable, ratio of material properties as a function of homologous temperature

h convection heat transfer coefficient

H_0 room temperature hardness of material

h_c convection coefficient acting on pin contact (flat) surface

h_d convection coefficient acting on disc

h_r convection coefficient acting on pin radial surface

i a time step where material was removed

j total number of time steps where material was removed

k thermal conductivity as a function of homologous temperature

k_1 thermal conductivity of stationary body

k_2 thermal conductivity of moving body

k_f thermal conductivity of fluid

L distance between heat input and heat sink

M total number of nodes in radial dimension

m node location designator in radial dimension

N total number of nodes in axial length dimension

n node location designator in axial length dimension

Nu_m mean Nusselt number

P pressure

p time step

Pe Peclet number

Q heat flux as a function of homologous temperature

$q''(t)$ heat flux

q_g rate at which energy is generated

R radius of spinning disc

r cylindrical radial coordinate

r_c radius of heat flow

r_p radius of pin

Re_Ω Reynold's number

s contact/no contact switch

t time

t^* total time duration of test scenario

U temperature

U_∞ ambient temperature

U_m material melt temperature

u_m melt depth

U_s surface temperature

U_{crit} critical temperature

v velocity

v_f kinematic viscosity of air

W wear rate, volume lost per unit distance traveled

w net work done by a system

$X_{m,n}$ variable, convective boundary condition along flat surface of pin

y^* diffusivity depth

z cylindrical axial length coordinate

MODELING NONLINEAR HEAT TRANSFER FOR A PIN-ON-DISC SLIDING SYSTEM

I. Introduction

1.1 Background and Motivation

Initial research in the area of wear for Vascomax® 300 was motivated by hypersonic testing conducted at the Holloman High Speed Test Track (HHSTT), located at Holloman Air Force Base, New Mexico. During this testing, a rocket powered sled is propelled down the track at speeds approaching 3000 m/s, remaining attached to the rail through the use of wraparound slippers fabricated out of Vascomax® 300 material (see Figure 1). Safe operation of the testing vehicles presents a wide array of technological considerations, many of which are due to the extreme thermal environment encountered during a test run [35]. During testing operations, the wraparound slippers are exposed to extreme forces from sliding and bouncing contact with the test track. One major byproduct is heat generation due to friction, which causes damage and wear to the slipper material. Much research has been devoted to modeling the thermal and mechanical behavior of the slipper under these conditions considering a multitude of factors in order to estimate survivability and improve the durability of these slippers [4, 12, 15, 17, 25, 38]. Of primary concern regarding slipper wear are mechanical gouging, asperity collisions, and thermal effects. Gouging is caused by the slipper interacting with the rail as the sled travels down the track. A small gap between the slipper and the rail creates a bouncing phenomenon that aids in the cooling of the slipper material but also produces an additional impact energy. As the slipper impacts the rail, material may be removed from one or both surfaces. Asperity collisions arise

from the collision of surface imperfections on the rail impacting the slipper, which will cause deformation or removal of slipper material. These effects become more pronounced as temperatures increase and material properties change [3]. Evaluation of wear specific to the slipper requires knowledge of the thermal distribution of the material. As slipper failure would lead to catastrophic losses, the need to further refine methods predicting the thermal and mechanical behavior of the slipper material is an ongoing endeavor. This research continues the effort to predictively model slipper wear by focusing on the refinement of previously used thermal models and the use of actual experimental data collected under controlled conditions.

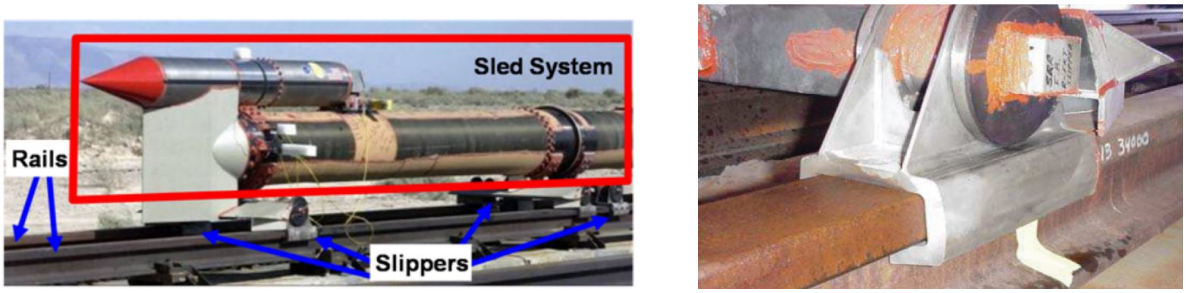

(a) Rocket Sled System (b) Slipper/Rail Interface

Figure 1. Holloman High Speed Test Track

1.2 Tribology

Tribology can be accurately described as "the science of rubbing" [9]. There are many aspects involved when considering this phenomenon, many of which have evolved and are complicated by technological advances. The interaction between two surfaces in motion against each other creates a highly complex system requiring significant evaluation to understand the effects of these interactions. This is the fundamental concept to the study of tribology. Of primary concern are the effects of friction and wear on the system. The effort of this work is an attempt at associating tribological concepts, based primarily on friction, to a high velocity environment.

1.2.1 Friction

Friction plays an important role in the study of most tribological systems. The force of friction exists due to resistance to initiate or sustain motion when two surfaces are in contact. The resistance to initiate motion can be described as the static or adhesion force, whereas the resistance to sustained motion can be referred to as the dynamic or deformation force [28]. The simple approach for evaluating friction is to use a function defined through the use of a Coulomb friction equation, which is the ratio of the frictional force and normal force. This ratio is referred to as the coefficient of friction (COF).

Oxide layers can be produced by the friction process due to the rise in temperature [9]. This "lubricative" presence can drastically affect the nominal COF. Temperature changes can also affect material properties, rates of oxidation, and induce phase transformations, all of which can result in large changes of frictional force [28]. While the interaction between the direct contact of solid surfaces dominates friction at lower sliding speeds, as the sliding speed increases a film of melted material may develop creating a lubrication layer, causing significant changes in the nominal COF.

1.2.2 Wear

Wear is the loss or removal of material when surfaces are in motion relative to one another. This process is complex in itself and can be greatly affected by temperature [9]. Wear rate can be quantified by volume or depth lost per unit distance traveled, although there are many other acceptable methods of measurement. Wear is a function of force, velocity, temperature, and the thermal, mechanical, and chemical properties of the materials. In general, the amount of wear is directly proportional to the applied load and sliding distance, and inversely proportional to material hardness.

1.3 Research Focus

Accurate predictions of material removal are essential to ensure survivability of a system during a test run. Temperature increases generally accompany softening of the material or other phase changes that may affect the material behavior. As such, it is desirable to develop a detailed temperature distribution to corroborate the thermal effects on material wear. The frictional heat generated under the conditions of this investigation is a function of several parameters, most of which are estimated but several of which are known, unlike previous works. This research, while acknowledging that the mechanical aspects of wear on sliding contact phenomena are of importance, focuses primarily on temperature as the key predictor of material removal.

Previous studies regarding the influence of temperature on slipper wear at the HHSTT were formulated on the basis of melt wear. Specifically, a one-dimensional finite difference algorithm was developed to approximate the temperature distribution of the slipper and produce melt wear estimations exclusively related to a particular 2008 experiment at the HHSTT [4]. Input for the one-dimensional model was data from Dynamic Analysis and Design System (DADS), a computer generated program for the 2008 test run. Melt wear predicted by the model was compared to actual wear results measured from a slipper recovered following the test run. Similar in nature, this research uses a model generated temperature distribution as the primary input for wear calculations, and compares the results to the data collected from pin-on-disc experiments.

1.4 Problem Statement

The objective of this research is to develop a two-dimensional numerical model to characterize the transient thermal distribution of cylindrical test samples fabricated from Vascomax® 300, which is the material present in the slipper incorporated in the test track's 2008 test. Analysis will focus on the flow of heat through these specimens when subjected

to frictional heat generated by high-speed sliding contact in a pin-on-disc configuration. Experimental pin-on-disc testing is conducted to validate and tune the numerical model, with consideration of various force and velocity profiles. The thermal model is used to determine if there is a quantifiable "critical temperature" value below the material's melting point such that, when the contact surface reaches this temperature, material is removed from the test specimen in a manner similar to what is observed in experimental testing. As current thermal modeling of the testing scenarios at the HHSTT concern only material removal due to melt, the introduction of a critical temperature concept may be used to more accurately characterize wear processes. The implementation of this methodology compensates for the fact that the mechanics contributing to wear are not coupled in the analysis.

The desire for a two-dimensional model arises when considering the boundary conditions present along the leading and trailing surfaces of the slipper, as the previously developed one-dimensional model cannot capture lateral heating and cooling effects. Therefore, the formulation of a two-dimensional cylindrical model supporting the pin-on-disc experiments has a direct correlation to the slipper configuration by considering the additional surface exposure along the transverse surface. The pin-on-disc experiment is then a representation of the front portion of the slipper used at the HHSTT, albeit on a different scale.

1.5 Experimental Design

The experimental features of the test facility used will now be discussed. This testing was conducted as part of a preliminary investigation with the desire to simulate a scaled version of the force and velocity conditions the slippers experience at the HHSTT. The test rig (Figure 2), designed by engineers at the Air Force Research Laboratory (AFRL), consists of a drive stand capable of 30,000 RPM upon which is mounted a 12-inch diameter disc of AISI 4340 steel. Cool air is blown onto the bottom of the disc to normalize the

disc's surface temperature as close to ambient as possible before the next contact. A motor-actuated holder, manually controlled by the machine operator, brings the test article into contact with the disc which spins clockwise (from observer's perspective) at prescribed rotational speeds to simulate the slipper sliding along a steel rail.

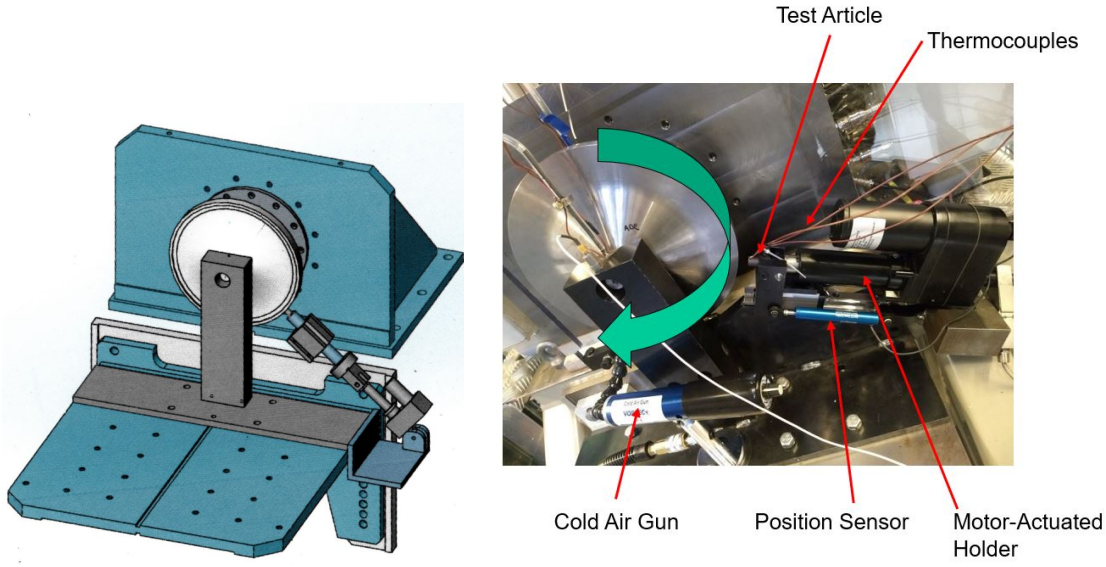

(a) Rig Design (b) Test Rig

Figure 2. Experimental Design

For the purposes of these experiments, each test run is conducted at a constant velocity. Test articles (Figure 3) are constructed from Vascomax® 300 material and cut into cylinders with ½-inch diameter and 1-inch length. Sensors include three Type-J thermocouples embedded through small holes drilled ⅕-inches deep from the radial surface, spaced at approximately ⅛-inch intervals from the face of the article and offset from each other by approximately 30 degrees. Type-J thermocouples have a maximum temperature rating of 1030 K $\pm$ 0.75%; temperature readings above this rating will be considered unreliable for exact analytical purposes. A LDI-119 Series Linear Variable Inductive Transducer was used for position sensing. Once placed in the holder, ½-inch of the test article remains exposed.

A DEWESoft data acquisition unit was used to collect thermal data, contact force, and

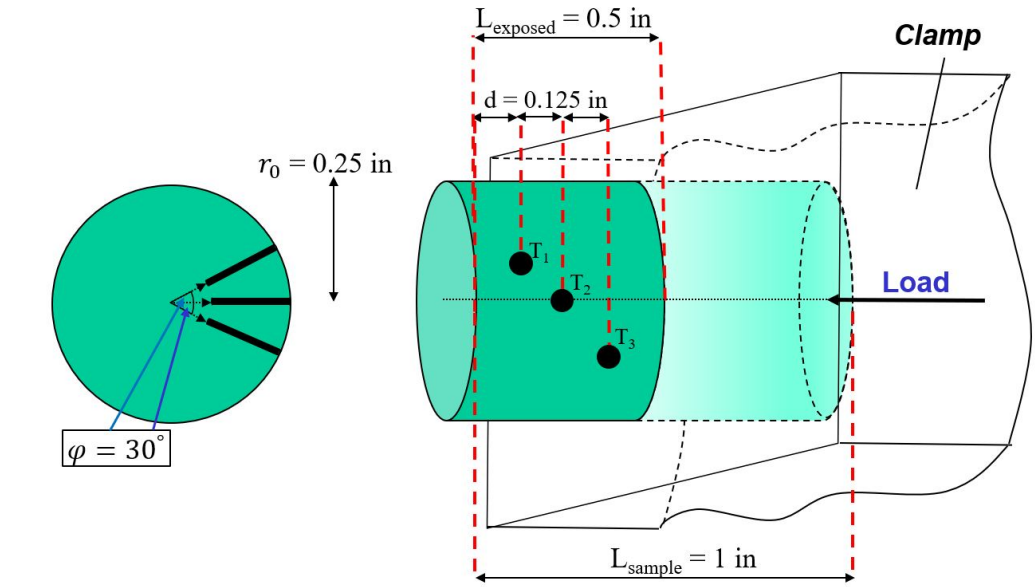

Figure 3. Pin Diagram

displacement of the linear actuator. Displacement will be defined by distance (mm) traveled by the specimen after initial contact with the spinning disc, with $d_0 = 0$ representing the specimen's displacement at initial contact and d_p representing the specimen's location at time step p, with a positive value indicating material removal due to wear. Collection rates were 2000 samples per second for RPM, force, and displacement data, and 100 samples per second for temperature data. Planned contact force was limited to 500 foot-pounds (2224 Newtons).

1.5.1 Experiment Parameters

Pin-on-disc tests were conducted under dry sliding conditions at disc speeds up to 16,000 RPM (which led to contact velocities up to 240 m/s) due to limitations on the shaft coupling the wheel to the drive stand. Data was collected for tangential velocities of 15, 48, 96, 128, and 240 m/s under varying normal loads applied as shown in Figure 3. The first three velocities were under a constant contact condition where force was applied to keep the face of the test article in contact with the wheel for the duration of the test run.

The last two runs incorporated a pulsing effect where contact was initiated and then disengaged multiple times. Although the numerical model is constructed to consider the pulsing contact scenario, this research will focus mainly on the experimental tests conducted under constant contact at velocities of 48 and 96 m/s. Experimental parameters for these tests are outlined in Table 1.

Table 1. Experimental Summary

RPM	Velocity	Duration	Force (N)		
			Minimum	Maximum	Average
3000	48 m/s	8.4 s	40	1304	641
6000	96 m/s	5.7 s	49	1281	556

Figures 4 and 5 show temperature recorded by the thermocouples and force data collected from the experimental test runs conducted at 48 and 96 m/s, respectively. The lack of smoothness in Figure 4a for the temperature profile of Thermocouple 1 is indicative of the dynamic conditions and design limitations present in the experimental testing, and may be attributed to momentary shifting of the thermocouple. Temperatures recorded by Thermocouple 1 for both velocities exceed the maximum rated value for the thermocouple and while they continue to record reasonable temperatures above this value, this data will be used purely to estimate behavior within the thermal model and not from an analytical standpoint. The periodic nature of the recorded force data in Figures 4b and 5b is due to the operator-controlled displacement actuator used to drive the specimen towards the disc and subsequently maintain contact between the pin and the disc, as desired. The difficulty in force application and control creates an inability to pre-program force inputs or to replicate experimental conditions. Thus, each test is unique in terms of force input.

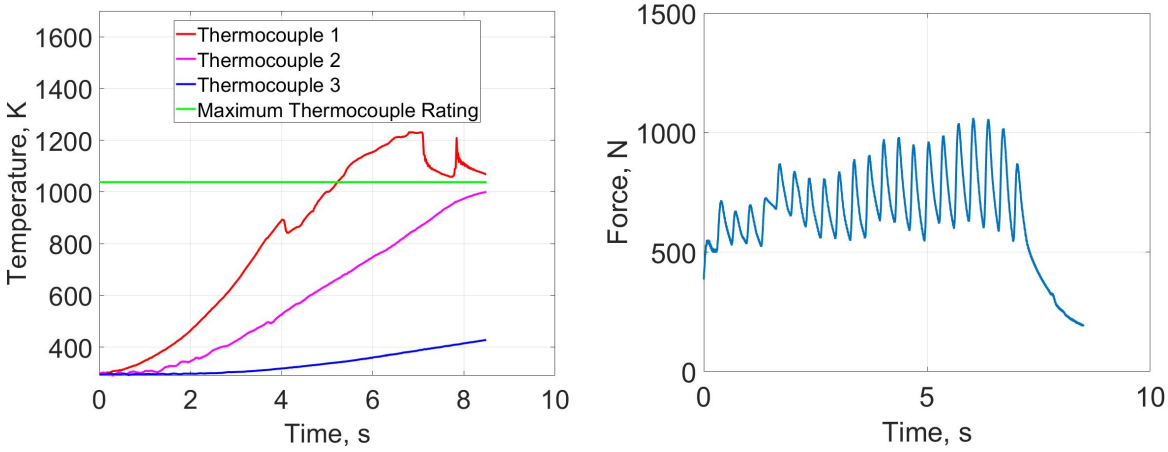

(a) Thermocouple Temperature Data (b) Force Profile

Figure 4. Experimental Data, Constant Contact, 48 m/s

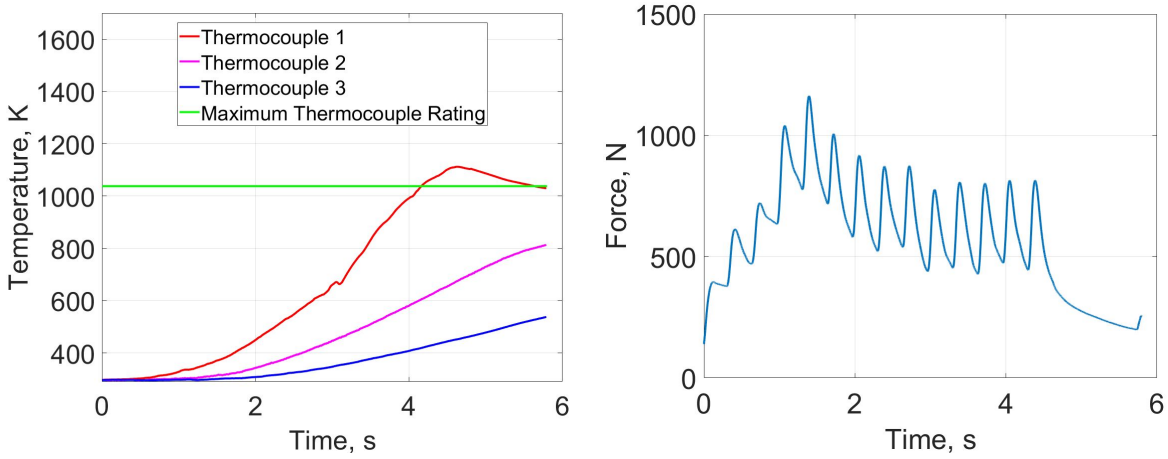

(a) Thermocouple Temperature Data (b) Force Profile

Figure 5. Experimental Data, Constant Contact, 96 m/s

1.6 Background Theory

1.6.1 Modes of Heat Transfer

Transfer of heat between substances will occur when a temperature differential exists. This can occur through the processes of conduction, convection, and radiation. The modes, and the importance placed on each of them, are determined by the system and nature of the materials involved. This research is primarily focused on the heat transfer methods of conduction and convection.

1.6.1.1 Conduction

Conduction is the transfer of energy that takes place within a medium. This diffusion process is dependent on the material and the temperature differential that exists and is governed by Fourier's Law, which is given by

$$\vec{q}''(t) = -\hat{k}(U)\vec{\nabla}U. \tag{1}$$

Here, $\vec{q}''$ (W/m^2) represents the heat flux vector, or the rate of heat transfer per unit area. The parameter $\hat{k}(U)$ is the thermal conductivity (W/m·K) of the solid, which is a transport property of the material indicating the rate at which energy is transferred by the diffusion process and may be a constant value or dependent on temperature [7]. We define U to represent the temperature value in Kelvin (K). The temperature gradient vector $\vec{\nabla}U$ can be expressed in three-dimensional form as

$$\vec{\nabla}U = \frac{\partial U}{\partial x}\vec{i} + \frac{\partial U}{\partial y}\vec{j} + \frac{\partial U}{\partial z}\vec{k} \tag{2}$$

where $\vec{i}, \vec{j}$, and $\vec{k}$ are the unit vectors in the positive x, y, and z directions, respectively. Fourier's Law states that the heat flow is proportional to the temperature gradient that exists and occurs in the direction of decreasing temperature, as indicated by the minus sign.

1.6.1.2 Convection

Convection is the process in which heat is transferred between a fluid in motion and another surface when a temperature difference exists. This transfer is dependent on the nature of the flow and can be forced, when the flow is caused by external means, or natural, caused by temperature variations in the fluid which drive the movement [7]. The heat flow due to convection (W/m^2) is determined by Newton's Law of Cooling expressed as

$$q''(t) = h(U_s - U_\infty), \tag{3}$$

which states the convective heat flux is proportional to the difference between the surface and ambient temperatures, U_s and U_∞ respectively, multiplied by the convection heat transfer coefficient h (W/m$^2\cdot$ K), which depends on the conditions in the boundary layer. These conditions strongly influence the temperature gradient along the surface/fluid interface and dictate the rate of heat transfer along this interface. Complications in determining the value or values of the convection coefficient arise from the dynamics of the fluid properties, surface geometry, and flow conditions [7]. The role of convection in many heat transfer scenarios, including the one present in this experiment, is that of determination of the boundary conditions that will dictate the solution of the partial differential equation (PDE) of interest.

1.6.2 Conservation of Energy

The first law of thermodynamics, the law of conservation of energy, provides a foundation for the derivation of the heat equation. This principle states that changes in energy within a control volume with respect to time are a result of the amount of energy entering and exiting the control volume minus the net work done by the system. This is expressed as

$$\triangle E_{tot} = \tilde{Q} - w \tag{4}$$

where $\triangle E_{tot}$ is the change in the total thermal and mechanical energy within the system, $\tilde{Q}$ is the net heat transferred within the system, and w is the net work done by the system [7]. As we are focused primarily on temperature and mechanical effects will be decoupled in the analysis, energy will be evaluated on the basis of transfer of thermal energy alone and

utilization of the stored thermal energy within a system. The purpose of this is to develop a technique to associate strictly thermodynamic principles, and the flow of heat within a system, with wear processes. A simple one-dimensional case is shown in Figure 6 with E_{st} as the energy stored within the system, E_{in} as the energy entering the system, E_{out} as the energy exiting the system, and E_{gen} as the energy generated in the control volume.

This can also be expressed over a time interval, as energy must be balanced between all energy rates. Thus,

$$\dot{E}_{st} = \dot{E}_{in} - \dot{E}_{out} + \dot{E}_{gen} \tag{5}$$

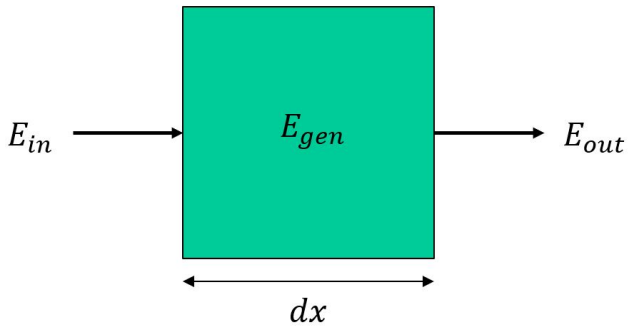

Figure 6. Conservation of Energy

If mechanical and chemical energy are not pertinent, then the rate of change of the stored thermal energy of the system may be expressed as

$$\dot{E}_{st} = \rho_s \hat{c}_p \frac{\partial U}{\partial t} dx \tag{6}$$

where U is the temperature (K), t is time (s), ρ_s is the material mass density (kg/m^3), $\hat{c}_p$ is the specific heat of the material (J/kg·K), and $\rho_s \hat{c}_p \partial U / \partial t$ is the change in thermal energy of the system over time, per unit volume [7].

1.6.3 Heat Diffusion Equation

Using the principles of energy conservation and considering only thermal energy, in conjunction with Fourier's Law, yields the heat diffusion equation expressed as the partial differential equation

$$\underbrace{\rho_s \hat{c}_p(U)\frac{\partial U}{\partial t}}_{\dot{E}_{st}} = \underbrace{\nabla \cdot (\hat{k}\nabla U)}_{\dot{E}_{in}-\dot{E}_{out}} + \underbrace{q_g}_{\dot{E}_{gen}}, \tag{7}$$

where $\hat{c}_p$ is the specific heat as a function of temperature and q_g is the rate at which energy is generated. In a scenario with no heat generation due to plastic material action and constant material properties, the equation becomes

$$\frac{1}{\hat{\alpha}}\frac{\partial U}{\partial t} = \nabla^2 U, \tag{8}$$

where $\hat{\alpha}$ is the thermal diffusivity of the material (m^2/s) given by the ratio

$$\hat{\alpha} = \frac{\hat{k}}{\rho_s \hat{c}_p}. \tag{9}$$

The thermal diffusivity of a material is a measurement of the rate of heat transfer through the material. It is related to the penetration of heat into the material and the speed at which this occurs, and affects the system's ability to reach thermal equilibrium [16]. Demonstrated in Equation 8, higher values of thermal diffusivity will increase the internal temperature within the material at a given time when compared to materials with lower values of thermal diffusivity.

1.6.4 Heat Flux

When surfaces are in sliding contact with one another the work required to overcome friction will generate energy, most of which is dissipated in the form of heat. This heat

is conducted into the two bodies through points of contact, which can be approximated as a single contact or as multiple contacts [9]. Under high force conditions, this results in essentially a single contact between the bodies during the sliding process. The conduction of heat results in temperature increases throughout the materials. The frictional energy generated is directly proportional to the friction coefficient, pressure, and velocity [39] and is given by the expression

$$q''(t) = \frac{\mu(t)F(t)v(t)}{A(t)} \tag{10}$$

where μ is the coefficient of friction, F is the normal force applied to the sample, v is the velocity of the wheel, and A is the contact area. A portion of this heat will travel into the test sample and a portion will flow into the spinning disc. Conductive heat flux into the sample is expressed as

$$q''(t) = \frac{\beta(t)\mu(t)F(t)v(t)}{A(t)}, \tag{11}$$

where β is partition coefficient describing the fraction of heat flowing into the sample. As these parameters can be time dependent, the heat flux is a function of time and heavily dependent on the values of β and μ.

II. Literature Review

2.1 Chapter Overview

Due to the dynamic conditions associated with this pin-on-disc scenario and its relation to the HHSTT, it is necessary to further investigate the contributing factors to wear and heat transfer. As this research is motivated to consider slipper wear at the HHSTT and subsequent work performed at the Air Force Institute of Technology (AFIT), both previous research performed at AFIT and that of other individuals concerning pin-on-disc configurations is investigated. This problem requires understanding of wear processes in general, and the effects of friction, material properties, and heat diffusion on the temperature distribution of the pin that are specific to this system. This chapter aims to enhance understanding of the primary contributing factors when relating heat transfer and material wear. The application of these concepts in regards to the pin-on-disc configuration examined in this work will follow in Chapter 5.

2.2 Sliding Wear

Wear can take on many forms, generally described as adhesive, corrosive, and abrasive, which may all be present simultaneously. In sliding contact, adhesive and abrasive wear are most prominent. Adhesive wear occurs when particles are sheared off one material and deposited to the surface of the other surface. Abrasive wear is caused by hard particles from one surface displacing material from another surface. A common example of abrasive wear is gouging [28]. Wear is often classified into rates of mild or severe. Mild wear is characterized by lower wear rates, smooth surface conditions with oxides present, and fine oxide particle debris. Severe wear consists of high rates of wear (100-1000 times higher than mild wear), rough surface conditions with heavily deformed metallic material and oxide particles present, and course metallic flake debris [28].

Sliding wear between two surfaces can occur under dry sliding or lubricated conditions. Consideration must be given to the stresses and damage that can occur at the asperity and macroscopic levels, the thermal effects of the frictional heat generated by the sliding action, and the chemical reactions and surface interactions that result. For sliding contact of metals, these chemical reactions include the formation of oxide layers as the temperature of the metal increases and reacts with the surrounding air. Depending on the speed and force conditions present, this oxide layer can heavily influence wear rates by preventing further oxidation of the metal below and preventing metal-metal contact at the surface. There often exists a transition temperature in which the oxide layer will form continuously, reducing sliding resistance and further protecting against wear damage [48]. Thus, any factor that influences the rate of oxidation will drastically affect the respective wear regimes. A way to represent these wear regimes is through the use of wear maps, which visually depict the dominating wear mechanism associated with conditions within a system. As the most commonly accepted wear maps depend on sliding speed and loading conditions, which directly influence temperature, the thermal effects on wear are of principle importance.

The damage produced by sliding contact can be observed through microstructural changes due to mechanical deformation and temperature effects, the formation of oxide layers at the wearing surface, and wear debris being expelled from the contact interface. This debris may consist of oxides which would be typical of lower speeds, or of the specimen material itself, which would be more likely at higher speeds. Oxidative wear occurs when the debris is removed from the oxide layer. Lim and Ashby [39] developed the terms mild and severe-oxidative wear, which characterize the amount of oxidation present as opposed to the wear rates associated with oxidation. In most cases, the wear rate in the severe-oxidational regime is lower than that of the mild-oxidational regime, but both regimes can give mild wear [48]. Oxide layers at the surface can be generated even at low sliding speeds for steels, around 1 m/s. At the asperity level, it has been assumed that this oxide

film forms on asperities and grows to some critical thickness, at which point it is removed as debris. This would be considered mild-oxidational wear [48]. Severe-oxidational wear occurs when the oxide layer forms continuously and frictional heat is sufficient to melt the oxide, causing the melted oxide to be lost as wear fragments.

Throughout the sliding wear process, different forms of wear may be present. It would be expected that early on, wear would be high due to metal-metal contact. As temperatures increase, oxide layers develop leading to more protective surfaces that may decrease wear rate. Depending on the system, this could eventually progress to melt wear [48]. Unfortunately, the transitions from one form of wear to another are often difficult to characterize and are heavily influenced by system properties in a addition to the materials in question.

2.3 Lim and Ashby

Research by Lim and Ashby [39] in the 1980s was devoted towards characterizing different regimes of wear for steels based on the input parameters most closely associated with the wear process. Their work analyzed a multitude of experimental tests, and consolidated those results to develop wear maps. The majority of the data considered were from dry sliding, pin-on-disc experimental tests. Since the data were collected over a wide range of velocities, forces, and geometrical orientations, normalized parameters of wear ($\tilde{W}$), velocity ($\tilde{v}$), and force ($\tilde{F}$) were introduced. These parameters are defined by

$$\tilde{W} = \frac{W}{A}, \tag{12}$$

$$\tilde{v} = \frac{v r_p}{\hat{\alpha}}, \tag{13}$$

and

$$\tilde{F} = \frac{F}{A H_0}, \tag{14}$$

where W is the volume lost per unit distance traveled, A is the contact area (m^2), v is the sliding velocity (m/s), r_p is the radius of the pin (m), F is the normal force on the sliding interface (N), and H_0 is the room-temperature hardness of the metal (N/m^2). The regimes of wear shown in Figure 7 show the dominant mechanism of wear under the normalized conditions described by Equations 13 and 14. Thus, the wear regime and normalized wear rate, given by Equation 12 and displayed as the contour lines on the wear map in Figure 7, are functions of normalized velocity and normalized pressure.

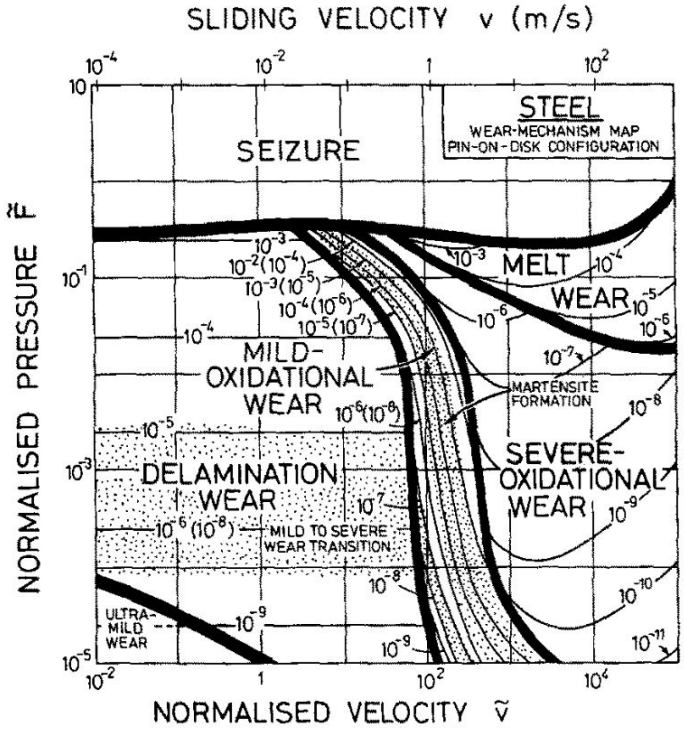

Figure 7. Lim and Ashby Wear Mechanism Map for Steel [39]

Delamination wear can be thought of as fatigue wear. It occurs from deformation at the surface causing cracks in the material, which eventually lead to the shearing of material in thin sheets [49]. Ultra-mild wear occurs at low force and velocity ranges. The oxide layer that is formed is not worn away and thus, there is no metal-metal contact. The regime of mild-oxidational wear occurs over a narrow range of normalized velocities by formation of an oxide layer in which wear is caused by the splitting off of this layer due to its thin, patchy,

and brittle characteristics [39]. The wear rate in this regime may also be influenced by a material phase change to a more martensitic structure characterized by increased material hardness, which equates to a sudden lowering of the wear rate experienced. Other than this factor, in the regimes of mild-oxidational, delamination, and ultra-mild wear, the thermal effects have little impact on wear [28].

Severe-oxidational wear occurs when the surface temperature is high but not yet to the melt temperatures of the material itself, and an oxide layer forms where the material removed consists of oxide from this layer rather than the metal. This layer is thicker and more continuous in comparison with the mild-oxidation regime, and the wear may be abrasive or due to melting of the oxide. In the melt wear regime, the force and velocity conditions are high, and the role of thermal conduction is ineffective at removing heat from the surface, and melting occurs. This melt may cause a layer of lubrication that will decrease the coefficient of friction values, but will be characterized by higher wear rates due to the ease in which the molten material is removed. Temperatures within this regime are high and it is likely that oxidation wear is also present. Experimental evidence gathered by Lim and Ashby [39] indicates that the role of oxidation wear is more dominant than that of local melting. The lines on these wear maps represent possible areas of transition from one form of wear to another, however they are not precise and only are used to express general behaviors. Figure 7 can be generalized into regions of mild and severe wear (discussed in Section 2.2) dependent on velocity and pressure profiles, as shown in Figure 8.

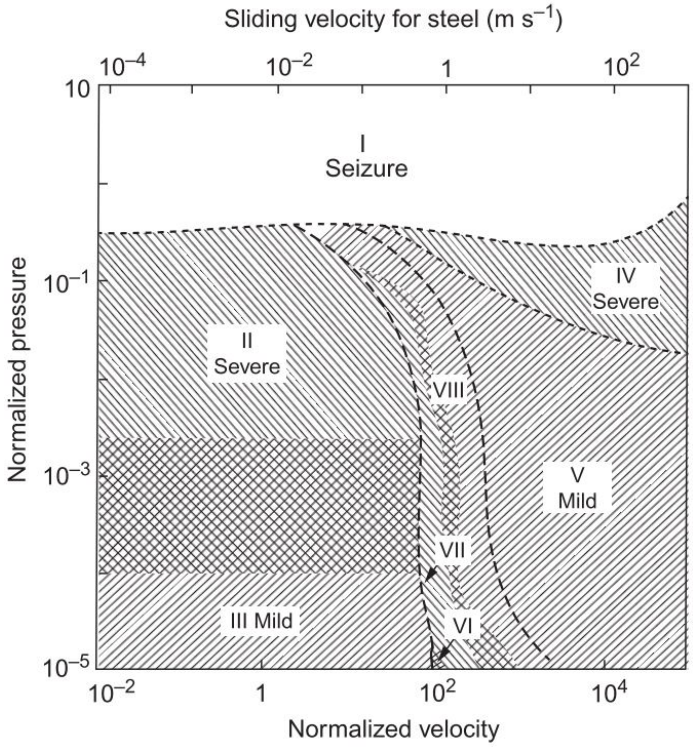

Figure 8. Wear Mode Map for Dry-Sliding of Typical Steels [28]

2.4 Coefficient of Friction

The values for coefficient of friction directly affect the solution to the temperature distribution of the system, as they are essentially a scaling parameter for the heat flux boundary condition (where q'' is given by Equation 11). The contribution of this work is designed for applications such as experiments at HHSTT and modeling pin-on-disc configurations, therefore research pertaining to both systems is relevant and considered.

2.4.1 Montgomery

Montgomery's primary interest was characterizing cannon muzzle wear supporting the U.S. Army in the 1940s and 1950s. This investigation was one of the earliest considerations of speeds within a higher velocity regime, since at that time cannon velocities were capable of reaching 1500 m/s. Data was collected using a high speed pin-on-disc test device testing

speeds up to 548 m/s. The experiments were performed using test samples constructed from copper, iron, and steel and brought into contact with a rotating steel disc. Friction coefficients were measured continuously through strain gauges. Thermocouples were also placed into the test specimens, however they yielded unsatisfactory results and were not considered in his analysis.

Analysis from the firing of artillery rounds and pin-on-disc experiments led Montgomery to conclude that the heat generated by friction was sufficient to induce a molten layer of metal, thus producing a "lubricated" sliding condition. This conclusion was validated by comparison with collected heat generation data. When samples were subject to a high rate of heat generation (a result of increased pressure and velocity), the coefficient of friction decreased and eventually stabilized, leading to the conclusion that there was a melted surface layer present that affected coefficient of friction values. Montgomery plotted coefficient of friction results as a function of pressure-velocity as shown in Figure 9.

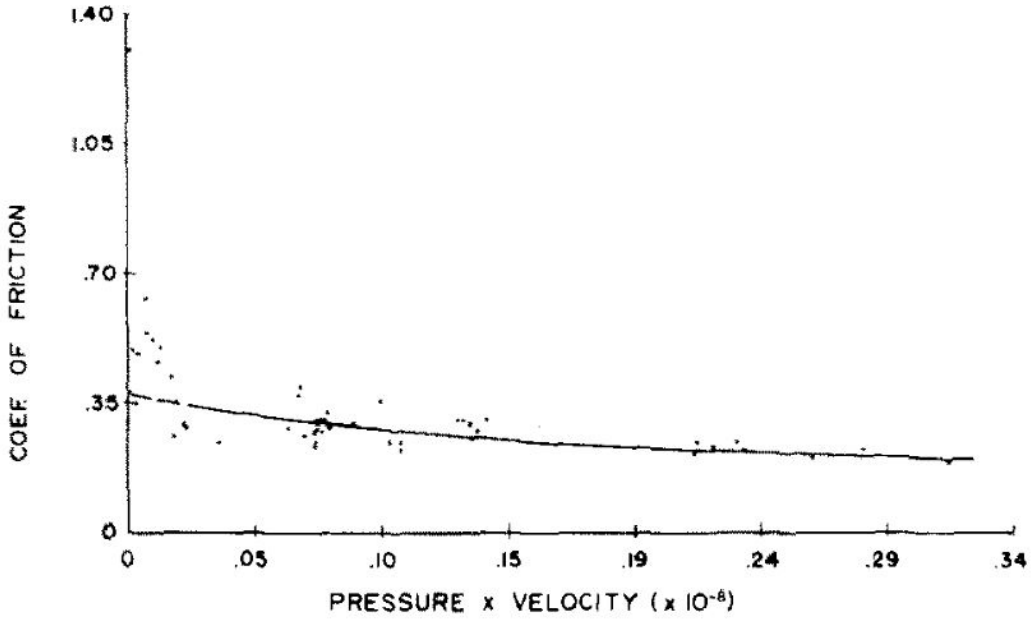

Figure 9. COF of projectile steel as a function of pressure x velocity, psi x ft/s [41]

Further utilization of heat generation data was also used in analysis of calculated wear rates for the test specimens, in terms of volume lost per foot distance traveled (Figure 10).

Montgomery attributed the scattering of data at lower pressure-velocities to the instability of coefficient of friction values that characterized this regime, as it was probably a result of only partial surface melting. He hypothesized that as the pressure-velocity increased however, this formed a region of uniform surface melting where the friction and wear rates stabilized. At this onset, he hypothesized the presence of a region of melted material in between the two surfaces, the presence of which suggested that they were likely not in actual contact but separated by this lubricating film.

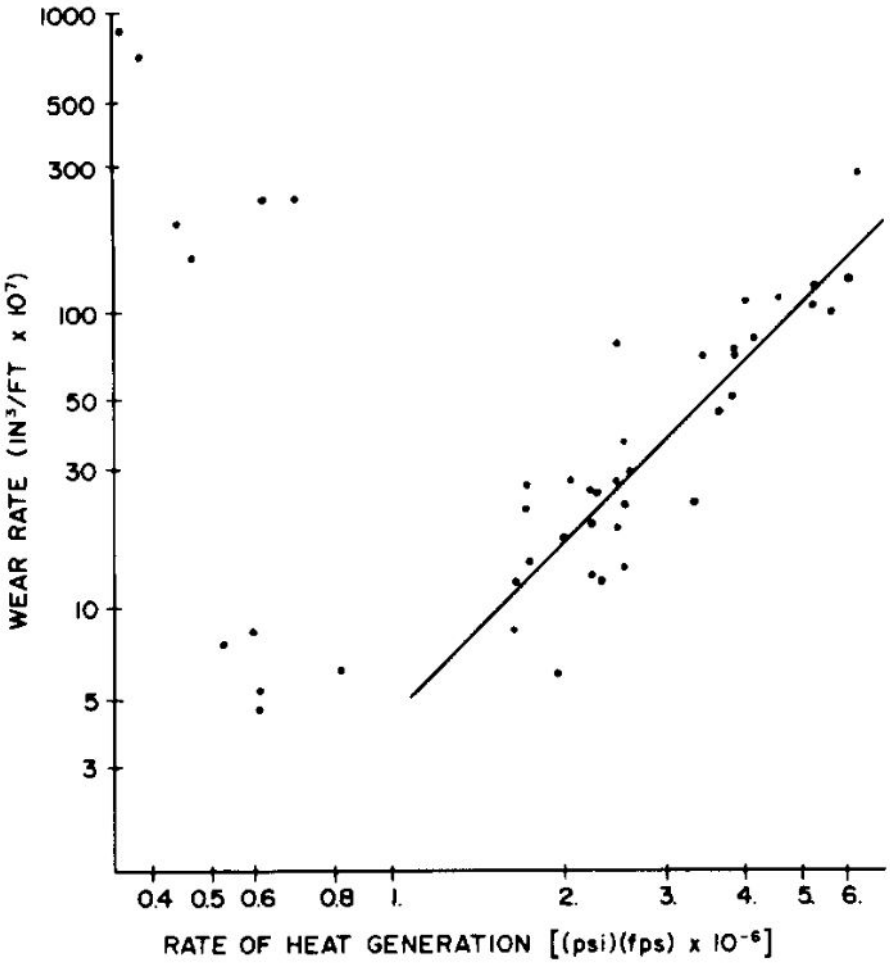

Figure 10. Wear Rate of projectile steel as a function heat generation [41]

Montgomery's calculations were substantiated by further research involving constant velocity, high speed pin-on-disc experiments involving various materials, and projectile

data calculations based on the actual firing of artillery rounds. He was able to attribute the formation of a lubrication film to a specific pressure velocity value where there were abrupt decreases in the values for coefficient of friction and wear rates [43]. As shown in Figure 11, due to several differences between the conditions simulated in the pin-on-disc tests and the projectile data, including changes in velocity and the heat generated from the firing of the projectiles, the location of these decreases in friction occurred at much lower values of pressure-velocity than those observed in the pin-on-disc experiments. This corresponded to lower values of steady-state coefficient of friction of 0.02 for the muzzle data, as opposed to 0.2 for the pin-on-disc experiments.

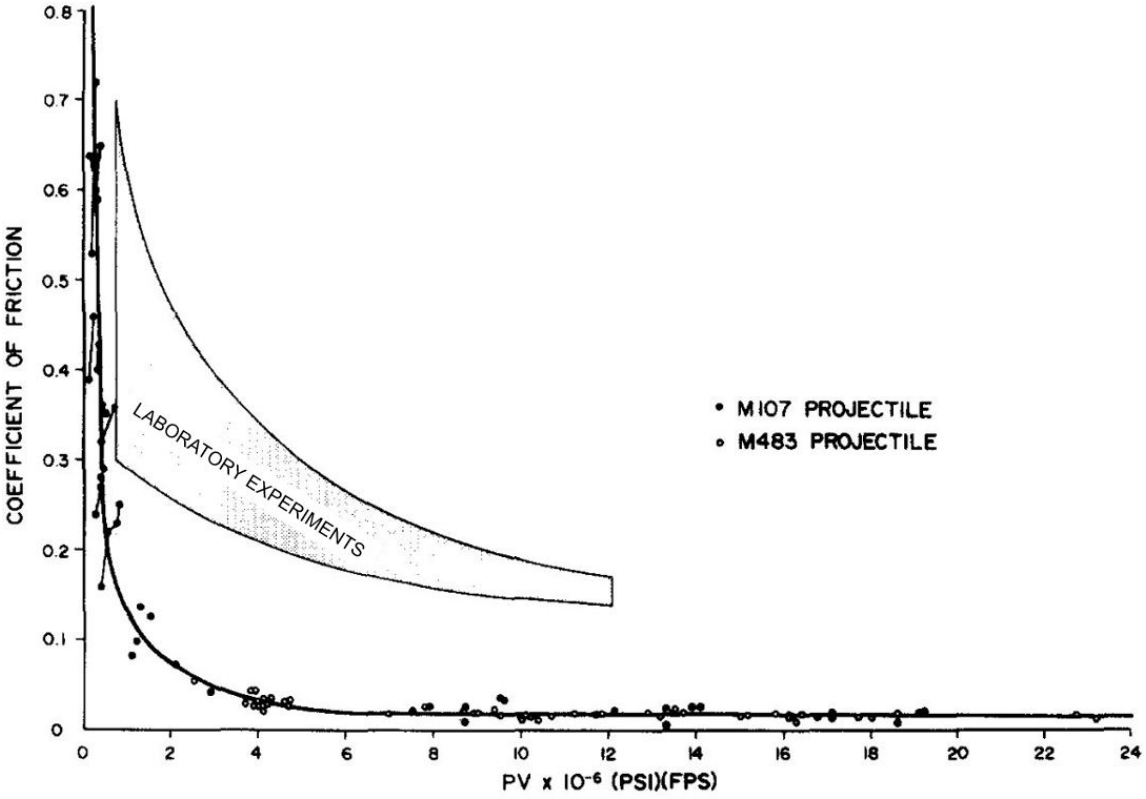

Figure 11. Wear Rate of projectile steel as a function heat generation [43]

2.4.2 Carignan and Rabinowicz

In an effort to achieve high velocity and loading conditions similar to Montgomery and confirm the hypothesized drop in friction coefficients at high sliding speeds, Carignan and Rabinowicz [13] performed pin-on-disc testing at speeds approaching 150 m/s with various metals sliding against a steel disc. The results they collected did not, in general, duplicate the low coefficient of friction coefficients reported by ballistic measurements, even when the surface temperatures approached the material melting points. They observed coefficients of friction that remained above 0.15 as shown in Figure 12, whereas the approximations for coefficient of friction values from Montgomery's ballistic work approached 0.02. Montgomery worked closely with Carignan and Rabinowicz and attributed the discrepancy in replicating these conditions in pin-on-disc testing to the inability of the leading edge of small diameter pins to reach melt lubrication except under high loading conditions [42]. Through their experimental results and analysis, Carignan and Rabinowicz concluded that the influence of melt lubrication may not be as drastic as previously hypothesized.

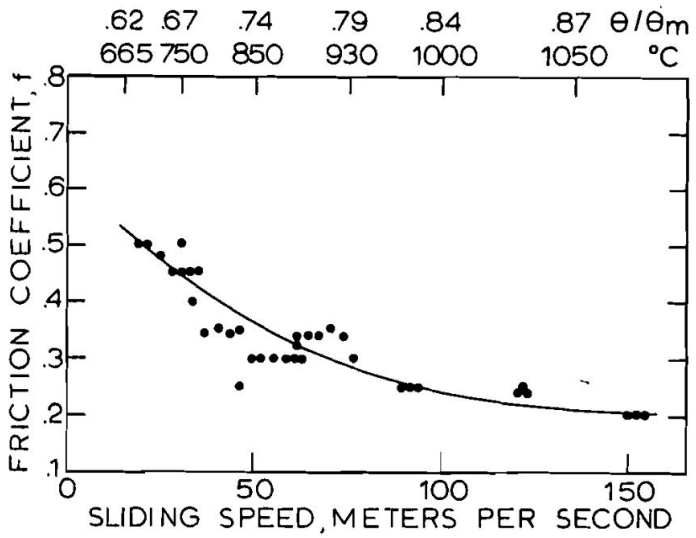

Figure 12. Coefficient of Friction for Constantan (60% Cu, 40% Ni) against 4140 Steel [13]

2.4.3 Lim and Ashby

In their development of wear maps Lim and Ashby also collected experimental data for coefficient of friction values for the dry rubbing of steel-on-steel over a wide range of velocity and force conditions. This data included the work done by Montgomery [41] and is shown in Figure 13.

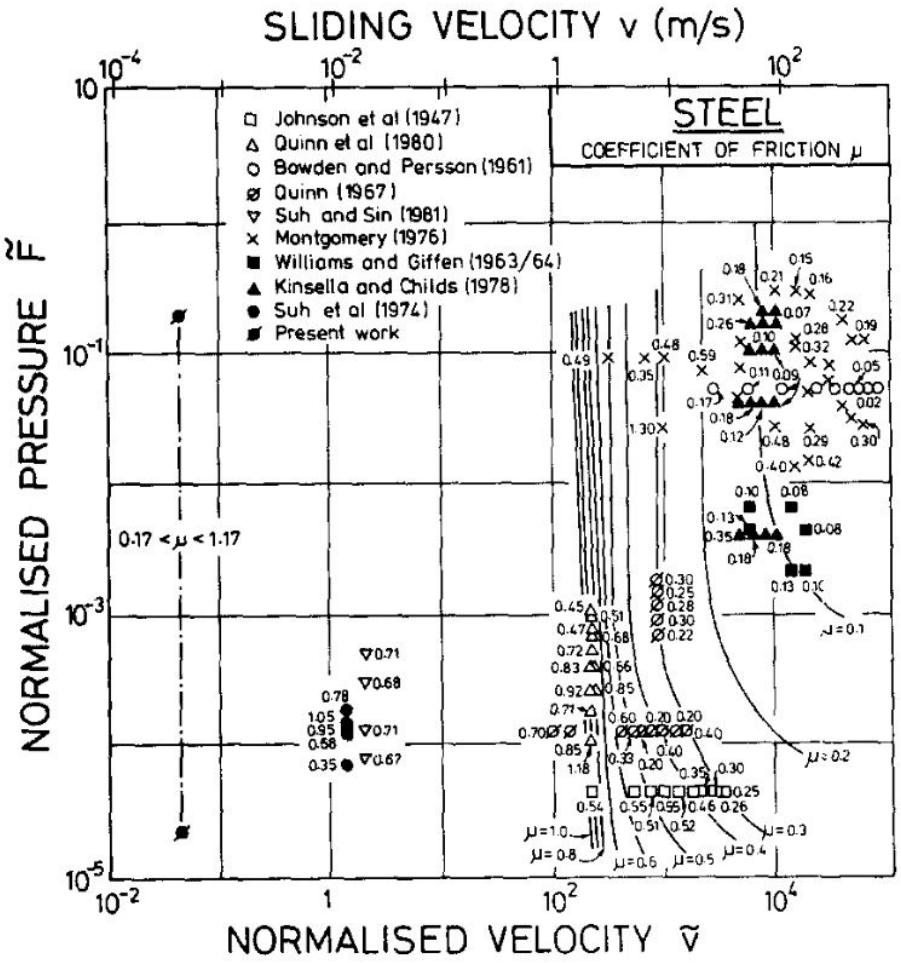

Figure 13. Lim and Ashby COF Data [39]

They developed the following expression for the coefficient of friction based on the experimental results shown in Figure 14.

$$\mu = 0.78 - 0.13\log\tilde{v} \tag{15}$$

As the normalized velocity (Equation 13) is a function of velocity, specimen radius, and thermal diffusivity, the coefficient of friction may not be constant given certain testing scenarios. As the curve approaches values of higher normalized velocity, the coefficient of friction decreases. These values fall below the values observed by Montgomery, denoted by the markers 'x' on the chart.

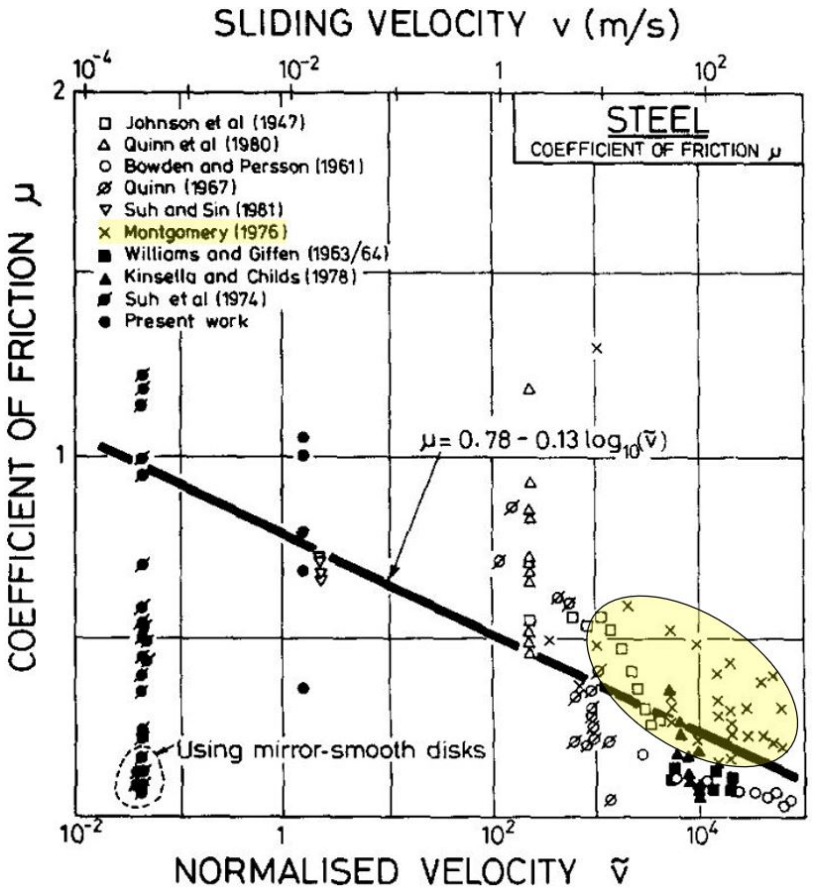

Figure 14. Lim and Ashby COF Interpolation [39]

2.5 AFIT Research

The problem regarding wear in high-velocity, high pressure regimes specific to those experienced at the HHSTT has been an ongoing area of AFIT research since 2002. This began with consideration of mostly mechanical aspects of wear and focused on asperity

collisions and gouging, with little regard to temperatures in works performed by Laird [36], Lofthouse [40], Szmerekovsky [51], and Cinnamon [15]. In 2006, Cameron [12] was the first to develop a one-dimensional finite-difference heat transfer model in MATLAB to fully incorporate temperature distributions and analyze the contributions of melt wear. He also incorporated simulated conditions that the rocket sled would experience as produced by the Dynamic Analysis and Design System (DADS), which is capable of modeling real-world mechanical systems. This simulated data provided approximations for loading and velocity conditions that the sled would experience, as real data was not possible to collect for this type of test run. The force data, as a function of time, used in the one-dimensional heat transfer model is shown in Figure 15. A positive (blue) force is associated with slipper/rail contact, while a negative (red) force is commensurate with a bouncing condition.

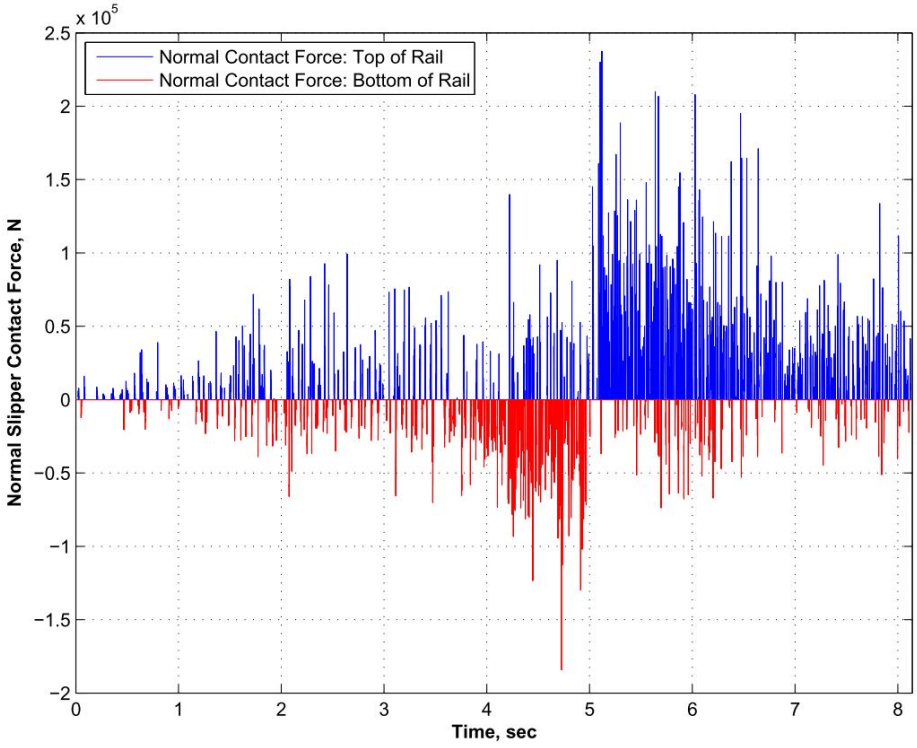

Figure 15. DADS Output for Slipper/Rail Contact Forces [25]

During the first five seconds of sled travel, the rocket motors are firing and the sled is accelerating down the track, contributing to the increasing propensity for the sled to become

airborne and the slipper to encounter a bounce condition. At approximately the five second mark, the rocket motors cease firing and the sled enters a deceleration phase, leading to increased positive forces on the slipper.

In 2012 Hale [25] improved the MATLAB code by accounting for the bouncing phenomena experienced by the test sled as it travels down the rail. Due to a small gap between the wraparound slipper and the rail (Figure 1b), the aerodynamic effects of the sled will cause the bottom of the slipper to lift up from the rail surface, causing a no-contact "bounce" condition in which the slipper will no longer be subject to conductive heat flux and will experience a convective effect due to the air flow through the gap. This bouncing, no-contact condition was accounted for through use of the DADS generated data as input for the computational model. As shown in Figure 15, this occurs with highest frequency between $t \in [3.5, 5]$ where the sled reaches its highest velocities. Hale also incorporated work performed by Montgomery to more accurately characterize the coefficient of friction calculations used in the heat transfer model. Continuing use of the pressure-velocity term, Hale fit the curve shown in Figure 16 and given by Equation 16 to Montgomery's work to determine coefficient of friction values based on the DADS produced data for the rocket sled.

$$\mu = \begin{cases} 0.2696e^{-3.409\cdot10^{-7}Pv} + 0.3074e^{-6.08\cdot10^{-9}} & 0 < Pv < 4.45\cdot10^{8} \\ 0.02 & Pv \geq 4.45\cdot10^{8} \end{cases} \tag{16}$$

Hale's work assumed a constant partition value of $\beta = 0.5$ (see Equation 11), which directs 50% of the heat generated into the slipper and 50% into the rail.

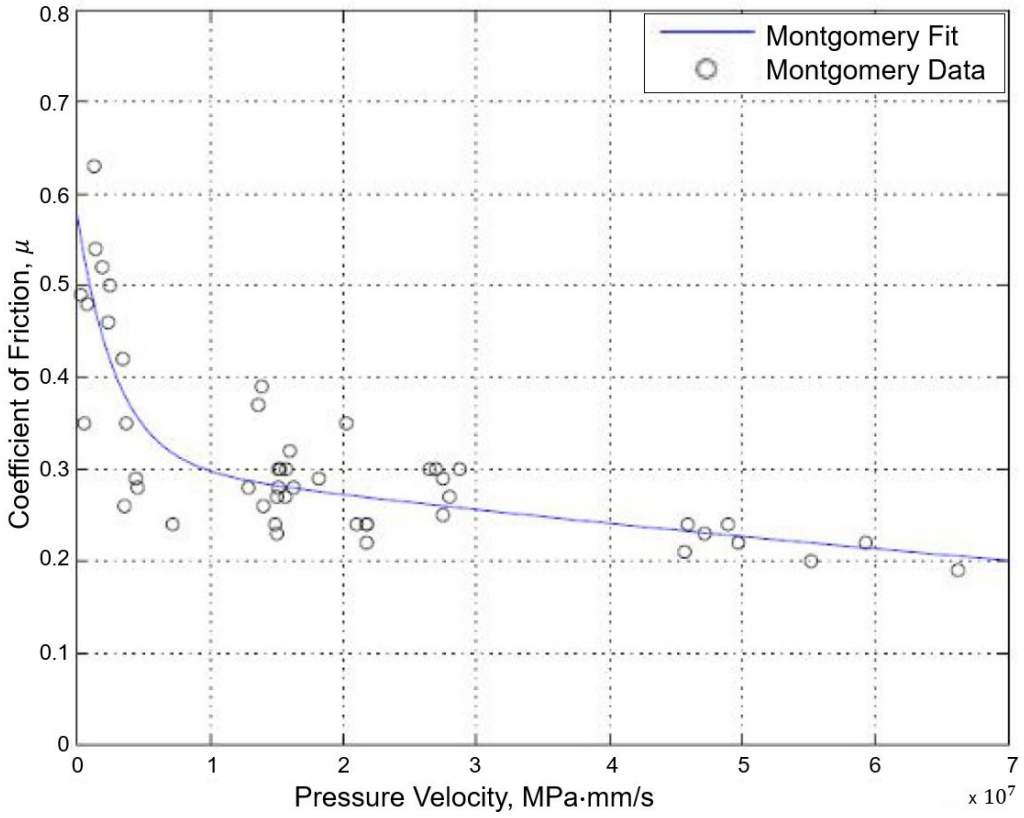

Figure 16. Friction as a function of pressure-velocity [25]

2.5.1 Heat Partition Function

Further improvements to the one-dimensional MATLAB model drove the requirement for a more appropriate partition function to accurately assess slipper wear measured after an actual test run when compared model predicted melt wear. The dynamic nature of the sled traveling down the rail, to include non-constant contact due to bouncing, presents a magnified degree of complexity in determining how to accurately characterize the division of heat. In 2013 Paek-Spidell [45] analytically and functionally investigated the heat partitioning function to better describe the slipper-rail interaction in the rocket sled system. This incorporated work performed by Carslaw and Jaeger [14] which assumes equal surface temperatures of the two bodies along the contact interface. Paek-Spidell then used a numerical method to account for the time-dependent nature associated with a continuously

changing heat flux. The proposed partition function considered the relation of material properties of the rail and slipper, and a constant non-dimensional velocity term. The model produced melt wear was then compared with physical measurements of material loss experienced by a slipper recovered following a 2008 test run at the HHSTT to produce the hypothesized time-dependent partition function

$$\beta(t) = 0.4e^{-5t^2} + 0.1. \tag{17}$$

The total amount of heat generated by friction is described by Equation 10. It was hypothesized through Equation 17 that initially the amount of heat flux into the sample is 50% of the total amount generated, and decays as a function of time to approximately 10% of the amount generated. This is due to the difference in surface temperatures between the rail and the slipper initially having a value of zero, but as time progresses the slipper temperature becomes much greater than the relatively constant temperature of the rail and therefore, less heat will flow into the slipper.

Le [38] further investigated the approximation methods for the partition function using test sled runs and corresponding wear rate results collected by Wolfson [55] during metal testing in the 1960s. Le considered linear, power, and exponential decaying partition functions and concluded that the exponential function proposed by Paek-Spidell (Equation 17) proved to be the closest match. Equation 17 is the partition function used in research regarding the HHSTT up to this point in time.

2.5.2 One-Dimensional MATLAB Algorithm

Until 2018 the MATLAB thermal model only accounted for constant valued material properties. To refine the model, DeLeon [17] incorporated the temperature dependent material properties for Vascomax® 300 that will be discussed in Section 2.6. DeLeon also modified the algorithm to include more accurate calculations of material removal due to

melt, through an iterative interpolation and solution process once melt temperatures were reached at the surface.

The one-dimensional MATLAB code was discretized with a fixed distance between nodes and solved via a second-order, explicit finite-difference scheme (meaning the temperature at each node for a given time step is determined as a function of the nodes around it [11]). The one-dimensional discretization is shown in Figure 17 and represents a single vertical slice through the slipper, with the base node located at slipper/rail interface. The domain spanned 100 vertical nodes and did not range over the entire depth of the slipper, but rather was chosen based off a maximum heat diffusion length that was calculated for the duration of the 2008 test event. This diffusivity depth y^* is defined by

$$y^* = \max_{U_\infty < U < U_{melt}} \sqrt{\frac{\hat{k}(U)}{\rho_s \hat{c}_p(U)} t^*} \tag{18}$$

and represents the maximum value achieved over the possible temperature ranges and the time duration of the test scenario, given by t^*. Throughout the algorithm, the node at this diffusivity depth (node 100 in Figure 17) is held at ambient temperature creating a constant value boundary condition. The code also included a moving boundary condition to facilitate the removal of material when the surface reached melt temperatures. The amount of material removed at a given time step when reaching melt temperatures was calculated by interpolation and is illustrated by the distance u_m. Upon removal, the entire nodal system is shifted by u_m to maintain a fixed distance between nodes. This one-dimensional model essentially represents a section out of the slipper in which the lateral sides are insulated, as it does not account for heat flow in the x or z dimensions.

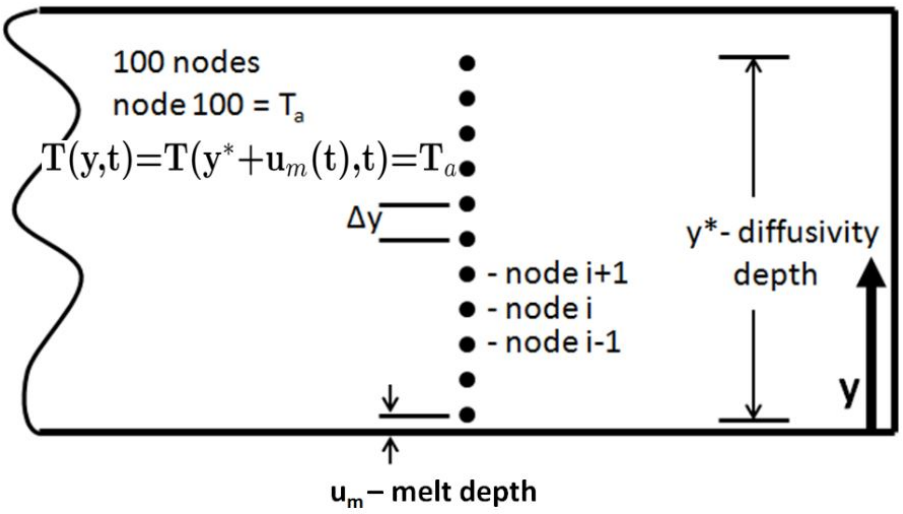

Figure 17. One-Dimensional Discretization [17]

2.6 Material Properties

Research specific to hypersonic rocket sled development performed by Graff and Dettloff was used to determine damage characteristics of both the rail and slippers regarding "gouging" phenomena [22]. It was determined that the choice of slipper material had some effect on this damage and that slippers manufactured from high strength maraging steel would be less likely to produce gouges [35].

Vascomax® 300 is also known as Maraging 300, where "maraging" describes a type of steel that is fully martensitic and strengthened by aging. The primary element is $\sim$18% Ni, which gives it ductility. The remaining elements include Co, Mo, Ti, and Al, which give it high strength characteristics. Vascomax® 300 is surface annealed at 815°C (1500°F) for one hour and heat treated at 482°C (900°F) for six hours. This process allows the material to evenly distribute all the alloying elements and then strengthens the material [26]. Table 2 is a listing of material properties for Vascomax® 300 used in past research [4, 12, 15, 25, 38]. Known values of specific heat as a function of temperature are shown in Table 3. There is little other published data on material properties over temperature ranges beyond 800 K, as a result the behavior of Vascomax® 250 and AISI 4130 data were used to estimate the

properties for Vascomax® 300. The specific heat and thermal conductivity are of primary concern during heat transfer analysis. Previous work yields estimates for these properties based on the behavior of the materials previously mentioned and is shown in Figure 18. The rise and then drop in values for specific heat is caused by a solid-solid phase change that the material undergoes as it transitions from martensite to austenite crystalline structure [26]. Density is assumed to be independent of temperature. Material properties for the disc are shown in Table 4 and will be considered constant for the duration of the experiment.

Table 2. Vascomax® 300 Material Properties [1]

Property	Value
Density	8000 kg/m^3
Melt Temperature	1685 K
Thermal Conductivity	30.807 W/(m $\cdot$ K)

Table 3. Vascomax® 300 Specific Heat [26]

Temperature (K)	Specific Heat, $\hat{c}_p$ (J/kg $\cdot$ K)
298	360
422	481
598	599
700	858

Table 4. AISI 4340 Steel Material Properties [2]

Property	Value
Density	7750 kg/m^3
Specific Heat	502 J/(kg $\cdot$ K)
Thermal Conductivity	41.8 W/(m $\cdot$ K)

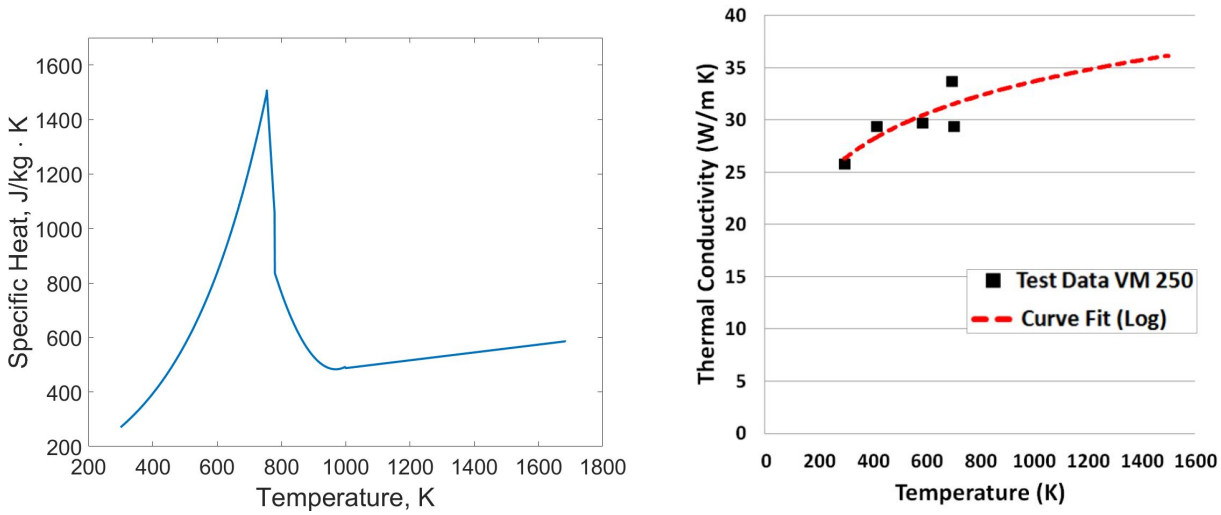

(a) Specific Heat (b) Thermal Conductivity

Figure 18. Temperature Dependent Material Properties [17]

2.7 Convective Effects

Convection plays an important role in the evaluation of bulk temperatures and when dealing with large-scale (as opposed to asperity-level) heat transfer effects [33]. In studies supporting the consideration of slipper wear at the HHSTT, Alban [4] extensively explored the role of convective effects and parameters associated with convection. This directly depends on the convective heat transfer coefficient h, which is affected by many dynamic conditions present in the boundary layers that develop along the surfaces. For a spinning disc at high speeds, the boundary layer is thin and the effect of curvature is negligible [58]. Notwithstanding, determination of h is a complicated undertaking in itself and is difficult to measure even in controlled experimental conditions. To aid in understanding the influence of this boundary layer and convective effects on the heat transfer within the system, the following dimensionless parameters are needed (and will subsequently be applied in Section 2.8):

1. Reynolds Number [7]: In determining characteristics within the boundary layer of air flow created by the spinning disc, the Reynolds number (Re_Ω) represents the ratio

of inertia to viscous forces and is defined as

$$Re_{\Omega} = \frac{\Omega R^2}{\nu_f} \tag{19}$$

where Ω is the angular velocity (rad/s), ν_f is the kinematic viscosity of air (m^2/s), and R is the radius of the spinning disc (m).

2. Nusselt Number [7]: The mean Nusselt number (Nu_m) is a dimensionless parameter characterizing the measure of convection heat transfer at a surface defined by

$$Nu_m = \frac{hR}{k_f} \tag{20}$$

where k_f (W/m·K) is the thermal conductivity of the fluid (air).

For fully turbulent cases ($5x10^5 \leq Re_{\Omega}$), a suitable correlation characterizing heat transfer from a rotating disc in still air was found by aus der Wiesche [5], given by

$$Nu_m = 0.015 Re_{\Omega}^{0.8}. \tag{21}$$

3. Biot Number [7]: The Biot number (Bi) is a dimensionless parameter describing the ratio of the internal thermal resistance of the solid to the boundary layer thermal resistance, expressed as

$$Bi = \frac{hR}{k}. \tag{22}$$

We define Bi_d and Bi_p as the Biot numbers of the disc and pin, respectively. The distinction is made due to the fact that the boundary layer created by the spinning disc will be relatively thin and the majority of the exposed length of the pin will be subject to free convection created by buoyancy forces within the air due to the

temperature differences ($h \approx 25$ W/m$^2\cdot$ K) [30]. The convection coefficient for the disc, h_d, can be determined through use of Equations 20 and 21.

4. Peclet Number [7]: The Peclet number (Pe) provides the ratio of advection to conduction heat transfer rates, defined as

$$Pe = \frac{vR}{\alpha}. \tag{23}$$

.

These parameters play an important role in the propagation of thermal energy into and out of the specimen. They also influence the behavior of partitioning of heat within the system, which will be further explored in Section 2.8. While Section 2.5.1 discussed heat partitioning specific to the HHSTT, further exploration is required to evaluate this parameter in regards to the current research concerning a pin-on-disc scenario.

2.8 Partitioning of Heat

The partitioning of heat flow into the sample versus into the disc involves consideration of mechanical, thermophysical and geometrical characteristics and is more accurately characterized as time dependent [44]. Heat partitioning can be expressed as a function of geometry, velocity, convective effects, and material properties [33]. There have been many efforts to analytically and numerically solve the partitioning of heat for pin-on-disc type experiments, with the majority of studies based on works originally performed by Blok [10] and Jaeger [29] which involve various analytical techniques matching asperity temperatures along the contact interface of sliding surfaces. Blok considered the maximum interface temperatures when deriving Equation 24 while Jaeger equated the average temperatures over the contact area, arriving at Equation 25. These expressions for $1-\beta$ represent

the amount of heat flowing into the moving body (the disc in a pin-on-disc configuration), given by

$$1-\beta=\frac{\frac{1}{2}\left(1-\frac{1}{\sqrt{2}}\right)+\frac{k_2}{k_1}\sqrt{\frac{\pi}{2}\frac{vr_c}{4\alpha_2}}}{1+\frac{k_2}{k_1}\sqrt{\frac{\pi}{2}\frac{vr_c}{4\alpha_2}}} \tag{24}$$

and

$$1-\beta=\frac{k_1\sqrt{vr_c}}{1.125k_2\sqrt{\alpha_1}+k_1\sqrt{vr_c}} \tag{25}$$

where k is the thermal conductivity of the material, v is the velocity, r_c is the radius of the heat flow, α is the thermal diffusivity, and subscripts 1 and 2 represent the stationary and moving bodies, respectively. Of note, as the velocity increases the values $1-\beta$ approach 1, indicating that the majority of heat will flow into the moving body, with a decreasing fraction of heat entering the stationary body as velocity increases. From Jaeger's work, Lim and Ashby developed an approximate equation used in their wear map research which they deemed adequate, given by

$$\beta=\frac{1}{2+L\sqrt{\frac{\pi v}{8\alpha r_c}}} \tag{26}$$

where L is the distance between the heat input and heat sink. As expected, with increases in velocity the fraction of heat flowing into the stationary pin will decrease. Berry and Barber[8] also developed a similar expression using Blok and Jaeger's work as a basis, constructing the equation

$$1-\beta=\frac{k_1\sqrt{\frac{vr_c}{2\alpha}}}{k_1\sqrt{\frac{vr_c}{2\alpha}}+0.795k_2}. \tag{27}$$

The difficulty in completely determining a partition function in most investigations leads to the use of an approximation or slight modification to the previous expressions.

In most applications, studies have shown that maximum contact temperatures calculated using approximations generally agree with results obtained using more exact partitioning analysis [32]. These partition approximations consider the steady state condition, however it has been shown that in most sliding contact scenarios the steady state is reached in a short period of time, with the amount of time decreasing as the Peclet number increases [33].

Laraqi et al. [37] conducted both numerical and analytical analysis of heat partitioning factors as functions of *Bi* and *Pe*. It was determined that beyond a certain threshold ($Pe \geq 30$) the speed does not significantly change the heat partition coefficient, and only the heat exchanges of the pin and the disc with their environment affect the value of the heat partition coefficient. Figure 19 represents the partitioning approximations when the pin and the disc have the same material properties, with the value $1-\beta$ along the vertical axis representing the fraction of heat flowing into the spinning disc.

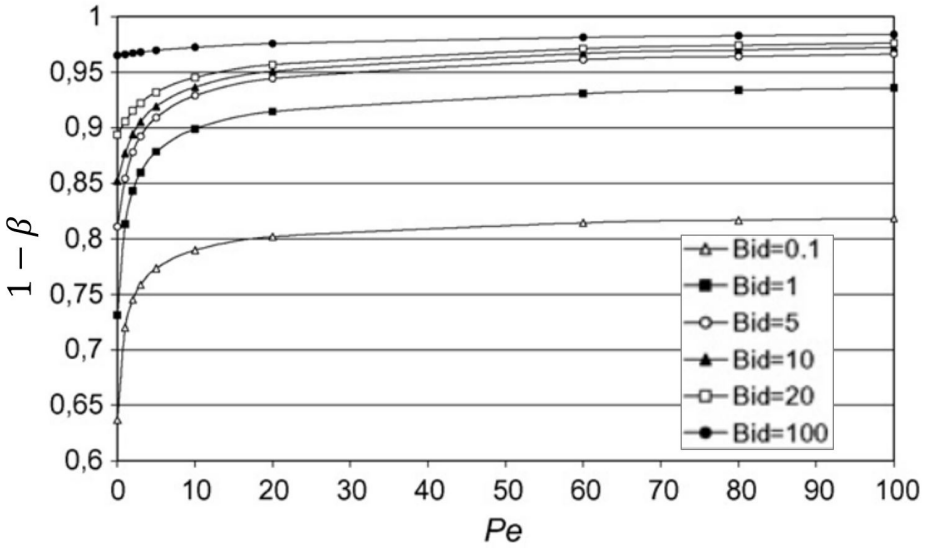

Figure 19. Heat Partitioning as a function of *Pe* for different disc Bi_d [37]

We can see a dependence on material properties of the pin in Figure 20 since the respective *Bi* are functions of the thermal conductivity of the material. The amount of heat flow into the disc increases with an increase in velocity, although as mentioned, beyond a certain threshold ($Bi_d = 10$) this value does not as heavily influence the partition coefficient.

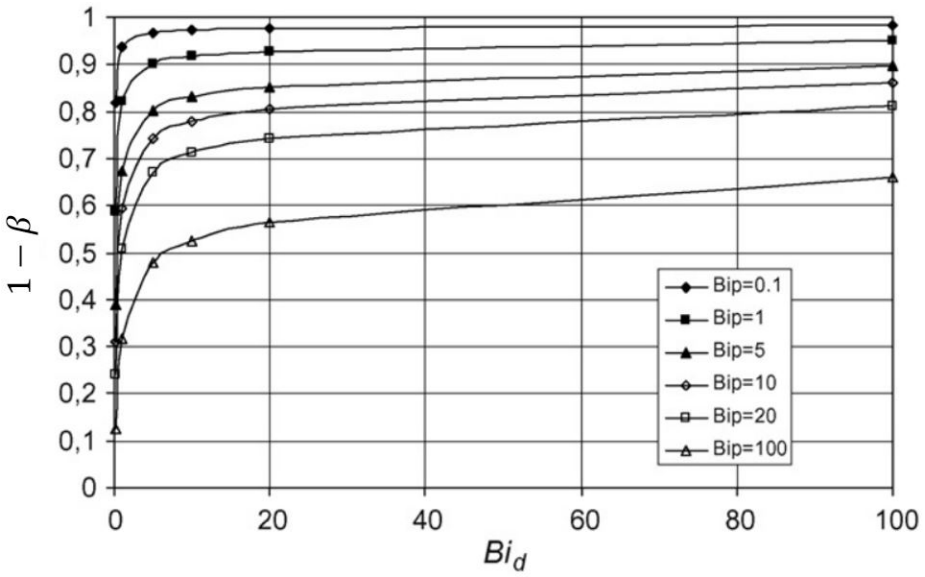

Figure 20. Heat Partitioning as a function of Bi_d for different pin Bi_p [37]

Finally, Waddad et al. [53] considered the time evolution of the partition coefficient with fixed angular velocities and different ratios of thermal diffusivity between the contacting materials, with similar conclusions. Figure 21 shows their results with χ_1 and χ_2 representing the thermal diffusivities of the moving disc and stationary pin, respectively, and p_1 representing the partitioning of heat into the moving disc. Here we see that for a fixed value for the thermal diffusivity of the disc (χ_1) and constant velocity, decreasing the thermal diffusivity of the pin results in decreasing fractions of heat flowing into the pin. As expected, increases in velocity result in a higher fraction of heat flowing into the disc.

These results have been corroborated through other analytical, numerical, and experimental research [23, 30, 31, 34, 56, 57]. In particular, Grosberg and Molgaard [23] recorded experimental values between 3 and 10 percent through pin-on-ring testing at speeds up to 40 m/s. They observed that experimental values rose quite sharply with increases in loading. When comparing their results to theoretical values, they noted discrepancies they attributed to the undetermined effect of oxide layers on the division of heat. Similar ranges were recorded during grinding processes by Guo and Malkin [24].

Regardless of the methods of approximation for the partitioning of heat, the value re-

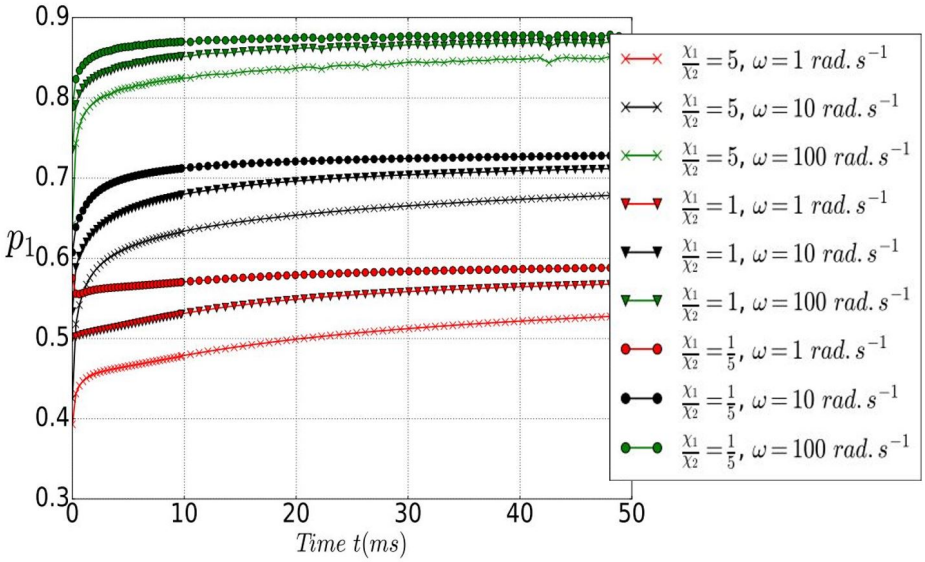

Figure 21. Heat Partitioning as a function of Angular Velocity and Thermal Diffusivity Ratios [53]

mains sensitive to the mechanical, thermal, and chemical interactions taking place within the contact boundary. Consideration will be given to the approximations described in this section in regards to the parameters observed and predicted by the experiment, and subsequent results of the thermal model.

2.8.1 Critical Temperature Estimation

During their attempt to determine the presence of friction decreases at high sliding speeds, Carignan and Rabinowicz [13] briefly investigated the effects of interface temperature on the coefficient of friction and wear rates. Using experimental data, they encountered difficulty when attempting to quantify the effects of temperatures on the friction and wear processes, but acknowledged that temperature effects, although unpredictable, were of moderate effect at temperatures below melt. However, when the surface reaches melting temperature, “the wear of the melting surface increases drastically” [13].

Study relating surface temperatures and wear rates has also been conducted in railway research projects, among other sliding contact systems. Most approaches in this regard focus on flash heating and localized temperatures at the asperity level [52]. Other investi-

gations of temperature effects on wear involve varying the temperature distribution of the materials through means other than frictional heating to study wear rates at different material temperatures [19]. Sundh and Olofsson [50] also conducted pin-on-disc testing to study different wear mechanisms, hypothesizing that contact temperatures could aid in explaining wear transitions between mild and severe regimes. Regardless of the specific nature of these experimental tests, the principles revolve around evaluating the effect of temperature of materials in sliding contact and corresponding wear. Although previous investigations generally involve velocities and forces less than those in question, implementing a thermal energy approach to determine wear characteristics remains applicable.

Work similar in nature was conducted by DeLeon [17] using computer generated force and velocity data simulating a 2008 test run at the HHSTT as input. DeLeon developed a one-dimensional heat transfer model to characterize predicted melt at the surface of a slipper in comparison to actual damage determined by measurement and analysis of a slipper recovered following the test run. That model was formulated under the assumption that material would not be removed until the surface reached melt temperatures.

Predicting material wear at temperatures below a material's melt temperature implies that wear is primarily mechanical in nature. In order to use a thermal model to evaluate wear, an equivalent temperature was considered to decouple the effects of mechanical wear and evaluate the solution exclusively on the flow of heat (generated by friction) within the system. Thus, it is hypothesized in the development of this model that there is a critical temperature value below the melt temperature of the pin that will accurately characterize the material removal process.

III. Two-Dimensional Mathematical Model

3.1 Chapter Overview

This chapter details the mathematical principles explored in this research. Specifically, this model applies the heat diffusion equation and approximates the modes of heat transfer of conduction and convection. Conduction is the transfer of energy that takes place between mediums when a temperature gradient exists. In the case of the pin-on-disc scenario, this temperature gradient arises due to the frictional heat generated upon sliding contact and will determine one of the boundary conditions associated with the model. Heat transfer from convective effects occurs when a temperature gradient exists between a fluid and another surface, and will be used to describe another set of boundary conditions within the model. The assumptions outlined in this chapter will allow formulation of a numerical model to approximate the heat transfer and the temperature distribution within the pin.

3.2 Governing Equations

3.2.1 Heat Diffusion Equation

By the Law of Conservation of Energy and eliminating the effects of material deformation we have the general form of the heat diffusion equation, as described in Section 1.6.3, given by [7]

$$\rho_s \hat{c}_p(U) \frac{\partial U}{\partial t} = \nabla \cdot (\hat{k} \nabla U) + q_g \tag{28}$$

where U is the temperature (K), t is time (s), ρ_s is the material mass density (kg/m^3), $\hat{c}_p$ is the specific heat as a function of temperature (J/kg·K), $\hat{k}$ is the thermal conductivity (W/m·K), and q_g is the rate at which energy is generated. Suppose thermal conductivity is a function of temperature, then $\hat{k} = \hat{k}(U)$. Assuming no energy generation, the diffusion

equation then becomes

$$\begin{aligned}\rho_s \hat{c}_p(U)\frac{\partial U}{\partial t} &= \nabla\cdot(\hat{k}\nabla U)\\ &= \hat{k}(\nabla\cdot\nabla U)+\nabla\hat{k}\cdot\nabla U\\ &= \hat{k}(U)\nabla^2 U+\frac{d\hat{k}}{dU}(U)\left|\nabla U\right|^2. \end{aligned} \tag{29}$$

In cylindrical coordinates

$$\nabla^2 U=\frac{\partial^2 U}{\partial r^2}+\frac{1}{r}\frac{\partial U}{\partial r}+\frac{1}{r^2}\frac{\partial^2 U}{\partial \phi^2}+\frac{\partial^2 U}{\partial z^2} \tag{30}$$

and

$$\left|\nabla U\right|^2=\left(\frac{\partial U}{\partial r}\right)^2+\frac{1}{r^2}\left(\frac{\partial U}{\partial \phi}\right)^2+\left(\frac{\partial U}{\partial z}\right)^2, \tag{31}$$

where r, z, and ϕ are the cylindrical coordinates of radius, axial length, and azimuth, respectively. Dividing by $\hat{k}(U)$ and substituting Equations 30 and 31 into Equation 29, we have the heat equation in cylindrical coordinates expressed as

$$\underbrace{\frac{1}{\hat{\alpha}(U)}}_{\text{non-linear}}\frac{\partial U}{\partial t}=\underbrace{\frac{\partial^2 U}{\partial r^2}+\frac{1}{r}\frac{\partial U}{\partial r}+\frac{1}{r^2}\frac{\partial^2 U}{\partial \phi^2}+\frac{\partial^2 U}{\partial z^2}}_{\text{linear}}+\underbrace{\frac{d\hat{k}}{dU}(U)\frac{1}{\hat{k}(U)}\left[\left(\frac{\partial U}{\partial r}\right)^2+\frac{1}{r^2}\left(\frac{\partial U}{\partial \phi}\right)^2+\left(\frac{\partial U}{\partial z}\right)^2\right]}_{\text{non-linear}} \tag{32}$$

where $\hat{\alpha}(U)$ is the thermal diffusivity of the material (m^2/s) given by the ratio $\dfrac{\hat{k}(U)}{\rho_s \hat{c}_p(U)}$, measuring the ability of the material to conduct thermal energy relative to its ability to store thermal energy. Note, the parameters $\hat{\alpha}$, $\hat{k}$, and $\hat{c}_p$ are functions of temperature, U, which leads to the non-linearities that arise in Equation 32.

Figure 22 represents the behavior of the thermal diffusivity of Vascomax® 300 as a

function of temperature, developed from prior work performed by DeLeon [17] and discussed in Section 2.6. The variations are largely driven by the change in specific heat as the temperature increases which, as previously mentioned, is caused by phase and structure transitions that occur as the material's temperature approaches 800 K.

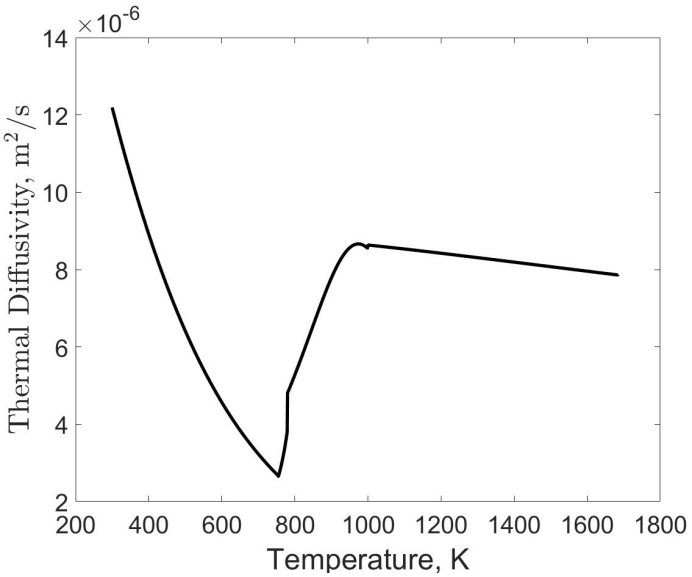

Figure 22. Thermal Diffusivity

3.2.2 Boundary Conditions

On the boundary of the cylinder, the heat loss due to convection (W/m^2) is determined by Newton's Law of Cooling given by Equation 3, $q''(t) = h(U_s - U_\infty)$. Thus, the convective heat flux is proportional to the difference between the surface and ambient temperatures, U_s and U_∞ respectively, multiplied by the convection heat transfer coefficient h (W/m$^2\cdot$ K), which depends on the conditions in the boundary layer. This equation is also used to describe the heat flow from the flat face of the sample when it is not in contact with the spinning disc. We define h_r to be the convection coefficient along the radial surface of the pin and h_c as the convection coefficient along the contact face of the sample when under a no contact condition.

The heat generated by friction will flow into the sample as governed by Fourier's law,

$$q''(t) = -\hat{k}(U)\frac{\partial U}{\partial z}. \tag{33}$$

This states that the heat flow is normal to the contact surface and in the direction of decreasing temperature.

3.2.3 Related Assumptions

The reference coordinate system is shown in Figure 23. From experimental observations and consistent with concepts developed in similar research for pin-on-disc systems, we make the following assumptions for a two-dimensional model in cylindrical coordinates:

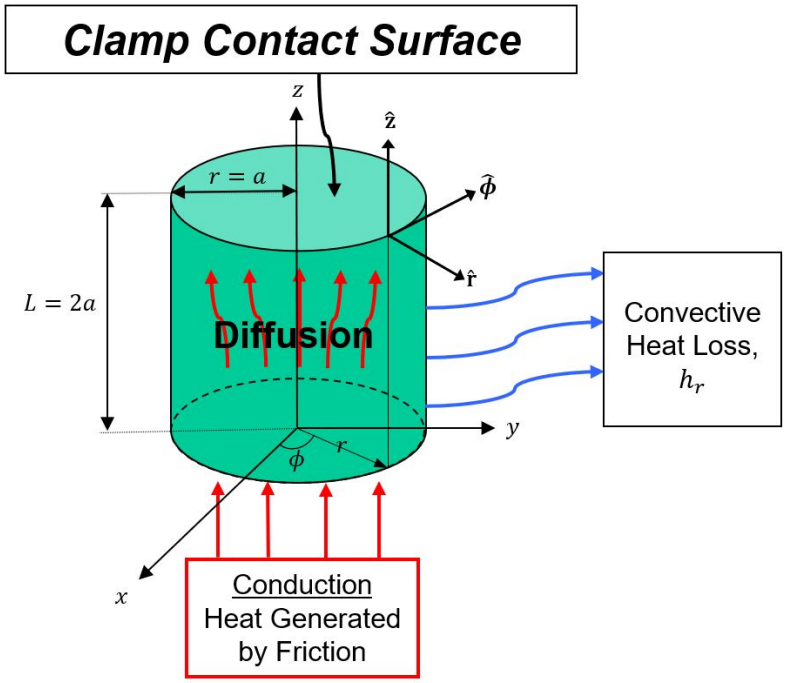

Figure 23. Cylindrical Coordinate System

1. All of the frictional energy is dissipated as heat at the contact interface [32].

2. The entire flat face of the pin is in contact with the surface of the disc and the friction

heat flux is generated uniformly across the face. Thus, the change in temperature distribution in the pin with respect to ϕ is negligible in comparison to the change with respect to the r and z components.

3. The convective heat transfer coefficients h_r along the radial surface of the pin, and h_c along the flat face of the pin when not in contact, are constant (that is, they have no dependence on the variables r or z).

4. The clamp at the top holding the pin in place acts as a heat sink due to its proportional size and material, resulting in a constant temperature boundary condition where the pin is held in the clamp [31].

5. The initial temperature of the test article is equivalent to the ambient temperature.

3.2.4 Partial Differential Equation

Under these assumptions the partial differential equation of interest reduces to

$$\frac{1}{\hat{\alpha}(U)}\frac{\partial U}{\partial t} = \frac{\partial^2 U}{\partial r^2} + \frac{1}{r}\frac{\partial U}{\partial r} + \frac{\partial^2 U}{\partial z^2} + \frac{d\hat{k}}{dU}(U)\frac{1}{\hat{k}(U)}\left[\left(\frac{\partial U}{\partial r}\right)^2 + \left(\frac{\partial U}{\partial z}\right)^2\right] \tag{34}$$

subject to the initial condition described by

$$U(r,z,0) = U_\infty \tag{35}$$

and boundary conditions:

$$\text{1) Conduction (Contact): } q''(t) = -\hat{k}(U)\frac{\partial U}{\partial z}\bigg|_{z=0} \tag{36}$$

2) Convection (Bounce): $-\hat{k}(U)\left.\frac{\partial U}{\partial z}\right|_{z=0} = h_c\left(U(r,0,t) - U_\infty\right)$ (37)

3) $\left.\frac{\partial U}{\partial r}\right|_{r=0} = 0$ (38)

4) $-\hat{k}(U)\left.\frac{\partial U}{\partial r}\right|_{r=a} = h_r\left(U(a,z,t) - U_\infty\right)$ (39)

5) $U(a,L,t) = U_\infty$ (40)

where a is the radius of the sample and L is the exposed length of the sample. In the case currently considered, $L = 2a$.

3.2.5 Scaling

Scaling factors are used in many numerical applications and are especially useful in transient solutions [7]. These dimensionless parameters can reduce the complexity of numerical calculations and analytical solutions by generalizing the problem, and provide insight as to the degree of influence that variables of differing orders of magnitude have on the solution. Introducing the following scaling factors simplifies the PDE and associated conditions. Define:

1. Length: $\xi = \frac{z}{a}, \qquad 0 \leq \xi \leq 2$

2. Radial: $\rho = \frac{r}{a}, \qquad 0 \leq \rho \leq 1$

3. Temperature: $\theta\left(\frac{r}{a},\frac{z}{a},t\right)=\frac{U(r,z,t)-U_\infty}{U_{crit}-U_\infty}, \qquad 0\le\theta\le 1$

4. Time: $t\ge 0$.

As $\hat{k}$ and $\hat{\alpha}$ are functions of U, let

$$\alpha(\theta)=\hat{\alpha}\Big(U_\infty+(U_{crit}-U_\infty)\theta\Big) \tag{41}$$

and

$$k(\theta)=\hat{k}\Big(U_\infty+(U_{crit}-U_\infty)\theta\Big). \tag{42}$$

The re-scaled PDE becomes

$$\frac{\partial\theta}{\partial t}=\frac{\alpha(\theta)}{a^2}\left(\frac{\partial^2\theta}{\partial\rho^2}+\frac{1}{\rho}\frac{\partial\theta}{\partial\rho}+\frac{\partial^2\theta}{\partial\xi^2}+\frac{dk}{d\theta}(\theta)\frac{1}{k(\theta)}\left[\left(\frac{\partial\theta}{\partial\rho}\right)^2+\left(\frac{\partial\theta}{\partial\xi}\right)^2\right]\right) \tag{43}$$

subject to initial condition

$$\theta(\rho,\xi,0)=0 \tag{44}$$

and boundary conditions:

1) Conduction (Contact): $\left.\frac{\partial\theta}{\partial\xi}\right|_{\xi=0}=-Q(\theta,t)$ (45)

where

$$Q(\theta,t) = \frac{aq''(t)}{k(\theta)(U_{crit} - U_{\infty})} \tag{46}$$

and $q''(t)$ is defined by Equation 11.

2) Convection (Bounce): $-k(\theta)\left.\frac{\partial\theta}{\partial\xi}\right|_{\xi=0} = h_c\theta(\rho,0,t)$ (47)

3) $\left.\frac{\partial\theta}{\partial\rho}\right|_{\rho=0} = 0$ (48)

4) $-k(\theta)\left.\frac{\partial\theta}{\partial\rho}\right|_{\rho=1} = ah_r\theta(1,z,t)$ (49)

5) $\theta(\rho,2,t) = 0.$ (50)

This is an initial value problem subject to a Dirichlet boundary condition at $\xi = 1$ and Nuemann conditions at $\rho = 0$, $\rho = 1$, and $\xi = 0$.

IV. Two-Dimensional Numerical Model

4.1 Numerical Model

A standard way to solve PDEs is through the use of numerical approximations for the respective derivatives. These are developed from Taylor Series expansions from Taylor's formula

$$f(x) = \sum_{n=0}^{\infty} \frac{f^{(n)}(b)}{n!}(x-b)^n \tag{51}$$

for a function f about the point b. This can also be expressed as

$$f(x) = \sum_{n=0}^{k} \frac{f^{(n)}(b)}{n!}(x-b)^n + \underbrace{\sum_{n=k+1}^{\infty} \frac{f^{(n)}(b)}{n!}(x-b)^n}_{R_n(x)} \tag{52}$$

where $R_n(x)$ is the remainder term if the series is truncated at $n = k$ terms. Then the Taylor expansions for $f(x+b)$ and $f(x-b)$ are

$$f(x+b) = f(x) + f^{'}(x)b + \frac{f^{''}(x)b^2}{2} + R_3(x) \tag{53}$$

and

$$f(x-b) = f(x) - f^{'}(x)b + \frac{f^{''}(x)b^2}{2} + R_3(x) \tag{54}$$

where $R_3(x)$ is of order $\mathcal{O}(b^3)$. Subtracting Equations 53 and 54 yields the central difference approximation for the first derivative, of the form

$$f^{'}(x) = \frac{f(x+b) - f(x-b)}{2b} + \mathcal{O}(b^2) \tag{55}$$

where $\mathcal{O}(b^2)$ represents the truncation error associated with the approximation. This is defined as the amount in which the solution fails to satisfy the finite difference equation

and depends on the step size taken spatially. Solving for the approximation for the second derivative in a similar manner yields

$$f''(x) = \frac{f(x+b) - 2f(x) + f(x-b)}{b^2} + \mathcal{O}(b^2). \tag{56}$$

Equations 55 and 56 represent the central difference formulas of order $\mathcal{O}(b^2)$ that will be used to numerical solve the PDE. For transient problems, the size of the time steps taken not only impacts the accuracy of the solution, but also influences the stability when using explicit solution methods which depend on previous iterations.

4.2 Runge-Kutta Methods

The method implemented to solve Equation 43 numerically requires reducing the PDE into a system of ordinary differential equations (ODEs) of the form

$$\frac{d\vec{\theta}}{dt} = F\left(t, \vec{\theta}(t)\right). \tag{57}$$

The ODEs can then be solved using a number of various difference methods. One-step solution methods compute the solution using values of the previous step, $\vec{\theta}^{p-1}$, and possibly as a function of the current step $\vec{\theta}^{p}$, where p is the iteration with respect to time. The Runge-Kutta family of solvers are of the form

$$\vec{\theta}^{p+1} - \vec{\theta}^{p} = \triangle t \sum_{i=1}^{j} w_i \zeta_i \tag{58}$$

where j represents the order of the method and the w_i's are constants that specify the weights associated with the values ζ_i. Each ζ_i is a function of F (given by Equation 57) and represents an estimation for the slope of the curve at the specified incremental distances $\varepsilon_i \triangle t$ and $\sum_{s=1}^{i-1} c_{is}\zeta_s$ from the present values of t_p and $\vec{\theta}^{p}$, respectively. This is expressed as

$$\zeta_i = F\left(t_p + \varepsilon_i \triangle t, \vec{\theta}^p + \sum_{s=1}^{i-1} c_{is}\zeta_s\right), \tag{59}$$

with the values of ε_i and c_{is} chosen to match the Taylor series expansions of both sides of Equation 58 as closely as possible [46], giving the highest possible order of accuracy for the method. The parameters ζ_i are essentially estimates of the change in the solution as the step advances, because they are a product of the change in t and a value for the slope of the curve, $\frac{d\theta}{dt}$. Runge-Kutta methods are one-step methods since they require knowledge of only one previous iteration. Because of this, they do not have weak instability (further discussed in Section 4.3). They are self-starting and will converge to the true solution as the spatial steps decrease and approach zero [27].

4.3 Stability

Stability within a system can be described as how the introduction of small changes of input parameters effect the solution and whether or not these changes will cause divergence of the solution. Consistency describes the ability of the method to reproduce the original differential equation as the step size approaches zero. A method is considered stable when the numerical solution does not diverge 'dramatically' from the exact solution when iterated upon. When this condition depends on certain parameters or choices of initial data, the system is called conditionally stable [11]. Finite difference approximation methods are stable if the error in the solution goes to zero as the truncation error goes to zero [47]. In stable methods, early errors of imprecision of the method will be damped out as the numerical method proceeds and will not grow unbounded [21]. As explicit methods use solution values from the previous point or time step, the stability of the solution will depend on the step size taken as well as the discretization of the system. For forward difference approximations, the truncation error is of order

$$\mathscr{O}\left(\triangle t + (\triangle z)^2 + (\triangle r)^2\right). \tag{60}$$

The method is conditionally stable if and only if [47]

$$1 - \triangle t \left(\frac{2}{(\triangle z)^2} + \frac{2}{(\triangle r)^2}\right) \|\alpha(\vec{\theta})\|_\infty \geq 0. \tag{61}$$

Since the thermal diffusivity is a function of temperature, its maximum value over the range of temperatures is considered when determining the time step size. The restriction on the time increment in terms of the dimensionless parameters ρ and ξ is

$$\triangle t \leq \left(\left(\frac{2}{(a\triangle\xi)^2} + \frac{2}{(a\triangle\rho)^2}\right) \|\alpha(\vec{\theta})\|_\infty\right)^{-1}. \tag{62}$$

The primary inputs for the model will be data collected from the experimental tests (force, velocity, and displacement), sampled at 0.0005 second increments by the data acquisition system. Thus, it is desired to maintain this step size with respect to time within the numerical model. This leads to restrictions on minimum values for nodal spacing in the ρ and ξ dimensions when developing the discretized scheme described in Section 4.4, with $\triangle\rho$ and $\triangle\xi$ chosen such that

$$\frac{1}{(\triangle\xi)^2} + \frac{1}{(\triangle\rho)^2} \leq 3.58\text{x}10^3 \text{ m}^{-2}. \tag{63}$$

4.4 Discretization

To numerically solve for the temperature distribution of the pin, we define the 2-dimensional mesh of the pin for the ρ and ξ coordinates shown in Figure 24. We have M equally spaced nodes in the ρ dimension and N equally spaced nodes in the ξ dimension, with $m \in$ [1, M] and $n \in$ [1, N]. The "ghost points" $\{\theta_{0,n}\}_{n=1}^{N}$, $\{\theta_{m,N+1}\}_{m=1}^{M}$, and $\{\theta_{M+1,n}\}_{n=1}^{N}$ are points that are located exterior to the domain and are introduced so that

the boundary conditions can be approximated using the discretized scheme. The line of symmetry created along the centerline of the sample is as a result of azimuthal independence by our previously identified assumptions.

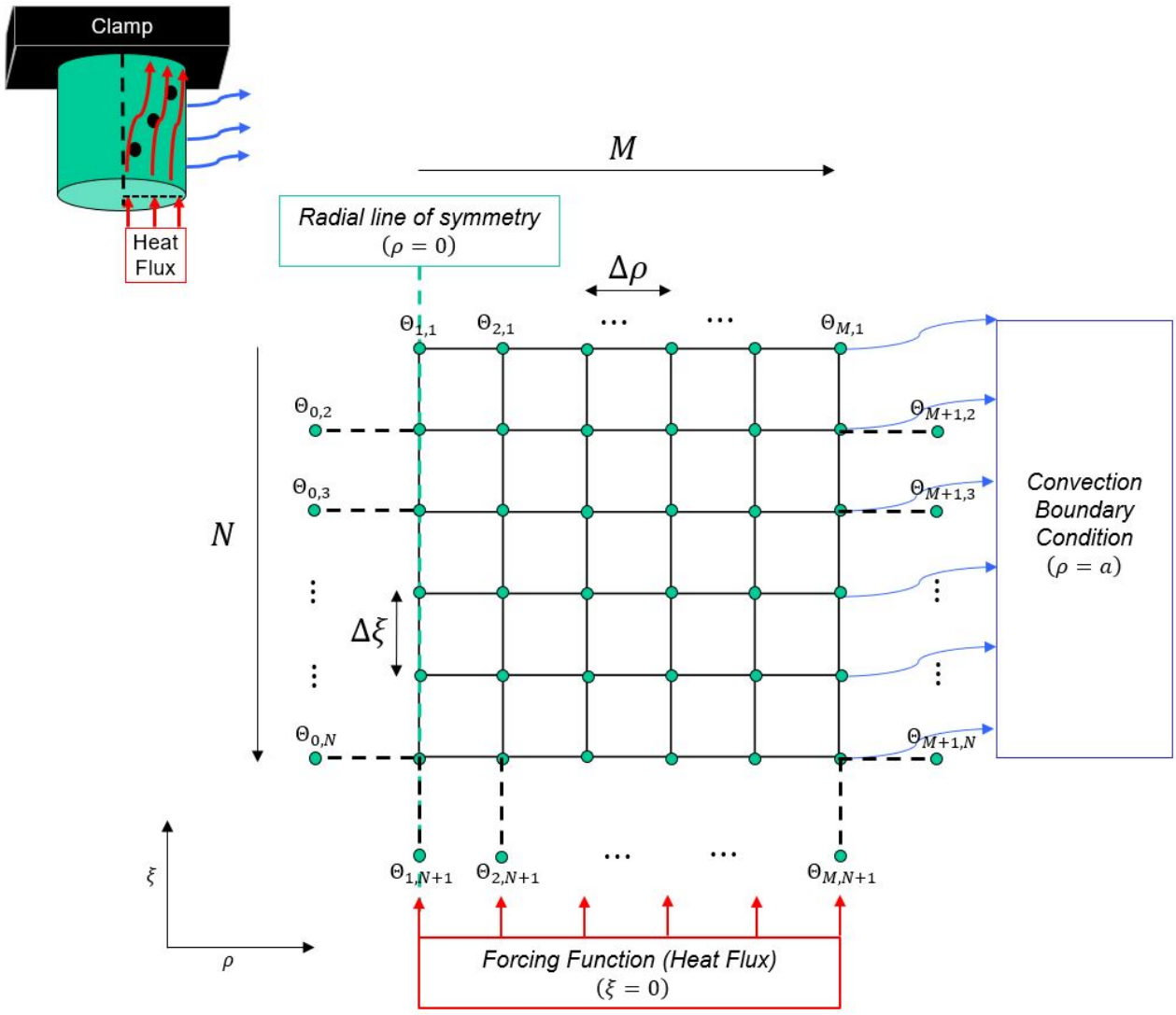

Figure 24. Nodal Network

We vertically concatenate the nodal rows to form the MN x 1 solution vector defined by Equation 64.

$$\vec{\theta}(t) = \begin{bmatrix} \theta_{1,1} \\ \theta_{2,1} \\ \vdots \\ \theta_{M,1} \\ \theta_{1,2} \\ \theta_{2,2} \\ \vdots \\ \theta_{M,2} \\ \vdots \\ \theta_{M,N-1} \\ \theta_{1,N} \\ \vdots \\ \theta_{M,N} \end{bmatrix} (t) \tag{64}$$

Due to the boundary condition associated with the specimen/clamp interface (Assumption 4), $\theta_{m,1} = 0$ for each m.

We now spatially discretize Equation 43 using the second order central difference approximations developed from Equations 55 and 56 for the respective derivatives, expressed as

$$\frac{\partial \theta}{\partial \rho} \approx \frac{\theta_{m+1,n} - \theta_{m-1,n}}{2\triangle\rho}, \tag{65}$$

$$\frac{\partial^2 \theta}{\partial \rho^2} \approx \frac{\theta_{m+1,n} - 2\theta_{m,n} + \theta_{m-1,n}}{(\triangle\rho)^2}, \tag{66}$$

$$\frac{\partial \theta}{\partial \xi} \approx \frac{\theta_{m,n+1} - \theta_{m,n-1}}{2\triangle\xi}, \tag{67}$$

and

$$\frac{\partial^2\theta}{\partial\xi^2} \approx \frac{\theta_{m,n+1} - 2\theta_{m,n} + \theta_{m,n-1}}{(\triangle\xi)^2}. \tag{68}$$

Substituting Equations 65 through 68 in Equation 43 yields the following stencil:

$$\begin{aligned}\frac{d\theta_{m,n}}{dt} = \frac{\alpha(\theta_{m,n})}{a^2}\left(\frac{\theta_{m+1,n} - 2\theta_{m,n} + \theta_{m-1,n}}{(\triangle\rho)^2} + \frac{1}{\rho_{m,n}}\frac{\theta_{m+1,n} - \theta_{m-1,n}}{2\triangle\rho} + \frac{\theta_{m,n+1} - 2\theta_{m,n} + \theta_{m,n-1}}{(\triangle\xi)^2}\right) \\ + \frac{dk}{d\theta}(\theta_{m,n})\frac{\alpha(\theta_{m,n})}{a^2k(\theta_{m,n})}\left[\left(\frac{\theta_{m+1,n} - \theta_{m-1,n}}{2\triangle\rho}\right)^2 + \left(\frac{\theta_{m,n+1} - \theta_{m,n-1}}{2\triangle\xi}\right)^2\right].\end{aligned} \tag{69}$$

The case of $\rho_{1,n} = 0$ will be dictated by the boundary condition along the radial line of symmetry. Expanding and defining the constant coefficients

$$\sigma = \frac{1}{(\triangle\xi)^2}, \tag{70}$$

$$\gamma = \frac{2}{(\triangle\rho)^2} + \frac{2}{(\triangle\xi)^2}, \tag{71}$$

$$\lambda = \frac{2}{(\triangle p)^2}, \tag{72}$$

$$\Psi = \frac{1}{4(\triangle\rho)^2}, \tag{73}$$

$$\Gamma = \frac{1}{4(\triangle\xi)^2}, \tag{74}$$

and functions

$$\psi_{m,n} = \frac{1}{(\triangle\rho)^2} + \frac{1}{2\rho_{m,n}\triangle\rho}, \tag{75}$$

$$\eta_{m,n} = \frac{1}{(\triangle\rho)^2} - \frac{1}{2\rho_{m,n}\triangle\rho}, \tag{76}$$

$$\Phi_{m,N} = 2Q(\theta_{m,N}, t)\triangle\xi, \tag{77}$$

$$\omega_{M,n} = \frac{2ah_r \triangle \rho}{k(\theta_{M,n})}, \tag{78}$$

$$X_{m,N} = \frac{-2ah_c \triangle \xi}{k(\theta_{m,N})}, \tag{79}$$

$$G_{m,n} = \frac{dk}{d\theta}(\theta_{m,n}) \frac{\alpha(\theta_{m,n})}{a^2 k(\theta_{m,n})}, \tag{80}$$

we have that Equation 69 can be solved by

$$\begin{aligned} \frac{d\theta_{m,n}}{dt} = & \frac{\alpha(\theta_{m,n})}{a^2} \left(\psi_{m,n}\theta_{m+1,n} + \eta_{m,n}\theta_{m-1,n} + \sigma\theta_{m,n+1} + \sigma\theta_{m,n-1} - \gamma\theta_{m,n} \right) \\ & + G_{m,n} \left[\Psi \left(\theta_{m+1,n} - \theta_{m-1,n} \right)^2 + \Gamma \left(\theta_{m,n+1} - \theta_{m,n-1} \right)^2 \right] \end{aligned} \tag{81}$$

subject to the boundary conditions in Equations 45 through 50, where $\psi_{m,n}$ accounts for interior nodal dependence in the $n+1$ radial direction, $\eta_{m,n}$ accounts for interior nodal dependence in the $n-1$ radial direction, σ accounts for nodal dependence in the ξ dimension, γ accounts for the contribution of the solution node, $\Phi_{m,N}$ is the heat flux boundary condition when in contact, $\omega_{M,n}$ accounts for the convective condition at $\rho = a$, λ is a result of the symmetry condition along the centerline $\rho = 0$, $X_{m,N}$ accounts for the convective condition at $\xi = 0$ when the sample is not in contact, Ψ accounts for the nonlinear contribution in the ρ dimension, and Γ accounts for the nonlinear contribution in the ξ dimension. The function $G_{m,n}$ represents a ratio of temperature dependent material properties and contributes to the non-linearity of the PDE.

In order to decrease computational time and complexity when solving Equation 81 we note that by using a small time step for each iteration (0.0005 seconds due to the data sampling rate) the changes in nodal temperature and material properties are small. This time step size is well within the stability criteria described in Section 4.3. We can simplify the non-linear portions and approximate the temperature dependent material properties in the PDE by using the known values of these parameters from the previous time step, denoted

$p-1$, which can be expressed as

$$N(\theta_{m,n}^{p-1}) = G_{m,n}^{p-1}\left[\Psi\left(\theta_{m+1,n}^{p-1}-\theta_{m-1,n}^{p-1}\right)^2+\Gamma\left(\theta_{m,n+1}^{p-1}-\theta_{m,n-1}^{p-1}\right)^2\right], \tag{82}$$

valid for $n \in$ [2, N-1] and $m \in$ [2, M-1]. The previously described boundary conditions dictate the behavior of $N(\theta_{m,n})$ for $n = 1$, $n = \mathrm{N}$, $m = 1$, and $m = \mathrm{M}$ where

$$N(\theta_{m,n}^{p-1}) = \begin{cases} 0 & m \in [1,\mathrm{M}], n = 1 \\ G_{m,n}^{p-1}\Gamma\left(\theta_{m,n+1}^{p-1}-\theta_{m,n-1}^{p-1}\right)^2 & m = 1, n \in [1,\mathrm{N}-1] \\ (1-s)G_{m,n}^{p-1}\Gamma\left(X_{1,N}^{p-1}\right)^2 & m = 1, n = \mathrm{N} \\ G_{m,n}^{p-1}\left[\Psi\left(\omega_{M,n}^{p-1}\right)^2+\Gamma\left(\theta_{M,n+1}^{p-1}-\theta_{M,n-1}^{p-1}\right)^2\right] & m = \mathrm{M}, n \neq \mathrm{N} \\ G_{m,n}^{p-1}\left[\Psi\left(\omega_{M,N}^{p-1}\right)^2+(1-s)\Gamma\left(X_{M,N}^{p-1}\right)^2\right] & m = \mathrm{M}, n = \mathrm{N} \end{cases}. \tag{83}$$

4.5 System of Equations

For each time step p we are solving the system of equations

$$\dot{\vec{\theta}}^{p} = \mathbf{A}\vec{\theta}^{p} + \mathbf{F}(\vec{\theta}^{p-1}) + \mathbf{N}(\vec{\theta}^{p-1}) \tag{84}$$

where $\mathbf{A}$ is the coefficient matrix on $\vec{\theta}^{p}$, and $\mathbf{F}$ and $\mathbf{N}$ are vectors that are functions of the previous solution $\vec{\theta}^{p-1}$. Equation 84 will be solved using a numerical ordinary differential equation (ODE) solver, thus the system of equations is constructed as a system of first-order ODEs.

The heat transfer coefficient matrix $\mathbf{A}$ is an MN x MN matrix composed of several smaller block matrices, and is of the form

$$\mathbf{A} = \begin{bmatrix} \mathbf{I} & \mathbf{0} & \mathbf{0} & \mathbf{0} & \mathbf{0} \\ \mathbf{Z} & \mathbf{R} & \mathbf{Z} & \mathbf{0} & \mathbf{0} \\ \mathbf{0} & \ddots & \ddots & \ddots & \mathbf{0} \\ \mathbf{0} & \mathbf{0} & \mathbf{Z} & \mathbf{R} & \mathbf{Z} \\ \mathbf{0} & \mathbf{0} & \mathbf{0} & 2\mathbf{Z} & \mathbf{C} \end{bmatrix}. \tag{85}$$

We define $\mathbf{I}_{\mathrm{MxM}}$ to be an M x M identity matrix to satisfy the boundary condition at the heat sink. Define $\mathbf{Z}$ as an M x M matrix representing the dependence on the nodes in ξ, with $\mathbf{Z} = \sigma\mathbf{I}_{\mathrm{MxM}}$. Define $\mathbf{R}_{\mathrm{n}}$ as an M x M matrix representing the dependence on the nodes in ρ, where

$$\mathbf{R}_{\mathrm{n}} = \begin{bmatrix} -\gamma & \lambda & 0 & 0 & 0 \\ \eta_{2,n} & \ddots & \psi_{2,n} & 0 & 0 \\ 0 & \ddots & \ddots & \ddots & 0 \\ 0 & 0 & \eta_{M-1,n} & -\gamma & \psi_{M-1,n} \\ 0 & 0 & 0 & \psi_{M,n}+\eta_{M,n} & \psi_{M,n}\omega_{M,n}-\gamma \end{bmatrix}. \tag{86}$$

For the pin/disc contact boundary we define s=0 to denote not in contact and s=1 as the pin in contact with the disc, resulting in $\mathbf{C}$ as an M x M matrix for the contact region

$$\mathbf{C} = \begin{bmatrix} [(1-s)(\sigma X_{1,N})-\gamma] & \lambda & 0 & 0 & 0 \\ \eta_{2,N} & \ddots & \psi_{2,N} & 0 & 0 \\ 0 & \ddots & \ddots & \ddots & 0 \\ 0 & 0 & \eta_{M-1,N} & [(1-s)(\sigma X_{M-1,N})-\gamma] & \psi_{M-1,N} \\ 0 & 0 & 0 & \psi_{M,N}+\eta_{M,N} & [(1-s)(\sigma X_{M,N})+\psi\omega_{M,N}-\gamma] \end{bmatrix}. \tag{87}$$

$\mathbf{F}$ is an MN x 1 vector representing the forcing condition produced by the heat flux at the boundary when in contact. $\mathbf{F}$ is given by

$$\mathbf{F} = \begin{bmatrix} 0 \\ \vdots \\ 0 \\ s\sigma\Phi_{1,N} \\ \vdots \\ s\sigma\Phi_{M,N} \end{bmatrix}. \tag{88}$$

Recall when the pin is in contact with the disc s=1, however when not in contact s=0 and $\mathbf{F} \equiv 0$. $\mathbf{N}$ is an MN x 1 vector capturing the non-linearities expressed in Equations 82 and 83, defined by

$$\mathbf{N} = \begin{bmatrix} 0 \\ \vdots \\ 0 \\ \hline N(\theta_{1,2}) \\ N(\theta_{2,2}) \\ \vdots \\ N(\theta_{M,2}) \\ \hline \vdots \\ \hline N(\theta_{1,n}) \\ N(\theta_{2,n}) \\ \vdots \\ N(\theta_{M,n}) \\ \hline \vdots \\ \hline N(\theta_{1,N}) \\ N(\theta_{2,N}) \\ \vdots \\ N(\theta_{M,N}) \end{bmatrix}. \tag{89}$$

The first M entries of the vector are zero as these values are for the nodes located at the top boundary at the specimen/clamp interface.

4.6 Material Removal

One main aim of this research is to define the correlation between the temperature distribution of the pin and subsequent removal of material through wear processes. As material was removed in the experiment (as indicated by the displacement data), the locations of the thermocouples move closer to the contact interface. Within the confines of the numerical model, material removal equates to a moving boundary condition as the nodes associated with the thermocouple locations will be shifted closer to the heat source. The model includes two options for implementing the moving boundary. The first (Method 1) is empirical and is based directly on experimental displacement data. Consequently, it produces a predicted temperature distribution but no estimation of material loss. The second (Method 2) is constructed on the hypothesis that there is a temperature (U_{crit}) below the material's melting point (1685 K) that can be used to initiate the removal process. This is in contrast to the melt temperature criteria that was used in previous one-dimensional models and is a simplifying assumption of the thermal, mechanical, and chemical properties that characterize wear. This simplification facilitates use of the model generated thermal distribution as the primary input to predict material removal. The value of U_{crit} will be determined by examining the temperature distributions produced by Method 1 and is further discussed in Section 5.3.2. Thus, Method 2 produces results for temperature distributions and material removal that are both predictive in nature.

4.6.1 Method 1

To execute the material removal process, Method 1 directly utilizes the recorded displacement data collected from the experiment and creates a moving boundary by removing

material (nodes in the discrete case) within the model to mirror the recorded movement of the test specimen. This will occur in discrete increments of $\triangle\xi$ within the model. Thus, once the recorded travel reaches a multiple of $\triangle\xi$ the bottom "row" of nodes in the solution vector is removed and all preceding rows are shifted down to simulate the moving heat flux boundary condition. The values along the top are kept at $\theta_{m,1} = 0$ to maintain the boundary condition where the pin meets the clamp. For the constant contact case let $d_0 = 0$ represent the initial displacement value at first contact between the pin and disc and d_f represent the final displacement value when the pin is disengaged from the disc. Then the number of time steps where removal will occur is discretized and will be annotated as

$$j = \left\lfloor \frac{d_f}{a\triangle\xi} \right\rfloor \tag{90}$$

where the notation $\lfloor\ \rfloor$ represents the largest integer value that is less than or equal to the enclosed value. Then t_i, $i \in [1, j]$ designates the time steps of the experimental test run in which $i\triangle\xi$ distance has been traveled by the specimen (meaning $i\triangle\xi$ of material has been removed) and t_i is a time step where removal criteria was met. The surface temperature values at this time step are averaged and recorded for future use in approximating a critical surface temperature value upon which material was removed, which will be used when executing Method 2 of implementation for material removal. The process of removing material and shifting the solution vector according to the displacement data (Method 1) occurs independent of the temperature profile and places no restrictions on the surface temperature calculations, as opposed to the second method in which material is removed based on the temperatures at the pin's surface.

4.6.2 Method 2

In order to implement material removal dependent on surface temperatures, the algorithm considers the model's thermal solution at each time step and averages the nodal tem-

peratures along the contact surface. This average value is compared against the critical temperature U_{crit}. If this value is exceeded, the bottom row of nodes is removed and replaced with the temperature values from the row above it. As in Method 1, all temperature values for each row above are shifted down one grid row which, in effect, creates the moving boundary condition. Method 2 assumes the temperature in the row of nodes just above the surface has not reached U_{crit}. This is due to the small time step taken at each iteration [17]. The shifted vector becomes the new solution vector for that time step and the iteration process continues at the next time step.

For both methods of implementing the moving boundary, material loss at a given time step t_i equates to the pin losing a volume of $\pi r^2 \triangle z$ m^3.

4.7 MATLAB Algorithm

The model's iteration process begins by incorporating data recorded from the test runs as input. The model determines the contact surface boundary condition (convection or conduction), calculates the coefficient of friction (as applicable) and material properties based on temperature distribution calculations, builds the system of equations for that time step, and solves the ordinary differential equation using MATLAB's ODE45 solver.

ODE45 is an explicit Runge-Kutta formula based on an algorithm of Dormand and Prince [18]. They sought to develop a set of formulae that would have a "'small' principle truncation term in the fifth order and have an extended region of absolute stability" [18]. This solver provides fourth and fifth order formulas and is capable of adjusting the step size in order to maintain accuracy in the solution. In this case the solver will determine an internal step size to use based on the specified domain of integration $\left[t_0, t_f\right]$. When using a step size of 0.0005 seconds for the algorithm based on the recorded data, ODE45 makes 41 internal time steps to integrate the differential equation. This process is repeated for the duration of the test run to produce predictions for thermocouple temperature evolution over

time and takes into account the data recorded from the experimental test in consideration.

The solution process is outlined in Figure 25. For a given time step p, the algorithm considers the force data recorded at that time step given by $F(t_p)$ and uses this value to determine if the specimen is in a "bouncing" condition or if there is a contact condition between the pin and disc. This determines the appropriate boundary condition that will be enforced at $\xi = 0$. In the case of a no contact condition, the convection boundary conditions along the flat surface of the pin are computed using Equation 47. If the specimen is in contact with the spinning disc, then Equation 45 is used to determine the conduction boundary condition. Recall that the forcing vector (**F**) when the pin is in contact with the disc is driven by the conductive heat flux into the specimen, with $q''(t)$ given by Equation 11. The force $F(t_p)$ is known, and velocity v and contact area A are considered constant for the duration of the test run. The partition fraction $\beta(t)$ and coefficient of friction $\mu(t)$ are computed, determination of which will be further discussed in Section 5.3.

The resulting values are used to build the heat transfer matrix **A**, and forcing vectors **F** and **N** that are described in Section 4.5. Using MATLAB's ODE45 solver, the system of equations is then solved. Depending on the specified process of material removal the algorithm will employ the appropriate method of moving boundary implementation described in Section 4.6, either 1) by application of the recorded displacement data (Method 1) or 2) based on comparison of the surface temperature distribution to U_{crit} (Method 2). The algorithm then determines the final solution vector for that time step and proceeds to the next time step, completing this iterative process until the specimen's contact with the disc is disengaged for the final time.

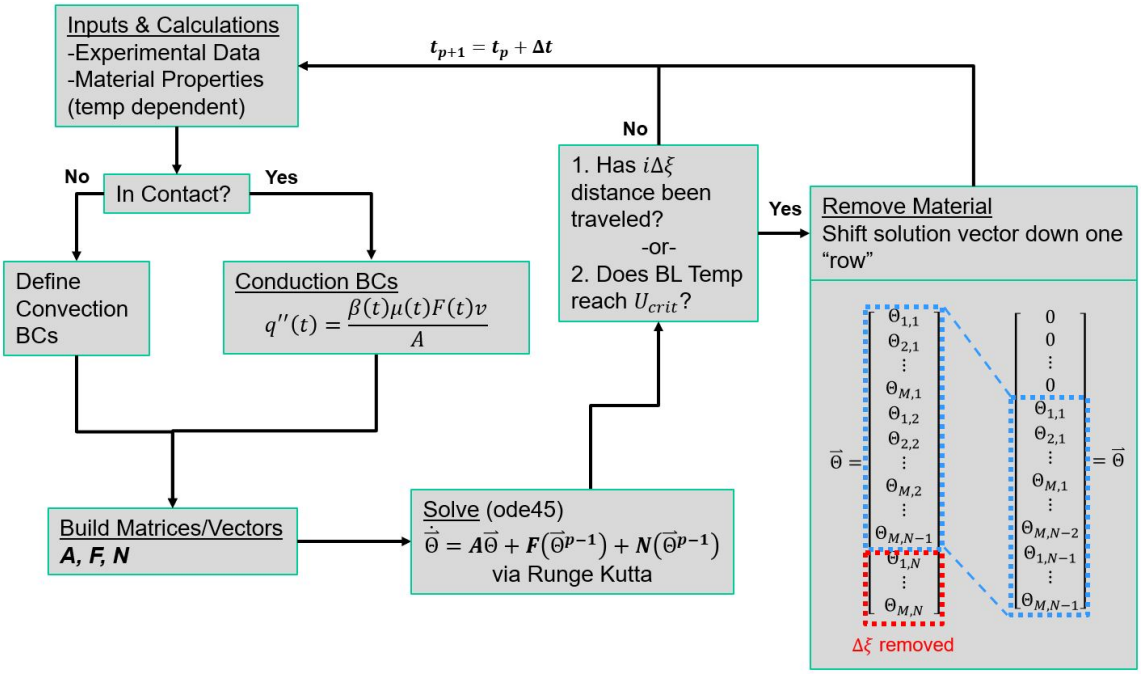

Figure 25. Solution Algorithm

V. Observations and Analysis

5.1 Chapter Overview

This chapter details the results generated by the heat transfer model and considers several applications of previous research for the coefficient of friction and partition function values. It explores the effects of temperature dependent material properties specific to the pin-on-disc experiments that were conducted. This chapter also discusses the relationship between the pin's temperature distribution and corresponding wear observed in the experimental tests and calculated by the model using the critical temperature removal concept. Although both the constant contact and bouncing conditions were modeled, this analysis focuses primarily on the constant contact condition.

5.2 Observations

5.2.1 Thermal Diffusivity

Figure 22 illustrates the thermal diffusivity of the pin as a function of temperature. In DeLeon's [17] work, the material properties of specific heat and thermal conductivity were evaluated at each time step to more accurately characterize the heat diffusion process. This methodology is also incorporated in the current model. Using input from the experimental test conducted at 96 m/s, and the model generated temperature distribution at the contact surface of the pin, Figure 26 displays the thermal diffusivity of material at the surface as a function of time. This value is generated by taking the model produced temperature distribution at the surface for each time step and calculating the respective thermal diffusivity value, which is approximated from the curve in Figure 22. The horizontal line also displayed in Figure 26 is the constant value of the material's thermal diffusivity ($\alpha = 4.4883e-6$ m^2/s) that was used in slipper wear and temperature distribution research

performed at AFIT prior to DeLeon's [17] work. The plot of thermal diffusivity calculations at pin's surface for the experimental test at 48 m/s exhibits similar behavior.

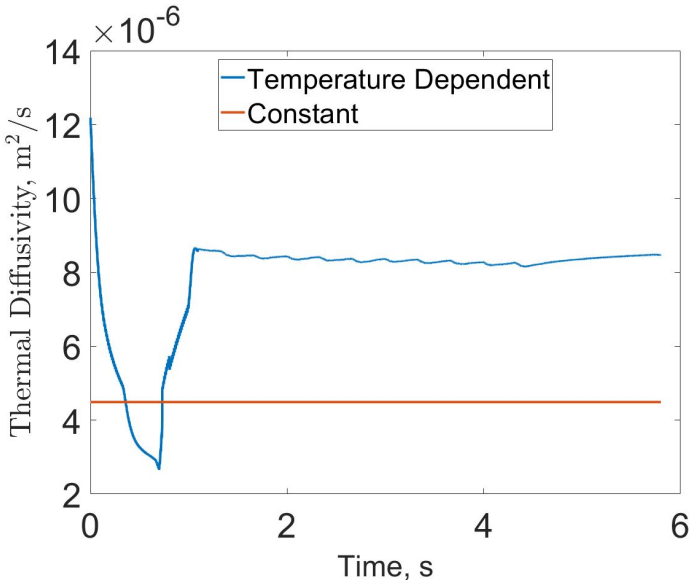

Figure 26. Thermal Diffusivity Values, 96 m/s

As the temperatures rapidly increase at the surface, thermal diffusivity varies during the first second of the test. After that, the thermal diffusivity reaches a relatively constant value as the surface temperature approaches a region corresponding to a relatively constant diffusivity (see Figure 22). The effects of temperature dependent material properties on the transient thermal distribution of the pin will be further discussed in Section 5.3.3.

5.2.2 Wear

Considering the case of constant contact at constant velocities of 48 and 96 m/s, the predicted and observed wear rates are plotted using Lim and Ashby's normalized parameters (see Section 2.3). Priority was given to the use of the calculated normalized velocity when plotting, as opposed to actual velocity (m/s).

Figure 27 is the wear map developed by Lim and Ashby [39] in which the observed and expected normalized wear rates, based on the experimental velocity and force profiles, are plotted. The range of normalized velocities is due to the considered effect of temperature

dependent thermal diffusivity of the material, since the normalized velocity (Equation 13) is a function of α. The range along the normalized force axis is a result of the fluctuations in force input due to the control mechanism. The red region indicates predicted normalized wear rates on the order of 10^{-8} to 10^{-9} for both velocities. The observed normalized wear rates indicated in green were computed according to Equation 12, using the recorded displacement data as input to determine volume lost at a given time step and the velocity to determine the distance traversed. Applying this methodology, the experimental data yielded normalized wear rates on the order of 10^{-4} to 10^{-6}.

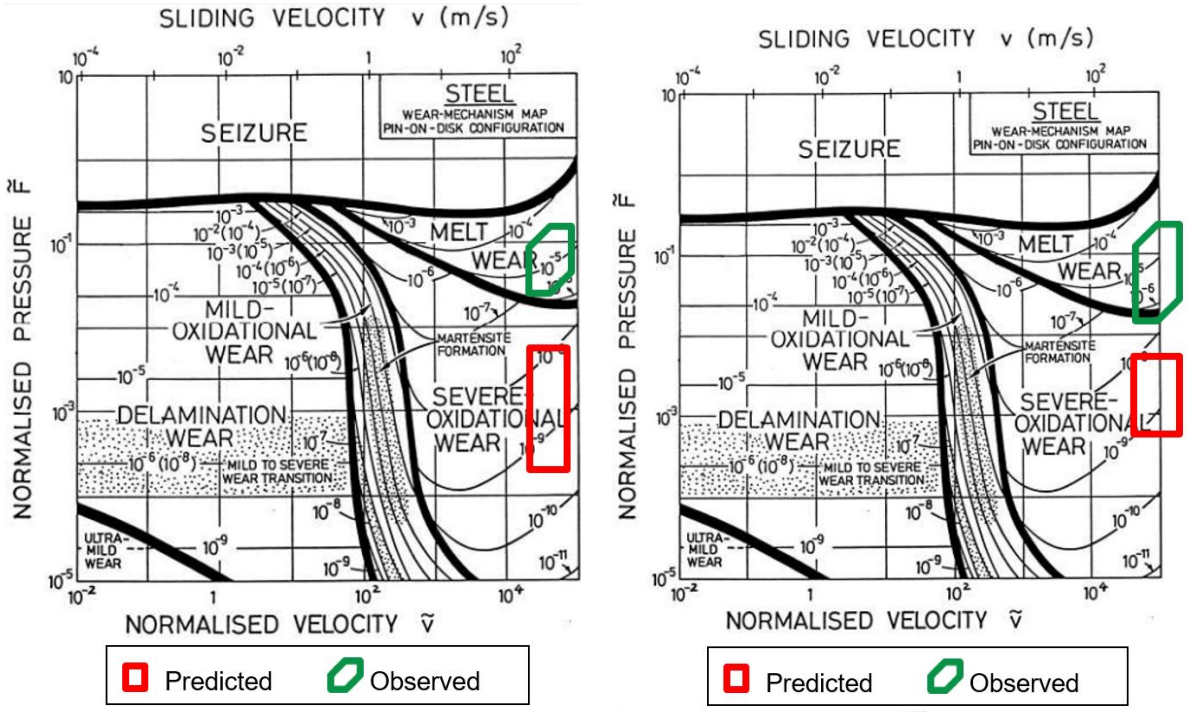

(a) Constant Contact, 48 m/s

(b) Constant Contact, 96 m/s

Figure 27. Pin-on-Disc Experimental Wear Maps

The observed and predicted regions of normalized wear rates differ by several orders of magnitude and fall into different dominant wear regimes. In particular, the displacement data seems to suggest that melt wear occurred however, experimental observations and model results discussed in Section 5.3.5 indicate that melt was not likely to have been present. The specimen's end shape, displayed in Figure 28, shows that plasticity was a

contributor to the deformation process, which is not considered in the development in this model and will be further discussed in Section 6.1.

Figure 28. Recovered Test Specimen, 96 m/s

Of note, the wear map produced by Lim and Ashby was developed to be a single diagram representing the approximate wear behavior of a wide range of steels. It is likely that in regards to the pin-on-disc experiments performed in this research, differing material properties and the effects of temperature on the material are contributing factors to the discrepancies shown in Figure 27. This is especially true when considering the specific heat of Vascomax® 300 (Figure 18a) and its behavior as temperatures approach 800 K when the material undergoes a solid-solid phase change affecting the crystalline structure.

Shown in Figure 29 are collected force and displacement data profiles for the tests conducted at 48 and 96 m/s, respectively. The force input is annotated on the right vertical axis and data displayed in orange, and the recorded displacement (position) of the specimen is annotated on the left vertical axis and data displayed in blue. The time domain is truncated in order to closely observe the behavior and correlation between force input and displacement. Again, the periodic nature of the force input given in Figure 29 was due to fluctuations produced by the force control mechanism and operator input in order to maintain contact between the pin and the disc. In general, there are two distinctive slopes for each displacement profile; one of which can be characterized by increased displacement

rates and the other corresponding to periods of lesser displacement rates. For both velocity profiles at 48 and 96 m/s, we observe that higher force input translates to higher rates of change in the displacement data. These rates are directly associated to wear rates. As we would expect, increased force leads to a higher heat flux input at the contact boundary and thus, increased amounts of displacement which is attributed to material wear.

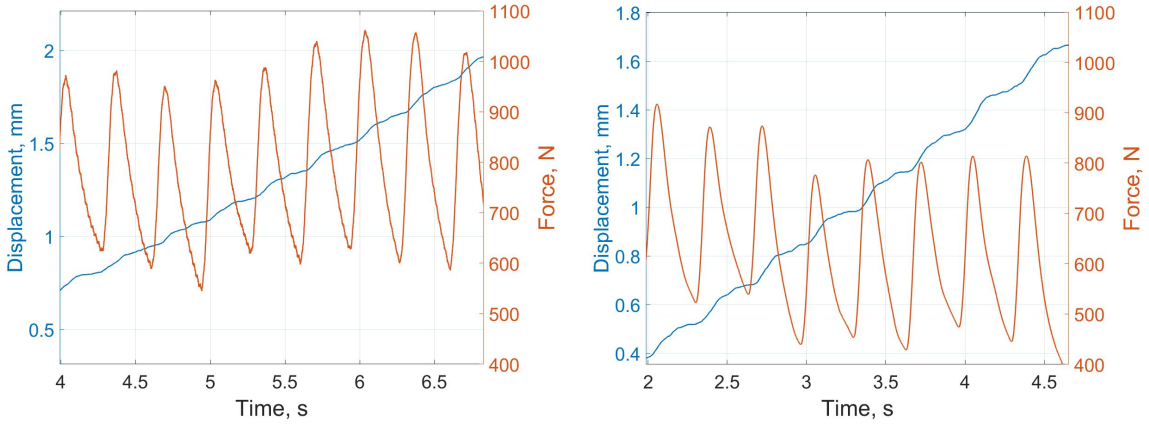

(a) Constant Contact, 48 m/s (b) Constant Contact, 96 m/s

Figure 29. Actual Force vs. Displacement

5.2.3 Approximating the Heat Partition Coefficient

Two terms contributing to the calculated value of heat flux, q'' given by Equation 11, are the partition coefficient and the coefficient of friction. Research concerning the heat partitioning coefficient was outlined in Section 2.8. While researchers did not in general reach the speeds or forces observed in this experiment, their applications are consistent and show that the majority of the heat generated will flow into the spinning disc.

Through estimations of the convective effects, applications of research performed by Laraqi et al. [37] yield the ranges of β for the conditions considered in this experiment displayed in Figures 30 and 31. Recall, the Biot number (Bi) discussed in Section 2.7 is a measure of the relative contributions of convection and conduction in determining the temperature distribution of a material. As the disc is spinning and the pin is stationary,

the disc will experience a more significant heat loss due to convection than the pin, and will have a larger Biot number. Although this research did not model the temperature distribution of the disc, Figure 30 shows the estimated ranges for Bi_d and Bi_p based on calculations using Equations 19 through 22, with the fraction of total heat generated flowing into the disc annotated on the vertical axis. According to the estimations of Biot number alone, we deduce that less than 12 percent of the total heat generated will flow into the pin.

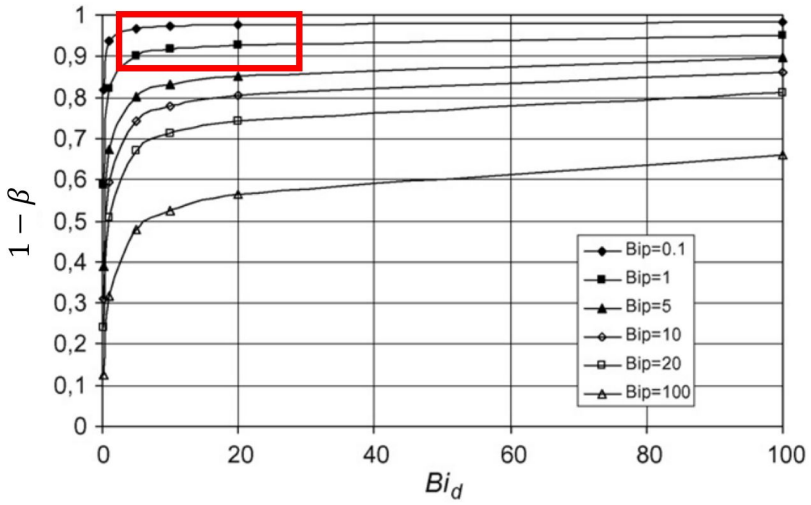

Figure 30. Heat Partitioning Approximations for Disc Velocity Ranges 15-240 m/s as a function of Bi_d and Bi_p [37]

Given the velocities in question for the experimental parameters, the *Pe* values experienced ($Pe \geq 5000$) are far greater than those charted by Laraqi et al. however, we assume that as the values for $1-\beta$ remain relatively constant for high *Pe*, this will remain the case for the current ranges in consideration. When applying the estimations of the disc's Peclet number and Biot number in Figure 31, we observe that less than 3 percent of the total heat generated is predicted to flow into the pin. However, this division of heat is based on the heat transfer between two materials of similar material properties and $Bi_p = 0.1$. As discussed in Section 2.8, as the thermal diffusivity of the pin decreases, which for Vascomax® 300 occurs over temperatures less than 800 K, a lower fraction of the total heat generated will flow into the pin.

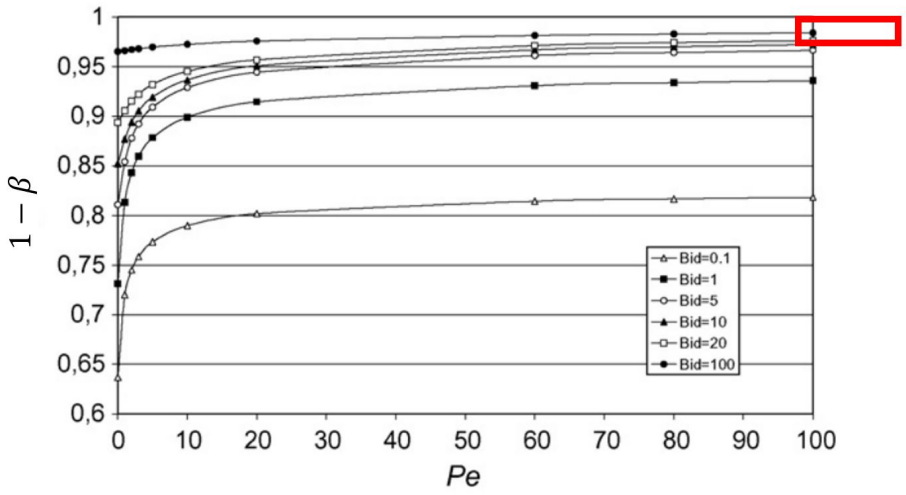

Figure 31. Heat Partitioning Approximations for Disc Velocity Ranges 15-240 m/s as a Function of Pe and Bi_d[37]

The behavior of the heat partition function with regard to thermal diffusivity is illustrated in Figure 32 through the formulas developed by Blok [10], Jaeger [29], Lim and Ashby [39], and Berry [8] given by Equations 24, 25, 26, and 27, respectively. Recall, these equations are functions of material properties and should be expected to change as the temperature changes with respect to time. Figure 32 displays the values of the respective approximations using the results of the numerical model to calculate the thermal diffusivity at the pin's surface, considering the test conducted at 96 m/s. As we would expect, the behavior and order of magnitude correspond well when comparing the approximations given by the different formulae. The initial decrease in values for the partition coefficient can be attributed to the temperature dependent material properties, as the value for thermal diffusivity is decreasing between the ranges of initial ambient temperature and approximately 800 K. As the model's surface temperature calculations approach 800 K at approximately 0.9 seconds, the thermal diffusivity begins to increase which is subsequently reflected in the increasing value for the partitioning coefficient. As the temperature at the surface approaches a steady state (and subsequently the values of thermal diffusivity and thermal conductivity) the behavior of β reaches a relatively constant value. These parti-

tioning estimates are similarly produced for the test conducted at 48 m/s and are slightly higher due to the decrease in velocity.

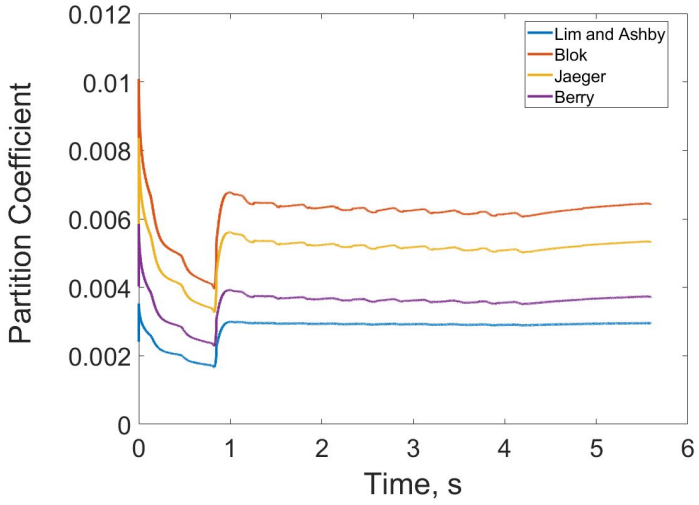

Figure 32. Heat Partitioning Approximations, 96 m/s

It was discovered through implementation of Equations 24 through 27 in the numerical model that the corresponding heat flux into the sample was insufficient and resulted in temperature predictions several factors below those recorded. A partition fraction below 0.01 does not match observed phenomenon and is unlikely under the assumptions of this model. Considering the implications of research by Laraqi et al. [37], the partition fraction was tuned within the model to produce temperature distributions at the thermocouple locations that best recreated the experimental temperature observations at the thermocouples. Through this procedure it was possible to estimate constant heat partitioning values depending on the velocities in question, which will be further specified in Section 5.3.

5.2.4 Approximating the Coefficient of Friction

The coefficient of friction was discussed in Section 2.4 and the two equations (Equations 15 and 16) are evaluated in terms of the experimental parameters. The approximation developed by Hale from the Montgomery data (Equation 16) is a function of the raw data

of pressure and velocity, whereas the expression developed by Lim and Ashby (Equation 15) takes into account the thermal diffusivity (through use of the normalized velocity term), which is a function of temperature and thus depends on input from the model. In Figures 33 and 34, the experimental data or thermal diffusivity calculations from the test runs conducted at 48 and 96 m/s are applied to the two equations, respectively, with the function's input annotated on the left vertical axis and displayed in blue, and the COF output annotated on the right vertical axis and displayed in orange. Figures 33a and 34a consider the Montgomery equation and the oscillations in COF are a result of the oscillatory changes in force input, as velocity is held constant for the test runs. Figures 33b and 34b are produced using Lim and Ashby's equation $(\mu = 0.78 - 0.13\log(vr_p/\alpha))$, which reflects the temperature dependent behavior of thermal diffusivity as the pin's surface temperature increases through the duration of the test runs. The sharp changes that occur at approximately 1.4 and 0.8 seconds, respectively, are a result of the temperature dependent material properties and portray the rapid changes in thermal diffusivity values (Figure 22) as the material transitions from martensite to austenite at the surface. This is reflected in the surface temperature calculations shown in Figure 36.

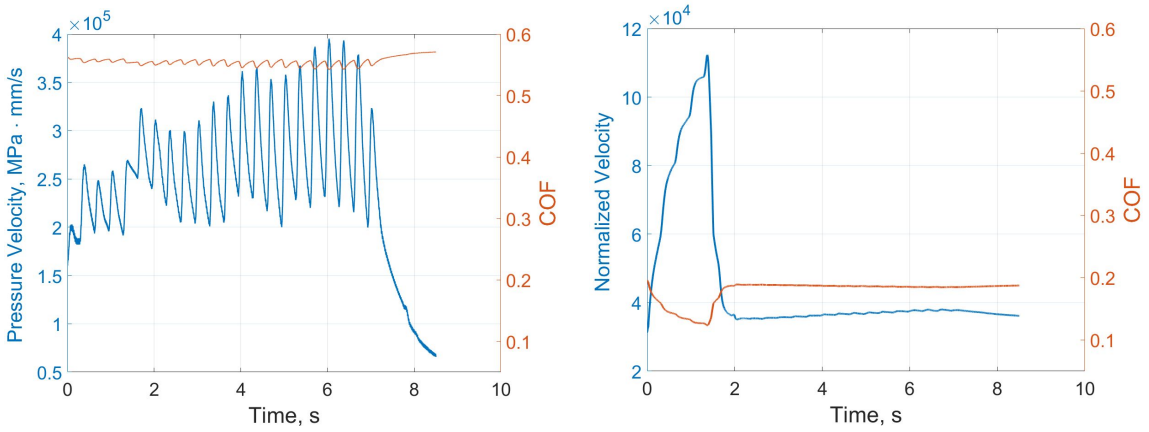

(a) Montgomery (b) Lim and Ashby

Figure 33. COF Approximations (Constant Contact, 48 m/s)

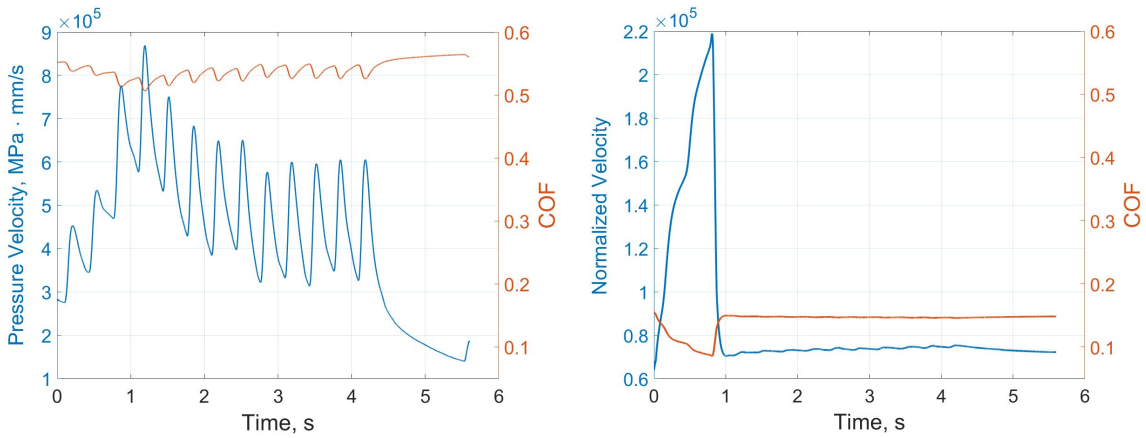

(a) Montgomery (b) Lim and Ashby

Figure 34. COF Approximations (Constant Contact, 96 m/s)

For the Montgomery curve, the approximation by Hale produces coefficient of friction values that are 3 to 4 times larger on average than those of Lim and Ashby. Given the influence of the heat flux boundary condition (Equation 11) on the solution, this magnification will significantly scale the calculated thermal distribution. For a fixed partition coefficient β, the model produced temperature distributions are magnified by a similar factor (between 3 and 4) when varying the only the input for COF between the Montgomery and Lim and Ashby curves. Table 5 is a summary of Figures 33 and 34, giving COF ranges for the two equations and velocity profiles, and the average COF value over time for the duration of the experimental test runs.

Table 5. COF Ranges

Equation	Velocity	Minimum Value	Maximum Value	Average Value
Lim & Ashby	48 m/s	0.1223	0.2082	0.1778
Montgomery	48 m/s	0.5344	0.5756	0.5553
Lim & Ashby	96 m/s	0.0834	0.1690	0.1410
Montgomery	96 m/s	0.4993	0.5735	0.5406

5.3 Results and Analysis

Based on the recorded force and velocity data from the test runs, the model results under constant contact conditions are analyzed. For each run, the partition coefficient β was fixed as a constant. Considered first is the implementation of the moving boundary (material removal) by shifting the source location as recorded by the displacement data (Method 1). In this instance, the amount of wear (material removed) results in the solution vector shifting to simulate the moving boundary as the sample moves towards the disc in increments of $\triangle\xi$. One purpose of this approach is to determine if there may be an equivalent temperature or stored energy state that can be used in the thermal model to predict material removal based on temperatures experienced at or near the pin's surface.

5.3.1 Implementing a Moving Boundary Using Recorded Data (Method 1)

To accurately determine the temperature distribution of the pin, the heat flux (Equation 11) must be computed. Both the Lim and Ashby equation (Equation 15) and the Montgomery approximation (Equation 16) for coefficient of friction calculations are considered as inputs to compute the heat flux, with the respective heat partitioning values taking on similar scale factors as discussed in Section 5.2.4.

5.3.1.1 Lim and Ashby COF

When taking the displacement data into consideration and implementing the moving boundary as a function of this data, temperature profiles produced by the model are shown in Figure 35, with $\beta = 0.126$ for $v = 48$ m/s and $\beta = 0.114$ for $v = 96$ m/s, and using the Lim and Ashby equation for COF calculations. The decrease in the partition coefficient β with the increase in velocity is logical, given the implications of Section 5.2.3. The solid lines in Figure 35 reflect the model produced temperature profiles at the thermocouple locations as a function of time, while the dashed lines represent the actual thermocouple

temperatures as recorded by the data. The colors are specific to the respective temperatures at the thermocouple locations with "T1" representing the thermocouple closest to the contact interface, "T2" designating the second thermocouple located ⅛-inches from T1, and "T3" the location of thermocouple farthest from the contact interface and closest to the clamp. Although the model produced temperature profiles differ from the data, the behavior is similar in nature and the maximum temperature achieved is approximately the same (acknowledging that this is above the thermocouple's maximum rated temperature). This will be further discussed in Section 5.3.6.

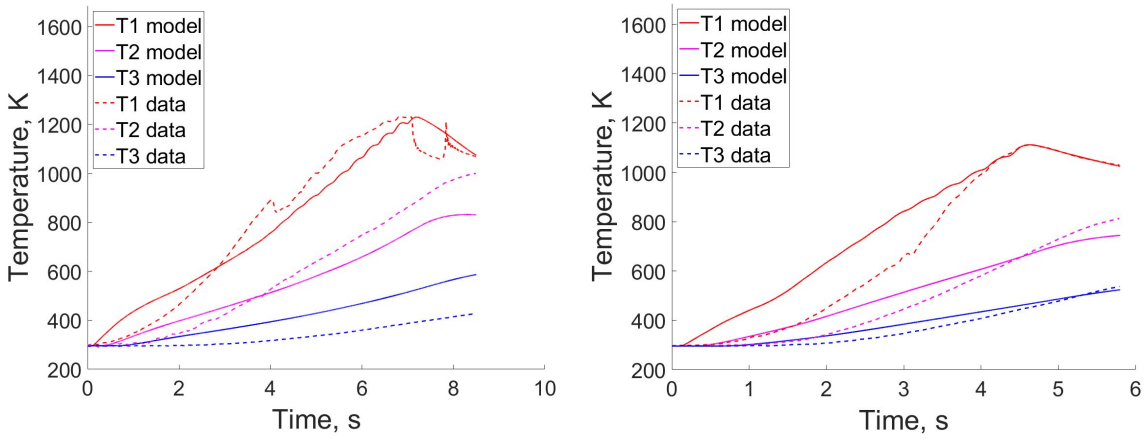

(a) Constant Contact, 48 m/s

(b) Constant Contact, 96 m/s

Figure 35. Model Thermocouple Temperatures based on Displacement Data Using Lim and Ashby COF

The time steps where removal criteria were met are overlaid on the model produced surface temperature calculations and shown in Figure 36. Each '+' symbol represents the pin's surface temperature as calculated by the model, at a time step (t_i discussed in Section 4.6) in which the specimen's displacement has reached $i\triangle\xi$ distance traveled.

Of note, there is no single temperature value at which material removal occurs, although removal occurs more rapidly as the surface temperature increases. The average temperature at which material removal occurred is represented by the green dashed line, with $\bar{U}_{removal} = 1224$ K for $v = 48$ m/s and $\bar{U}_{removal} = 1295$ K for $v = 96$ m/s. For both test

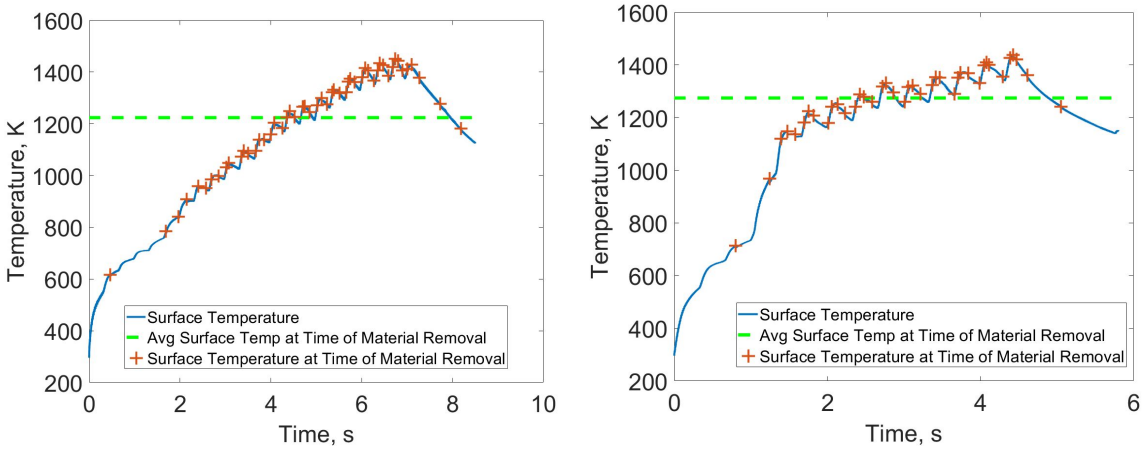

(a) Constant Contact, 48 m/s

(b) Constant Contact, 96 m/s

Figure 36. Surface Temperatures upon Material Removal Using Lim and Ashby COF

runs, the maximum calculated surface temperature exceeds 1400 K, but does not approach the material's melt temperature of 1685 K.

We can also utilize the concept of stored thermal energy within a system, described in Section 1.6.2 and given by Equation 6, to determine the thermal energy within the removed layer of material. Recall that the stored thermal energy of a system is directly related to the specific heat of the material (Figure 18a) and temperature of the region in consideration. When removing material at time t_i, the amount of material lost has a volume of $\pi r^2 \triangle z$ m^3 and has thermal energy in units of joules (J). For the test runs conducted at 48 and 96 m/s, evaluating the stored thermal energy within the pin's surface layer of thickness $\triangle z$ yields the results in Figure 37 using Lim and Ashby's COF equation (Equation 15) to determine the heat flux.

Each '+' symbol represents the stored energy at the pin's surface with thickness $\triangle z$ as calculated by the model, at a time step t_i in which material has been removed by the algorithm. The average stored energy within a removed layer is represented by the green dashed line, with $\bar{E}_{removal} = 4447$ J for $v = 48$ m/s and $\bar{E}_{removal} = 4671$ J for $v = 96$ m/s. Again, there is no single value for stored thermal energy at which material removal occurs and despite the early behavior of the curves where the specific heat is rapidly increasing

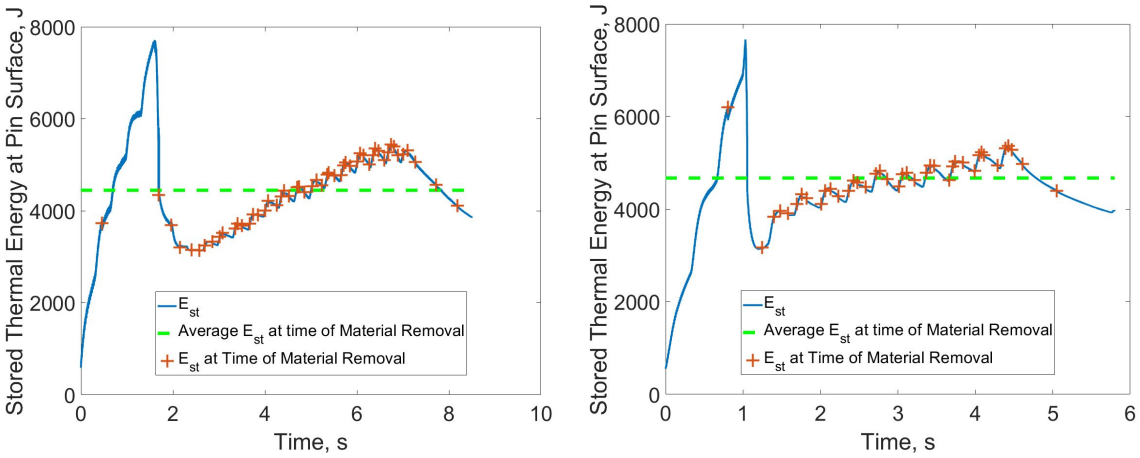

(a) Constant Contact, 48 m/s (b) Constant Contact, 96 m/s

Figure 37. Stored Energy upon Material Removal Using Lim and Ashby COF

due to the temperature rise and stored thermal energy achieves maximum values, material removal occurs more frequently following the sharp decrease in specific heat. This rapid change is associated with surface temperature values approaching 800 K where the material is presumed to have changed from a martensite to austenite crystalline structure as discussed in Section 2.6.

5.3.1.2 Montgomery COF

As previously noted, the COF values when using the Montgomery data equation are significantly higher than those produced by the Lim and Ashby equation. Therefore, lower values of β are required to produce similar thermal profiles. As before, when accounting for displacement data and implementing the moving boundary as a function of the data (Method 1), thermocouple temperature profiles for the two tests in consideration are shown in Figure 38 and compared to the recorded data, using $\beta = 0.0419$ for $v = 48$ m/s and $\beta = 0.0304$ for $v = 96$ m/s.

Based on the model results, the surface temperatures and corresponding time steps at which material was removed according to the displacement data are shown in Figure 39. The trends in thermocouple and surface temperature calculations when using the Mont-

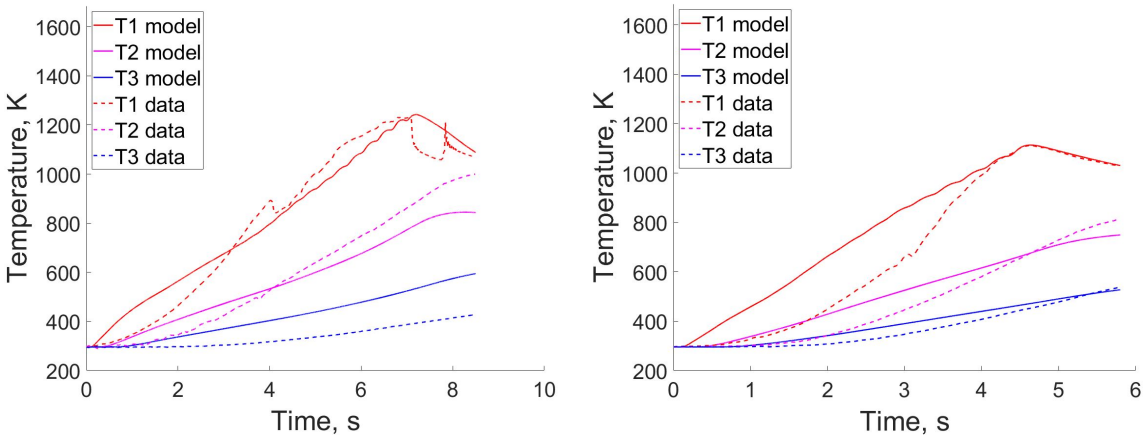

(a) Constant Contact, 48 m/s (b) Constant Contact, 96 m/s

Figure 38. Model Thermocouple Temperatures based on Displacement Data Using Montgomery COF

gomery COF remain similar to those determined through the use the Lim and Ashby COF equation and will be further analyzed in Section 5.3.6. The average values for surface temperatures at which material was removed are $\bar{U}_{removal} = 1241$ K for $v = 48$ m/s and $\bar{U}_{removal} = 1287$ K for $v = 96$ m/s.

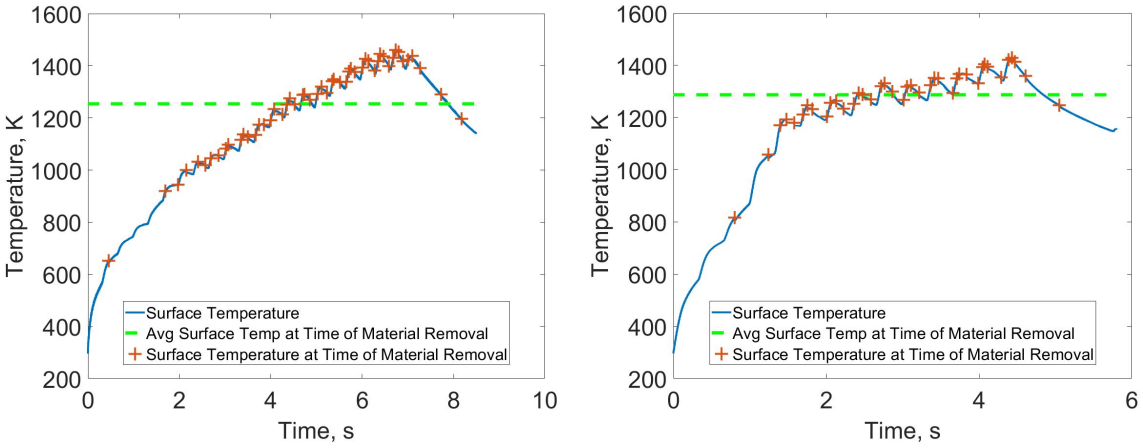

(a) Constant Contact, 48 m/s (b) Constant Contact, 96 m/s

Figure 39. Surface Temperatures upon Material Removal Using Montgomery COF

Applying the stored thermal energy concept in Figure 40 we again discover no distinct value for stored thermal energy that directly correlates to material removal. However, the observation remains that as the thermal energy begins to rise following the solid-solid phase transformation of the material at approximately 800 K, it is increasingly likely that material

loss will occur. Average values represented by the green dashed lines are $\bar{E}_{removal} = 4538$ J for $v = 48$ m/s and $\bar{E}_{removal} = 4659$ J for $v = 96$ m/s.

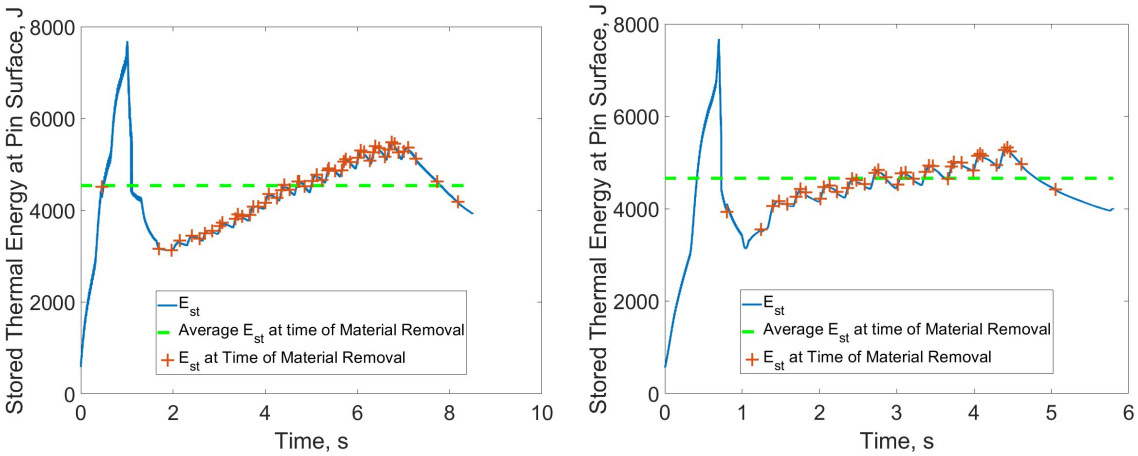

(a) Constant Contact, 48 m/s (b) Constant Contact, 96 m/s

Figure 40. Stored Energy upon Material Removal Using Montgomery COF

5.3.1.3 Comparison

As we would expect, the temperature profiles generated through the use of the different COF calculations are fairly similar, since the product of $\beta\mu(t)$ is essentially a scaling factor in regards to the boundary condition. The values of $\beta\mu(t)$ as a function of time are shown in Figure 41, using both the Montgomery COF and Lim and Ashby COF equations, and respective partitioning coefficients previously specified for the tests under constant contact conducted at 48 and 96 m/s. Since we are scaling Figures 33 and 34 by the respective β value depending on the COF choice, the behavior is similarly justified. As expected, the values for $\beta\mu(t)$ in Figure 41 under both the Montgomery and Lim and Ashby calculations differ only slightly in value once the thermal diffusivity of the material reaches equilibrium, resulting in the similar thermal profiles that are reflected in Figures 35 and 38.

The question then becomes which combination is more likely to have occurred? Based on the partitioning values from research outlined in Section 2.8 and their respective applications with regard to the experimental parameters summarized in Section 5.2.3, it is likely

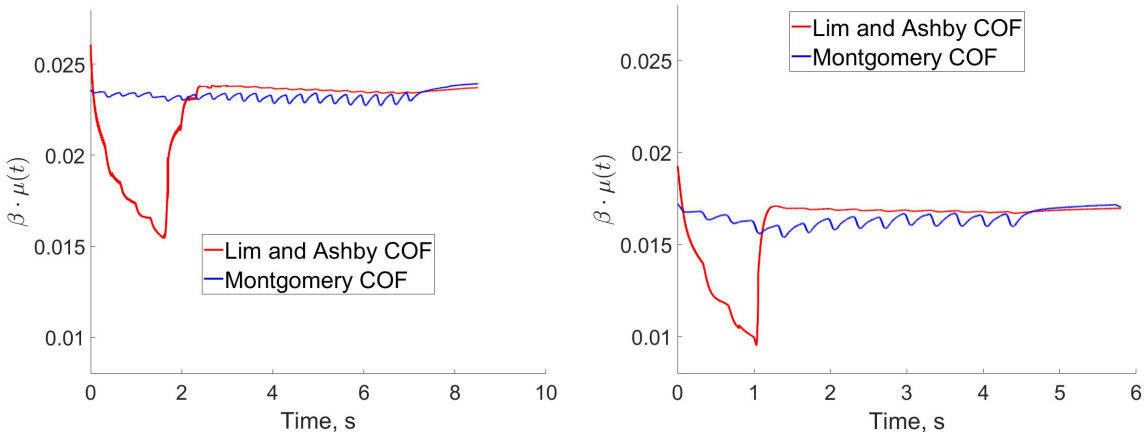

(a) Constant Contact, 48 m/s

(b) Constant Contact, 96 m/s

Figure 41. Comparison of the Product $\beta \cdot \mu(t)$ for Montgomery and Lim & Ashby COF Calculations

that only a small fraction of the heat generated enters the sample. The lower COF values achieved by Lim and Ashby's equation (Equation 15) required higher values of the heat partition coefficient ($\beta \approx$ 11-12%) to achieve the same thermal profile produced through the use of the Montgomery COF (Equation 16) scaled by $\beta \approx$ 3-4%. For this reason the Montgomery COF equation (Figures 33a and 34a) values and the corresponding values for the partitioning coefficient β will be used in subsequent analysis and when implementing the critical temperature removal criteria to predict material wear (Method 2).

It is important to note that Method 1 of implementation for the moving boundary using the recorded data to shift the source location, while remaining predictive in nature for the temperature distribution of the sample, is not predictive of material removal. While the surface temperatures and stored thermal energy within a removed layer that corresponds to displacement changes in increments of $\triangle\xi$ are not constant, as shown in Figures 39 and 40, an estimated U_{crit} may be inferred to support an alternate method of material removal calculation based on temperature. To implement a model that is predictive in nature for both temperature and material removal, we will utilize the concept of a critical temperature equivalent.

5.3.2 Implementing a Critical Temperature Concept

A simple approximation of a single value for the critical temperature can be made through analysis of the information reflected in Figures 39 and 40 and application of the concept of stored thermal energy within a removed layer of material. The amount of thermal energy within this layer, at time t_i, is given by Equation 5. Using the previously determined average stored thermal energy values ($\bar{E}_{removal}$) at times of material removal allows determination of the average temperature $\bar{U}_E$ associated with the thermal energy value, by solving the equation

$$\bar{E}_{removal} = \rho_s \hat{c}_p(\bar{U}_E)\bar{U}_E \tag{91}$$

for $\bar{U}_E$.

The model produced surface temperature values at removal time steps t_i, observed in Figure 39, are also examined in the determination of U_{crit}. Again, although no singular value is present, a simple approximation of U_{crit} can be made by considering the average values computed for $\bar{U}_{removal}$.

Following analysis of $\bar{U}_E$, $\bar{U}_{removal}$, the ranges of recorded thermocouple temperatures, and subsequent accuracy of the thermal models, a best approximation of $U_{crit} = 1276$ K was formulated. The importance of the critical temperature value is two-fold: 1) it will be used to implement the material removal process in the model and 2) it will force a restriction on the pin's temperature at the contact boundary. The result of the second implication is the imposition of a maximum temperature that can be achieved not only at the pin's surface but also for the entire thermal distribution of the pin.

Results for temperature distributions and material removal predictions utilizing the critical temperature removal criteria are shown in Figures 42 and 43 for the tests conducted at 48 and 96 m/s, respectively. In both cases the computed thermal profiles for the thermocouple temperatures in 42a and 43a indicate an initial increase above the observed temperature

values, and achieve higher maximum values than the model temperature profiles produced in Figure 38 when the boundary was instead shifted according to the displacement data (Method 1). This difference is attributed to the increased amount of material removal (and subsequent moving boundary condition) predicted by the model, shown in Figures 42b and 43b, as opposed to what the actual displacement data reflects. The model-predicted total wear for the test conducted at 48 m/s amounts to an overestimation of 44% of the recorded values and reaches the location of the first thermocouple, an occurrence that was not observed in experimental testing. The model corresponding to the test conducted at 96 m/s predicts a 46% increase in wear when comparing with the observed values, although this increase does not lead to predicted wear reaching the first thermocouple as the overall recorded displacement is to a lesser degree. Despite the over-prediction of total material wear for both velocities, there is a delay in the time step associated with initial removal since the surface temperatures produced by the model have not yet reached the removal threshold. The choice of $U_{crit} = 1276$ K is a conservative estimate when assessing overall wear but does not accurately characterize the initial removal process.

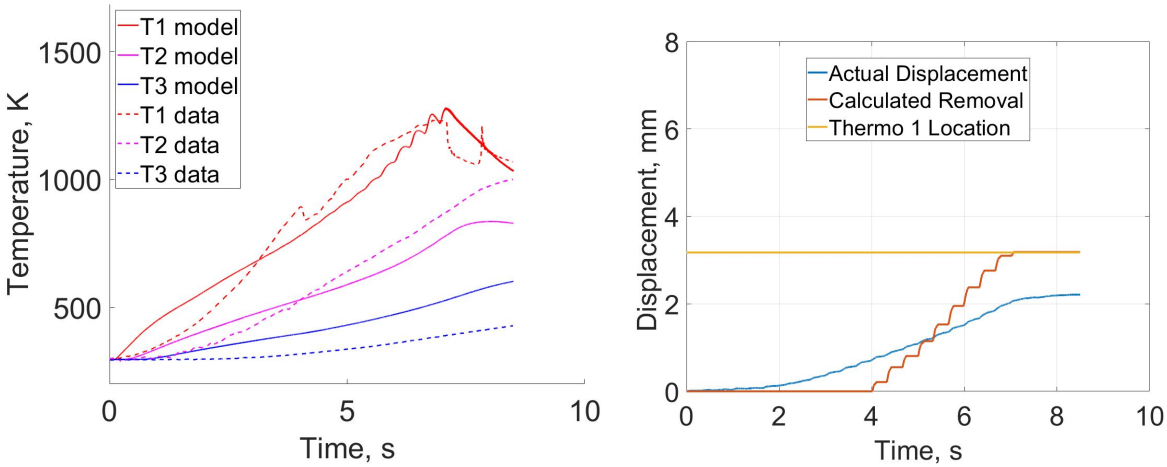

(a) Thermocouple Temperatures

(b) Material Removal

Figure 42. Critical Temperature Removal Criteria, 48 m/s

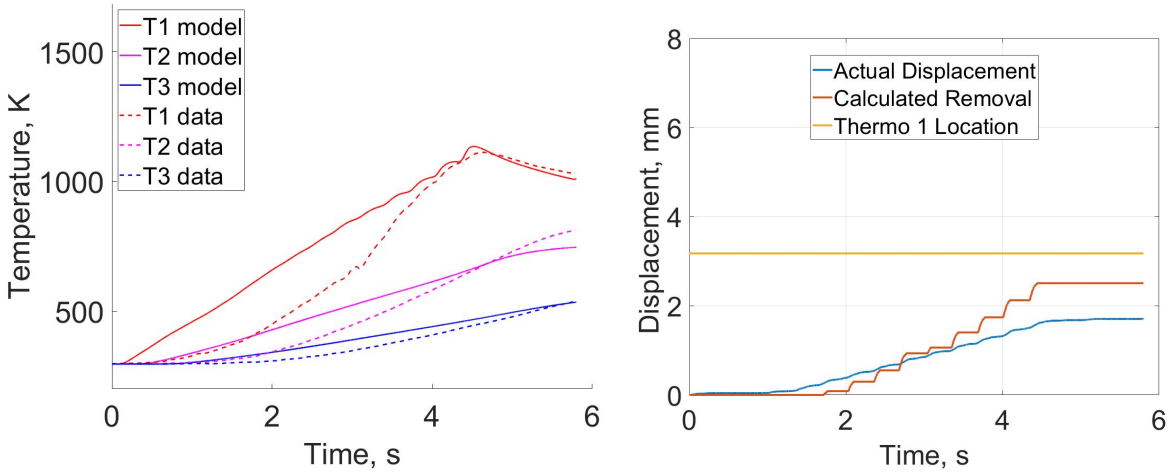

(a) Thermocouple Temperatures (b) Material Removal

Figure 43. Critical Temperature Removal Criteria, 96 m/s

5.3.3 Temperature Dependent versus Constant Material Properties

As illustrated in Figure 26, the constant valued thermal diffusivity used in previous research was generally less than the temperature dependent material property values used in DeLeon's [17] research. Therefore, one would expect the predicted temperature profiles for the constant valued case would fall below those of the temperature dependent case. We see in Figure 44 that this is the case, with dashed lines representing the model thermocouple temperature distributions when applying the temperature dependent material properties, the dotted lines representing the application of constant-valued material properties in the model, with the curves of identical color representing the temperature distributions at the same thermocouple.

Figures 45 and 46 compare the model thermocouple temperature profiles and material removal predictions (according to U_{crit} removal criteria) when using constant material properties to the values of the recorded experimental data. As the resulting temperature profiles fall below those produced when incorporating temperature dependent material properties, less material is predicted to have been removed. In comparison with the model results for incorporating temperature dependent properties, the model thermocouple temperatures for

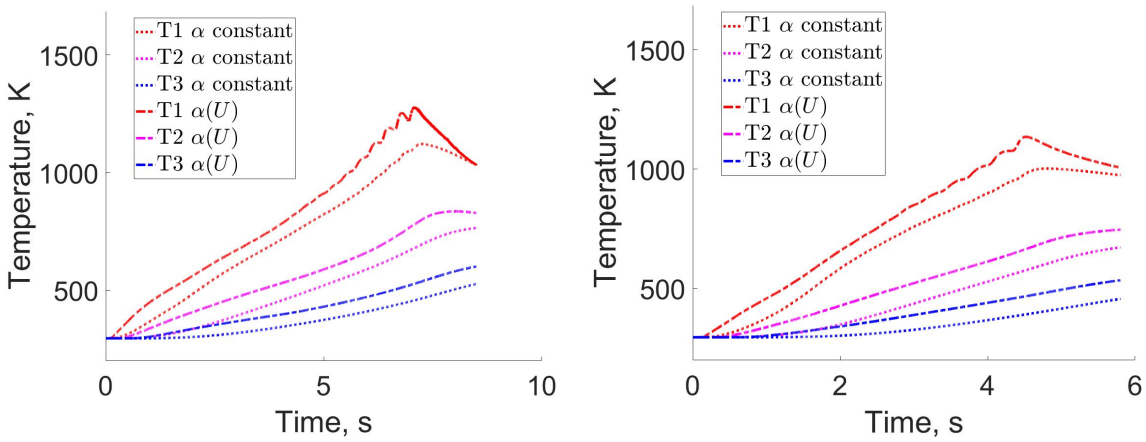

(a) Constant Contact, 48 m/s

(b) Constant Contact, 96 m/s

Figure 44. Model Thermocouple Temperature Profile Comparison, Temperature Dependent vs. Constant Material Properties (αconstant $= 4.4883e-6$ m^2/s)

the case of constant thermal diffusivity are initially a more accurate representation of what was physically observed, as the flow of heat is slower at the onset of contact. However, as time progress ($t \geq 3$ s) and temperatures increase, this lower value of thermal diffusivity imposes a slower diffusion process and the corresponding thermal profiles reflect lower temperature values than those observed both in the experiment and the model produced results under the case of temperature dependent material properties. While the application of constant material properties delays the onset of predicted material removal as surface temperatures are slower to reach U_{crit}, it is a more accurate prediction of overall wear for both test scenarios, as Figures 45b and 46b show only slight over-predictions in the amount of material lost when compared to the actual displacement data.

Due to the influence of thermal diffusivity on the solution, it is clear that not only accounting for temperature dependent material properties, but also ensuring the accuracy of the material parameters, is essential in order to accurately characterize the thermal distribution of the pin.

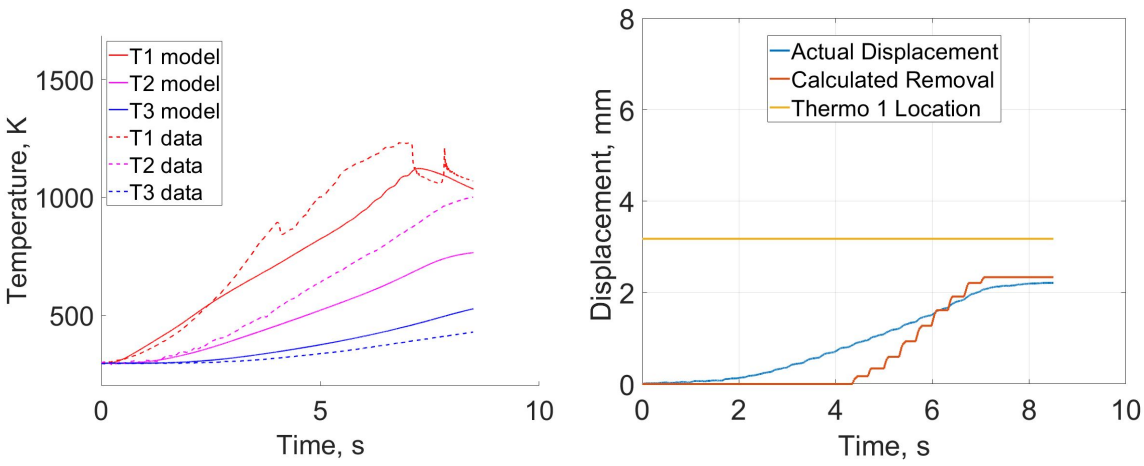

(a) Thermocouple Temperatures (b) Material Removal

Figure 45. Critical Temperature Removal Criteria, 48 m/s, Constant Material Properties

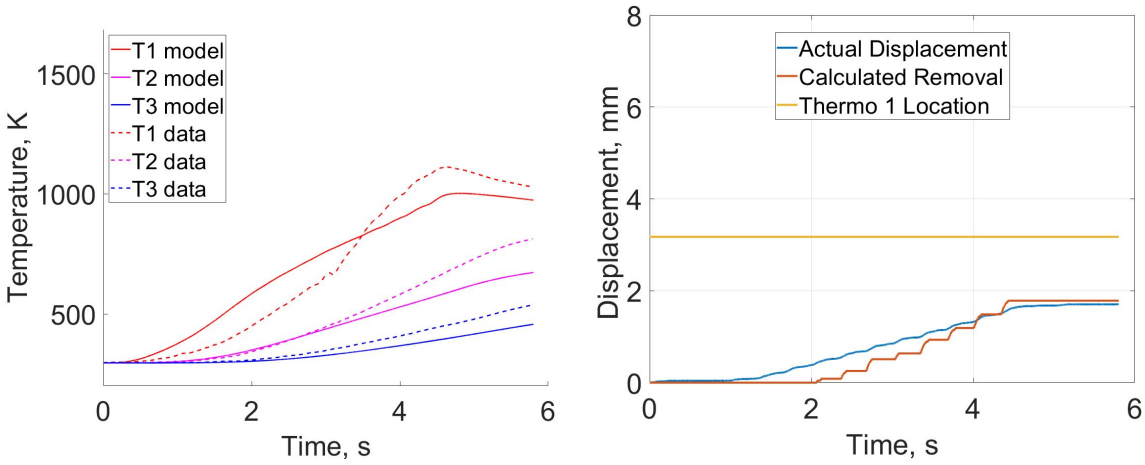

(a) Thermocouple Temperatures (b) Material Removal

Figure 46. Critical Temperature Removal Criteria, 96 m/s, Constant Material Properties

5.3.4 Influence of Heat Partitioning and COF in the Thermal Model

It is important to note the solution's heavy dependence on the chosen values for the heat partitioning coefficient β and the computed values for the coefficient of friction, $\mu(t)$. While a fixed value of β was chosen for the purposes of this model, the heat partitioning factor is more accurately described as a factor dependent on both time and the material properties of the disc and the pin, and is therefore temperature dependent. In the case of the test conducted at 96 m/s, applying $\beta \approx 4\%$ instead of $\beta \approx 3\%$ yields the temperature

profiles and material removal results shown in Figure 47 when using the critical temperature removal criteria (Method 2). We see that the predicted material removal surpasses the location of the first thermocouple, as indicated in Figure 47b where the Calculated Removal curve crosses the Thermocouple 1 Location curve. To reflect this occurrence within the thermal model in Figure 47a, the temperature at the location of Thermocouple 1 is held at U_{crit} for the remainder of the test run. This was not observed in constant contact conditions during experimental testing. Furthermore, the corresponding thermocouple temperature profiles in Figure 47a far exceed the measured values.

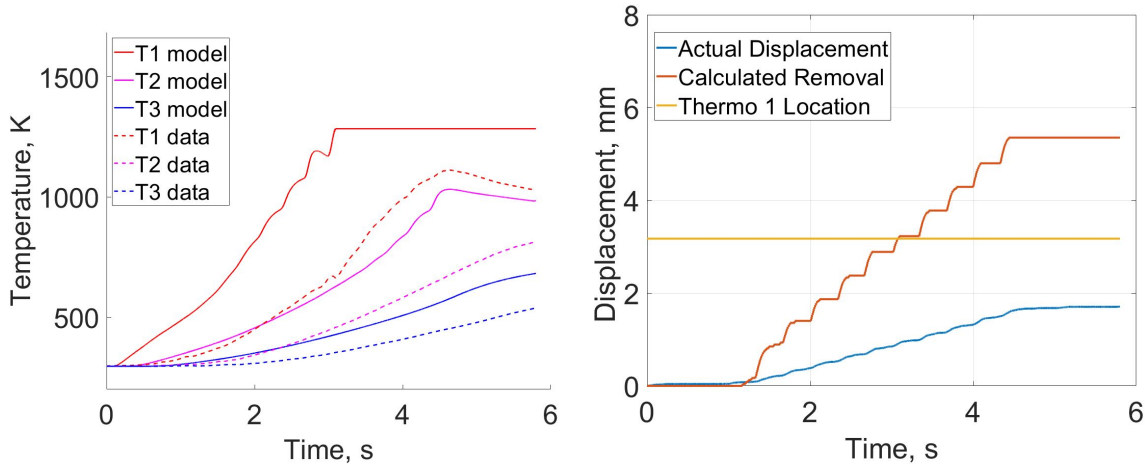

(a) Thermocouple Temperatures (b) Material Removal

Figure 47. $\beta \approx 4\%$, Constant Contact, 96 m/s

Figure 48 considers the opposite extreme, where low values for β are applied to the model and experimental data collected from the test run at 96 m/s. Here, Blok's partition function (Equation 24) is applied to the model according to the respective curve displayed in Figure 32. The low partitioning values for heat flow into the pin yield the model produced temperature profiles in Figure 48a. While the temperature profiles reflect a more accurate representation of the data at the thermocouples for $t \leq 2$ seconds, they begin to deviate well below the recorded data as time progresses due to decreased heat flow into the pin. Therefore, surface temperatures do not reach U_{crit} and zero material is removed within the model, as indicated in Figure 48b.

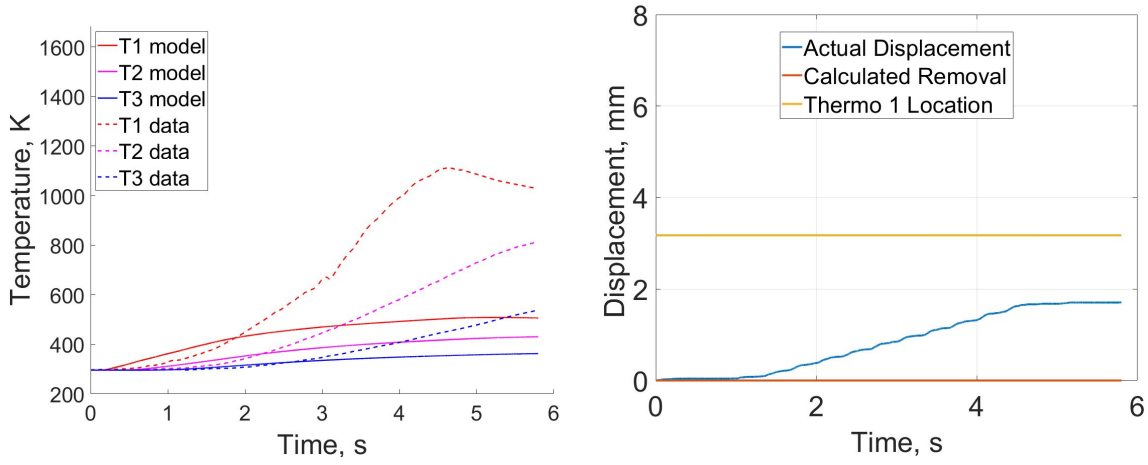

(a) Thermocouple Temperatures (b) Material Removal

Figure 48. Blok's Partition, Constant Contact, 96 m/s

5.3.5 Material Melt Removal

If we instead consider only melt and set $U_{crit} = U_m$, the model calculates zero material removal due to melt (Figure 49b). The thermal results are not drastically effected, however this assumes that the thermocouple locations remain a fixed distance away from the contacting face of the pin, as no material is removed and there is no moving boundary condition. Clearly, this is not the case if implementing the material removal process within the model only when reaching melt temperatures.

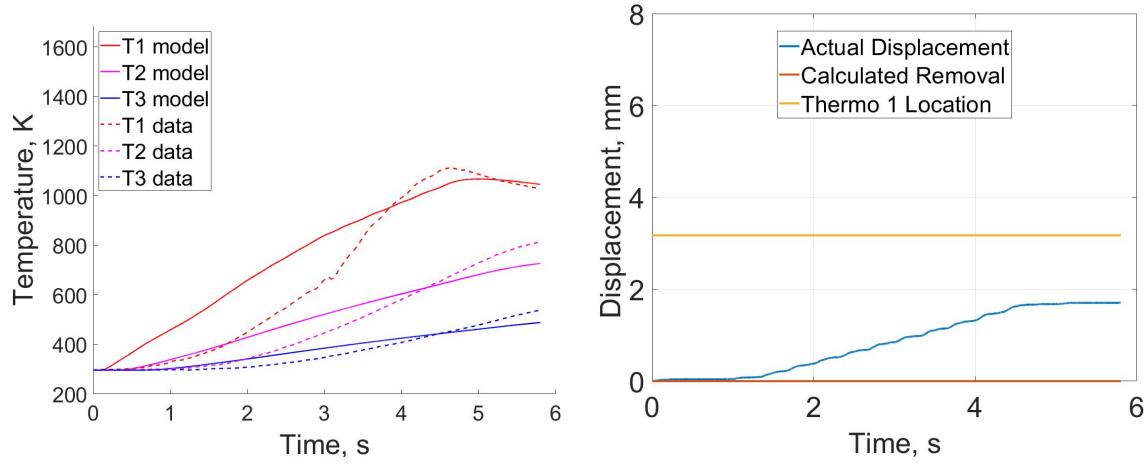

(a) Thermocouple Temperatures (b) Material Removal

Figure 49. Results for $U_{crit} = U_m$, Constant Contact, 96 m/s

5.3.6 Model Accuracy

For both velocities in consideration, the majority of model produced thermal profiles under the assumption of temperature dependent material properties showed initial temperature increases at the thermocouples that were well above observed values. The temperature profiles for the first thermocouple then tend to achieve a similar maximum value (acknowledging that this is above the thermocouple's maximum rated temperature), while model results for the second thermocouple location trend to a value that is lower than recorded values. The temperature profile produced by the model for third thermocouple typically lies above the recorded data for the same location throughout the duration of the test. In comparison with the model results using constant material properties shown in Figures 45 and 46, the use of constant values for thermal conductivity and thermal diffusivity appear to better approximate the thermal behavior at the thermocouples for earlier times, which correspond to lower temperature values.

Direct comparison of the thermal profiles produced by the model based on the two methods of implementation for the moving boundary (shifting the boundary based on recorded displacement data versus removing material at a critical temperature) is shown in Figure 50. The profiles for the second and third thermocouples are virtually identical for each removal method. The temperature models for the first thermocouple only begin to deviate from each other for $t \geq 4$ seconds, as the solution is more heavily influenced by the moving boundary imposed by material removal at U_{crit} since the thermocouple location is closer to the heat source as time progresses. However, the similarity in temperature profiles for the two removal methods gives credence to the use of a critical temperature estimation and subsequent application to predict material removal.

As mentioned in Section 5.2.2, there were two distinctive slopes observed in the recorded displacement data, with the highest rates of movement corresponding to periods of higher force input. When assessing *predicted* material removal in Figure 51, the effect of higher

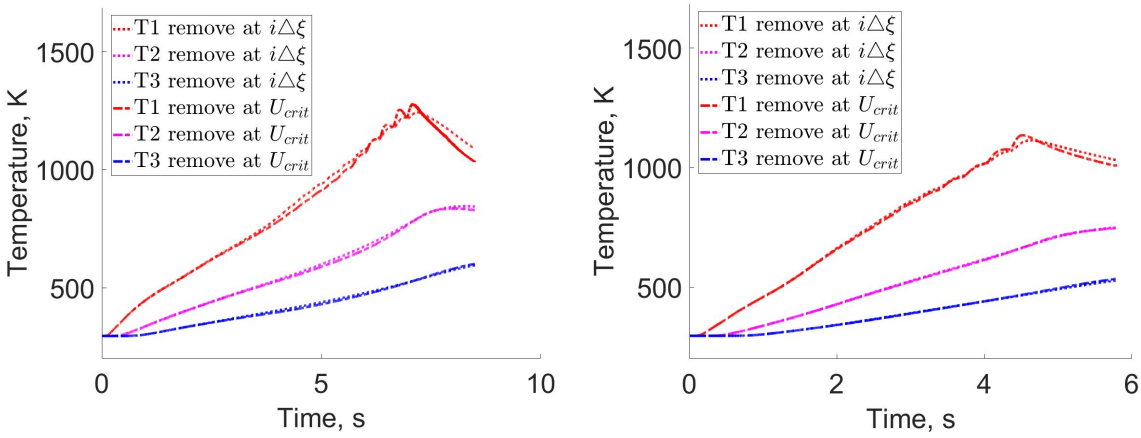

(a) Constant Contact, 48 m/s (b) Constant Contact, 96 m/s

Figure 50. Thermal Profile Comparison, Removal Based on Displacement Data vs. U_{crit} Criteria

force input becomes more distinct and we see that predicted wear coincides with periods of higher force input. In this regard, the model behaves as one would expect and is similar to the recorded displacement data versus force profiles in Figure 29. In Figure 51, the periods of decreasing force, and thus lower heat flux, result in the model reflecting zero material removal at those time steps due to predicted surface temperatures decreasing below U_{crit}.

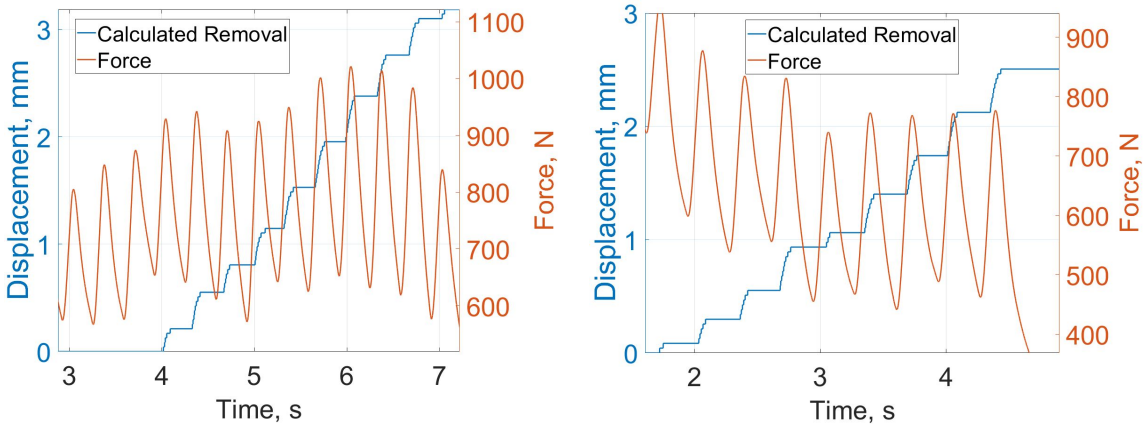

(a) Constant Contact, 48 m/s (b) Constant Contact, 96 m/s

Figure 51. Force vs. Calculated Displacement

Despite the similarity in temperature profiles shown in Figure 50, the recorded displacement data shows material being worn away much earlier in the test runs than the predictive model for material removal (based on the removal criteria of surface temperatures greater

than U_{crit}) indicates. The delay in predicted versus observed material removed indicates that material is physically being removed at lower surface temperatures than the chosen value of U_{crit}. Thus, using a lower value for U_{crit} in the model shifts the time steps of predicted material removal earlier and will more closely resemble the displacement data profiles for earlier times. However, this will cause even more drastic increases in overall removal predictions than the currently chosen value of $U_{crit} = 1276$ K, since the removal process would be implemented at a lower temperature threshold. In contrast, imposing a larger value for U_{crit} will further delay the time of initial material removal but will decrease the total amount of predicted material loss and provide a more accurate approximation of overall wear.

VI. Conclusion

6.1 Conclusions

There are many factors that complicate this seemingly one-dimensional problem. The actual wear of the pin is a function of many variables and adjusting model inputs drastically affects material wear estimations, ranging from predictions of zero material removal to the opposite extreme of causing unrealistic increases in wear calculations. Table 6 is a summary of the input parameters from the two test runs that were studied and includes best estimates for variables that were not quantifiable from data acquisition. Despite the uncertainty of several parameters that influence the numerical model, several conclusions can be made.

Table 6. Experimental Parameters and Variables

Velocity	COF Choice	Average Pressure-Velocity (MPa · mm/s)	β	U_{crit}
48 m/s	Montgomery (Equation 16)	2.42 x 10^5	0.0419	1276 K
96 m/s	Montgomery (Equation 16)	4.21 x 10^5	0.0304	1276 K

6.1.1 Critical Temperature Approach to Material Wear

The use of a single value for U_{crit} to determine material removal criteria may not be valid. It is likely that similar to research conducted by Sundh and Olofsson [50], different wear mechanisms (and corresponding wear rates) can be attributed to different contact temperatures, and there may be multiple values and ranges for U_{crit} that will better characterize material wear for this experiment. While use of the current model captures certain aspects regarding the behavior of the material loss, refinement to incorporate functions of additional parameters may more accurately reflect the removal process as the assumptions of this model do not consider other mechanical and chemical properties that contribute

to wear. The attempt at evaluating energy within the system as solely a function of temperature falls short and indicates that incorporating mechanical energy (work by plastic deformation) should be coupled in the analysis.

6.1.2 Material Properties

The previously approximated temperature dependent properties of specific heat and thermal conductivity may not be as accurate as desired. As thermal diffusivity (as a function of these parameters) greatly influences the behavior of the solution, there were significant deviations in corresponding thermal profiles when considering the results of applying constant versus variable material properties within the model (discussed in Section 5.3.3). For Vascomax® 300, specific heat is the largest contributor to the effect of temperature dependent material properties on the solution. The model's early deviations in temperature profiles from the experimental data, produced when incorporating this non-linear contribution, indicate that the values of specific heat corresponding to lower temperature values may be under-estimated. It is however possible that other factors, one of which was treated as a constant in this research, can account for these early temperature deviations.

6.1.3 Coefficient of Friction Approximation

There were two functions evaluated within the model to define coefficient of friction inputs. It was determined that the regression equation based on Montgomery's research, as a function of pressure-velocity, was a better representation of the physical elements of the interactions between the pin and the disc. This corresponded to higher coefficient of friction values than those produced by Lim and Ashby's equation and subsequently, lower probable values for the heat partitioning coefficient used to distribute heat between the pin and disc.

6.1.4 Heat Partition Coefficient

Imposing a fixed value of the heat partition coefficient β for each test velocity leads to inaccuracies in the solution of the thermal distribution. The influence of β within the model was discussed in Section 5.3.4 and it is clear that it is a major contributor to the transient temperature distribution of the pin. The characteristics of the contact interface between the pin and disc play a role in the division of heat between the surfaces. Therefore, it is likely that the value of β is dependent on both time and material properties, and the inability to account for these factors contributed to discrepancies noted within the thermal profiles and material wear predictions.

6.1.5 Overall Conclusions

While this thermal model provides comparable results under certain assumptions, further testing and analysis are required to validate this approach. The higher velocities create an additional degree of complexity than most pin-on-disc type experiments. Of note, the coefficient of friction and partition function heavily influence the solution as they play a large role in determining the time-dependent heat flux boundary condition. The coefficient of friction is also based on a regression curve fit by compiling wear rate data from variety of experiments and may not be as accurate as desired for this experiment. The values for β were fixed as constants, but are likely dependent on time and material properties. The accuracy of the solution also depends on the respective convection coefficients, determination of which is complex in itself and requires a separate investigation. Similarly, the predictive methods of wear can be improved by analysis of the different wear mechanisms and corresponding temperature ranges that may aid in explaining wear transitions. In general, we see that the behavior of the model agrees with that of the collected data. Further refinement will lead to more accurate predictions of expected temperature distributions and material

loss, and enhance understanding of the factors contributing to heat generation and wear for Vascomax® 300 when subjected to high velocity and high force conditions.

6.2 Contributions to Research Field

The pin-on-disc configuration studied in this work was the first of its kind to impose the high velocity and contact force profiles upon Vascomax® 300 material in a controlled setting. This research improved upon the previous numerical heat transfer model by expanding the thermal profile into two dimensions and implementing a method for material removal in a two-dimensional wear model. This analysis of thermal effects on Vascomax® 300 provides further insight to the thermal behavior of the slipper material with direct application to the HHSTT, and further advances the understanding of temperature effects on wear phenomena. Development of a thermal model in two dimensions and investigating the critical temperature concept for material removal provide a foundation for ongoing research regarding Vascomax® 300 material and pin-on-disc schematics.

6.3 Recommendations

6.3.1 Experimental Considerations

As the force input directly contributes to the heat flux boundary condition, the periodic nature of the current experimental force parameters leads to greater complications when analyzing the effects of other inputs within the model (specifically, the partition coefficient and coefficient of friction). The experiment in question must continue to refine methods for force control in order to remove the corresponding high variations and periodic changes in heat flux at the contact interface. These force oscillations complicate the heat transfer process by creating even more dynamic boundary conditions at the contact interface. It is desired to conduct further testing under more constant loading conditions. The collection

of additional data under more controlled conditions also gives way to statistical analysis of the results and will allow for further conclusions regarding the experimental parameters that prove difficult to otherwise determine.

It is also recommended to consider tests at various force and speed conditions but similar pressure-velocities, in an effort to confirm or disprove the application of the Montgomery data COF regarding this particular pin-on-disc scenario. Given the importance of COF and partition function input to the model and heat transfer process, this would lead to more accurate predictions of these parameters and increase the accuracy of the model.

Finally, in order to verify the accuracy of the thermal data collected by the thermocouples, it is recommended to incorporate analysis of thermal imaging collected from infrared cameras in future experimentation and evaluation. This will also enhance understanding of the convective boundary conditions and their influence on the solution.

6.3.2 Mechanical Contributions

Additional testing would also aid in understanding the role of mechanical effects. The results of this model show that in order to more accurately characterize temperature predictions and material removal approximations, mechanical considerations should be incorporated. To better represent the thermal effects on the wear process of the material under high force and speed conditions, the assumption of heat generation only due to frictional input should be modified to include mechanical inputs of impact at the asperity level. As noted in similar research [54], if plastic deformation is involved in the sliding process, then this plastic dissipation will also influence the temperature increases in the material. This would adjust the differential equation of the form

$$\rho_s \hat{c}_p(U)\frac{\partial U}{\partial t} = \nabla \cdot (\hat{k}\nabla U) + \tau\dot{\gamma} \tag{92}$$

to now include the plastic deformation work that is converted into heating, where τ is the

shear stress and $\dot{\gamma}$ is the shear strain rate. Wei [54] also noted that as time progresses, the influence of the heat generation due to plastic dissipation becomes more dominant than the heat generated at the interface due to friction.

6.3.3 Heat Partitioning

Accounting for mechanical inputs will also affect the prescribed heat partition fraction due to frictional heating, since the addition of work by plastic deformation to the system of equations will decrease the amount of frictional heating required to generate the same thermal profile. This may account for the difference between the higher partitioning values currently used, and the lower theoretical and experimental values outlined in Section 2.8. Other contributions to the higher partition values used in the current model include further consideration of the material characteristics as the temperature increases. Barber [6] observed that at the asperity contact level, most of the deformation will take place in the softer solid, which increases the flow of heat generated by friction into the softer solid. Additionally, although efforts are taken to ensure the disc surface remains as close to ambient temperature as possible, it is likely that the disc surface temperature will increase as the contact time progresses. This is especially likely at higher velocities, as the time between contacts for a given section of the disc will decrease. An increase in disc's surface temperature will affect the heat partitioning due to the reduction in the disc's capacity to dissipate heat, which has been substantiated in other research [20]. The interactions along the surfaces of actual contact between the solids is sensitive to the system inputs, and heat will have a greater propensity to flow into softer solids at higher speeds.

6.3.4 Model Development and Other Assumptions

An argument can be made for the implementation of a model that also considers the temperature distribution of the spinning disc. As discussed, this will more effectively model

the system in its entirety and will lead to increased understanding of the division of heat between the contacting surfaces.

Due to several unknown parameters within the system, it is unclear how the implementation of a three-dimensional model will refine results. Analysis of recovered specimens following testing reveals that the assumption of axisymmetry about the centerline $\rho = 0$ may be an oversimplification of the problem. Additionally, not all material that is displaced is removed, as the mushrooming of the samples indicates. This additional surface area and material mass will affect the heat transfer process in ways that are at this time, undetermined.

6.3.5 Overall

This research provided a preliminary investigation regarding temperature and wear in pin-on-disc configurations, specific to Vascomax® 300 material. Future research must improve upon several experimental parameters to increase understanding of the system as a whole. It is clear that the physics involved in sliding contacts are more complicated than a simple interfacial friction model. Unfortunately, "the relative importance of the plastic working and the interface heating in a coupled thermo-mechanical system is unknown" [54], and further study is required specific to this scenario to account for factors that cannot be simplified or determined under the assumptions in this work.

Bibliography

1. "18 per cent nickel maraging steels: Engineering properties," Publication No. 4419, Nickel Development Institute, 1976.

2. "Material thermal properties database," https://thermtest.com/materials-database# 4340, 2019.

3. C. Alban, "Thermal and melt wear characterization of materials in sliding contact at high speed," Master's thesis, Air Force Institute of Technology, Wright Patterson AFB, OH, 2014.

4. C. Alban, A. Palazotto, and J. Rutledge, "Thermal considerations with respect to sliding contact at high speed," *Journal of Thermophysics and Heat Transfer*, vol. 30, no. 1, pp. 54–61, 2016.

5. S. aus der Wiesche, "Heat transfer from a rotating disk in a parallel air crossflow," *International Journal of Thermal Sciences*, vol. 46, no. 8, pp. 745–754, 2007.

6. J. Barber, "The conduction of heat from sliding solids," *International Journal of Heat and Mass Transfer*, vol. 13, no. 5, pp. 857–869, 1970.

7. T. Bergman, A. Lavine, F. Incropera, and D. DeWitt, *Fundamentals of Heat and Mass Transfer*. John Wiley and Sons, Inc, 2011.

8. G. Berry and J. Barber, "Division of frictional heat - a guide to the nature of sliding contact," *Journal of Tribology*, vol. 106, no. 3, pp. 405–415, 1984.

9. B. Bhushan, *Introduction to Tribology*. John Wiley and Sons, Inc, 2002.

10. H. Blok, "Theoretical study of temperature rise at surfaces of actual contact under oiliness conditions," *Proceedings of the General Discussion on Lubrication and Lubricants*, vol. 1-2, pp. 222–235, 1937.

11. R. Burden and J. Faires, *Numerical Analysis*. Thomson Brooks/Cole, 2005.

12. G. Cameron and A. Palazotto, "An evaluation of high velocity wear," *Wear*, vol. 265, no. 7, pp. 1066–1075, September 2008.

13. F. Carignan and E. Rabinowicz, "Friction and wear at high sliding speeds," *ASLE Transactions*, vol. 23, no. 4, pp. 451–459, 1980.

14. H. Carslaw and J. Jaeger, *Conduction of Heat in Solids*. Oxford University Press, 1959.

15. J. Cinnamon, A. Palazotto, and Z. Kennan, "Material characterization and development of a constitutive relationship for hypervelocity impact of 1080 steel and Vascomax 300," *Impact Engineering*, vol. 33, pp. 180–189, September 2006.

16. R. Dante, *Handbook of Friction Materials and Their Applications*. Woodhead Publishing, 2016.

17. A. DeLeon, W. P. Baker, and A. N. Palazotto, "Modeling a nonlinear melt region as a result of high-speed sliding," *Journal of Thermophysics and Heat Transfer*, vol. 33, no. 3, pp. 808–816, 2019.

18. J. Dormand and P. Prince, "A family of embedded runge-kutta formulae," *Journal of Computational and Applied Mathematics*, vol. 6, no. 1, pp. 19–26, 1980.

19. M. Federici, C. Menapace, A. Moscatelli, G. Straffelini, and S. Gialanella, "Pin-on-disc study of a friction material dry sliding against HVOF coated discs at room temperature and 300° C," *Tribology International*, vol. 115, pp. 89–99, 2017.

20. M. Federici, G. Straffelini, and S. Gialanella, "Pin-on-disc testing of low-metallic friction material sliding against HVOF coated cast iron: Modelling of the contact temperature evolution," *Tribology Letters*, vol. 65, no. 4, pp. 1–12, 2017.

21. C. Gerald and P. Wheatley, *Applied Numerical Analysis*. Pearson Education, Inc, 2004.

22. K. Graff and B. Dettloff, "The gouging phenomenon between metal surfaces at very high sliding speeds," *Wear*, vol. 14, no. 2, pp. 287–97, 1969.

23. P. Grosberg and J. Molgaard, "Aspects of the wear of spinning travelers: the division of heat at rubbing surfaces," *Proceedings of the Institution of Mechanical Engineers, Conference Proceedings*, vol. 181, pp. 16–23, 1966.

24. C. Guo and S. Malkin, "Heat transfer in grinding," *Journal of Materials Processing and Manufacturing Science*, vol. 1, pp. 16–27, 1992.

25. C. Hale, A. Palazotto, and W. Baker, "Engineering approach for the evaluation of mechanical wear considering the experimental Holloman high-speed test track," *Journal of Engineering Mechanics*, vol. 138, no. 9, pp. 1127–1140, September 2012.

26. A. Hall and C. Slunder, "The metallurgy, behavior, and application of the 18-percent nickel maraging steels," NASA SP-5051, Washington D.C., Tech. Rep., 1968.

27. F. Hildebrand, *Finite Difference Equations and Simulations*. Prentice-Hall, Inc, 1968.

28. I. Hutchings and P. Shipway, *Tribology*. Elsevier Ltd, 2017.

29. J. Jaeger, "Moving sources of heat and the temperature at sliding contacts," *Proceedings of the Royal Society of New South Wales*, vol. 76, pp. 203–224, 1942.

30. T. Kagnaya, C. Boher, L. Lambert, M. Lazard, and T. Cutard, "Friction at high sliding speed of WC-6Co pin versus steel disc AISI 1045: Estimation of the contact temperature," *International Journal of Multiphysics*, vol. 3, no. 2, pp. 141–154, 2009.

31. M. Kar and S. Bahadur, "Heat transfer analysis for a pin-and-disc sliding system," *Wear*, vol. 67, pp. 71–84, 1981.

32. F. Kennedy, Y. Lu, and I. Baker, "Contact temperatures and their influence on wear during pin-on-disc tribotesting," *Tribology International*, vol. 82, pp. 534–542, 2015.

33. F. Kennedy and X. Tian, "Modeling sliding contact temperatures, including effects of surface roughness and convection," *ASME Journal of Tribology*, vol. 138, no. 4, pp. 042 101,1–9, 2016.

34. R. Komanduri and Z. Hou, "Analysis of heat partition and temperature distribution in sliding systems," *Wear*, vol. 251, pp. 925–938, 2001.

35. D. Krupovage and H. Rassmussen, "Hypersonic rocket sled development," Technical Report AD-TR-82-41, Test Track Division, 6585 Test Group, Holloman Air Force Base, New Mexico, Tech. Rep., 1982.

36. D. Laird, "The investigation of hypervelocity gouging," Ph.D. dissertation, Air Force Institute of Technology, Wright Patterson AFB, OH, 2002.

37. N. Laraqi, N. Alilat, J. Garcia de Maria, and A. Bairi, "Temperature and division of heat in a pin-on-disc frictional device-exact analytical solution," *Wear*, vol. 266, pp. 765–770, 2009.

38. K. Le, "Study of the thermal environment developed by a traveling slipper at high velocity," Master's thesis, Air Force Institute of Technology, Wright Patterson AFB, OH, 2013.

39. S. Lim and M. Ashby, "Wear-mechanism maps," *Acta Metallurgica*, vol. 35, pp. 1–24, 1987.

40. A. J. Lofthouse, "Computational aerodynamic analysis of the flow field about a hypervelocity sled," Master's thesis, Air Force Institute of Technology, Wright Patterson AFB, OH, 2002.

41. R. Montgomery, “Friction and wear at high sliding speeds,” *Wear*, vol. 36, pp. 276–298, 1976.

42. R. Montgomery, “Projectile lubrication by melting rotating bands,” *Wear*, vol. 39, pp. 181–183, 1976.

43. R. Montgomery, “Surface melting of rotating bands,” *Wear*, vol. 38, pp. 235–243, 1976.

44. O. Nosko, “Partition of friction heat between sliding semispaces due to adhesion-deformation heat generation,” *International Journal of Heat and Mass Transfer*, vol. 64, pp. 1189–1195, 2013.

45. G. Paek-Spidell, “Analysis of heat partitioning during sliding contact at high speed and pressure,” Ph.D. dissertation, Air Force Institute of Technology, Wright Patterson AFB, OH, 2013.

46. A. Ralston and P. Rabinowitz, *A First Course in Numerical Analysis*. McGraw-Hill, Inc, 1978.

47. G. Sewell, *The Numerical Solution of Ordinary and Partial Differential Equations*. John Wiley and Sons, Inc, 2005.

48. F. Stott, “The role of oxidation in the wear of alloys,” *Tribology International*, vol. 31, no. 1-3, pp. 61–71, 1998.

49. N. Suh, “An overview of the delamination theory of wear,” *Wear*, vol. 44, pp. 1–16, 1977.

50. J. Sundh and U. Olofsson, “Relating contact temperature and wear transitions in a wheel-rail contact,” *Wear*, vol. 271, no. 1-2, pp. 78–85, 2011.

51. A. Szmerekovsky, "The physical understanding of the use of coatings to mitigate hypervelocity gouging considering real test sled dimensions," Ph.D. dissertation, Air Force Institute of Technology, Wright Patterson AFB, OH, 2004.

52. H. Uetz and K. Sommer, "Investigations of the effect of surface temperatures in sliding contact," *Wear*, vol. 43, no. 3, pp. 375–388, 1977.

53. Y. Waddad, V. Magnier, P. Dufrénoy, and G. De Saxcé, "Heat partition and surface temperature in sliding contact systems of rough surfaces," *International Journal of Heat and Mass Transfer*, vol. 137, pp. 1167–1182, 2019.

54. Z. Wei and R. Batra, "Modeling and simulation of high speed sliding," *International Journal of Impact Engineering*, vol. 37, no. 12, pp. 1197–1206, 2010.

55. M. Wolfson, "Wear, solid lubrication, and bearing material investigation for high-speed track applications," Technical Report AFMDC-TR-60-7, Test Track Division, 6585 Test Group, Holloman Air Force Base, New Mexico, Tech. Rep., 1960.

56. A. Yevtushenko, O. Ukhanska, and R. Chapovska, "Friction heat distribution between a stationary pin and a rotating ring," *Wear*, vol. 196, pp. 219–225, 1996.

57. S. Ying and Y. Yupeng, "Temperature field analysis of pin-on-disk sliding friction test," *International Journal of Heat and Mass Transfer*, vol. 107, pp. 339–346, 2017.

58. W. Yuen, "The thermal boundary layer in a rotating cylinder subject to prescribed surface heat fluxes," *International Journal of Heat and Mass Transfer*, vol. 37, no. 4, pp. 605–618, 1994.

REPORT DOCUMENTATION PAGE

Form Approved
OMB No. 0704–0188

1. REPORT DATE *(DD–MM–YYYY)*	2. REPORT TYPE	3. DATES COVERED *(From — To)*
26–03–2020	Master's Thesis	August 2018 — March 2020

4. TITLE AND SUBTITLE

Modeling Nonlinear Heat Transfer for a Pin-on-Disc Sliding System

5a. CONTRACT NUMBER

5b. GRANT NUMBER

5c. PROGRAM ELEMENT NUMBER

6. AUTHOR(S)

Boardman, Brian A., Major, USAF

5d. PROJECT NUMBER

5e. TASK NUMBER

5f. WORK UNIT NUMBER

7. PERFORMING ORGANIZATION NAME(S) AND ADDRESS(ES)

Air Force Institute of Technology
Graduate School of Engineering and Management (AFIT/EN)
2950 Hobson Way
Wright-Patterson AFB OH 45433-7765

8. PERFORMING ORGANIZATION REPORT NUMBER

AFIT-ENC-MS-20-M-001

9. SPONSORING / MONITORING AGENCY NAME(S) AND ADDRESS(ES)

Air Force Research Laboratory, Aerospace Systems Directorate
1950 Fifth St., Bldg 18B Rm 15
WPAFB, OH 45433

10. SPONSOR/MONITOR'S ACRONYM(S)

AFRL/RQQ

11. SPONSOR/MONITOR'S REPORT NUMBER(S)

12. DISTRIBUTION / AVAILABILITY STATEMENT

DISTRIBUTION STATEMENT A:
APPROVED FOR PUBLIC RELEASE; DISTRIBUTION UNLIMITED.

13. SUPPLEMENTARY NOTES

14. ABSTRACT

The objective of this research is to develop a numerical method to characterize heat transfer and wear rates for samples of Vascomax® 300, or Maraging 300, steel. A pin-on-disc experiment was conducted in which samples were exposed to a high-pressure, high-speed, sliding contact environment. This sliding contact generates frictional heating that influences the temperature distribution and wear characteristics of the test samples. A two-dimensional nonlinear heat transfer equation is discretized and solved via a second-order implicit finite difference scheme to predict the transient temperature distribution of the pin. This schematic is used to predict the removal of material from the specimens over time based off the temperature profile of the pin. The solutions presented also consider the experimental data and are used to determine characteristics of the contact interface and pin surface associated with the material removal process.

15. SUBJECT TERMS

Heat Transfer, Finite Difference, Pin-on-Disc, Holloman High Speed Test Track, Vascomax® 300

16. SECURITY CLASSIFICATION OF:			17. LIMITATION OF ABSTRACT	18. NUMBER OF PAGES	19a. NAME OF RESPONSIBLE PERSON
a. REPORT	b. ABSTRACT	c. THIS PAGE			Dr. William Baker, AFIT/ENC
U	U	U	UU	125	19b. TELEPHONE NUMBER *(include area code)* (937) 257-3636 x4517; william.baker@afit.edu